UNIVERSITY OF CALIFORNIA
RIVERSIDE

Surface Treatment Methods Using Porous Materials for Thermal and Hydraulic Enhancement in Microchannel Heat Sinks and Energy Storage Units

A Dissertation submitted in partial satisfaction
of the requirements for the degree of

Doctor of Philosophy

in

Mechanical Engineering

by

Ali Ghahremannezhad

December 2019

Dissertation Committee:
Dr. Kambiz Vafai, Chairperson
Dr. Cengiz Ozkan
Dr. Reza Abbaschian

The Dissertation of Ali Ghahremannezhad is approved:

_____

_____

_____

Committee Chairperson

University of California, Riverside

ABSTRACT OF THE DISSERTATION

Surface Treatment Methods Using Porous Materials for Thermal and Hydraulic Enhancement in Microchannel Heat Sinks and Energy Storage Units

by

Ali Ghahremannezhad

Doctor of Philosophy, Graduate Program in Mechanical Engineering
University of California, Riverside, December 2019
Dr. Kambiz Vafai, Chairperson

Due to their unique and interesting properties, porous structures have recently gained increasing attention and are widely utilized in many applications. Large surface area to volume ratio and design simplicity and controllability, has made them a suitable candidate for effective thermal enhancement. In this thesis, capability of porous structures as a novel surface treatment method for thermal and hydraulic enhancement in microchannel heat sinks and energy storage units are studied. First, in chapter 1, we perform a comprehensive investigation on utilizing porous substrates on vertical and horizontal solid fins in a microchannel heat sink (MCHS). Three dimensional models of MCHSs with different solid and porous fin thicknesses are constructed and numerically analyzed. Various thermal and hydraulic performance parameters are evaluated and compared for a parametric optimization on the thickness of the solid/porous fins. The results show that given a set of parameters for a conventional MCHS, an optimized porous design can be found that can improve the thermal capacity at the same or even lower level of pumping power. This type

of improvement is tested and observed for different Reynolds numbers, heat sink materials, and porosities.

In chapter 2, we evaluate the improved porous setup for double-layered MCHSs and effect of utilizing porous substrates on their thermal and hydraulic performance is analyzed. Similar to the single-layered MCHSs, thermal and pumping power of the new porous double-layered MCHSs are evaluated to retrieve the optimized design. Three dimensional geometries are constructed and conjugate heat transfer between the coolant and the MCHS is numerically simulated. A parametric study is presented on the porous and solid fin thicknesses considering two scenarios where the top and bottom microchannels can be similar or having different porous and solid fin thicknesses. Performance parameters including heat transfer effectiveness and pumping power effectiveness are defined and studied for the proposed double-layered MCHSs along with the Figure of Merit (FOM). The results show enhancement in different Reynolds numbers, heat sink materials, and porosities. Interesting behavior is sound for double-layered MCHSs where the top channel has a different design from the bottom one.

In the last chapter, chapter 3, thermal enhancement capability of porous metal foams is investigated for energy storage applications heat sinks working with phase change materials (PCMs). Porous foams as thermal conductivity enhancers (TCEs) are placed inside a PCM-based system and role of the foam's pore structure including the pore size and density is comprehensively studied utilizing a new numerical approach. The porous medium with variable properties is modeled using Darcy-Brinkman-Forchheimer equations and the transient phenomenon of PCM's melting inside the foam is simulated. Positive and negative gradient porous morphologies in different directions of the enclosure are considered the thermal response of the energy storage system is determined. It is found that, the new proposed gradient porous TCEs can considerably affect the thermal performance and the detailed results can be exploited to attain the designs with

higher efficiencies. The melting profile and heat transfer rate distribution is studied for various heating configurations at different melting stages. Effect of porosity, pore density, and size of the enclosure on the melting and energy storage rate is discussed in detail.

Table of Contents

List of Tables

List of Figures

Chapter 1: Thermohydraulic Enhancement in Single-Layered MCHSs with Porous Substrates

Nomenclature:

A	Heat sink's bottom surface area (m^2)
C	Forchheimer's constant
c_f	Heat capacity of the coolant (J kg^{-1} K^{-1})
c_s	Heat capacity of the solid (J kg^{-1} K^{-1})
D_h	Hydraulic diameter of the channel (m)
f	Friction factor
FOM	Figure of merit
h_m	Average heat transfer coefficient (W m^{-2} K^{-1})
k_e	Effective thermal conductivity of the porous medium (W m^{-1} K^{-1})
k_f	Thermal conductivity of the coolant (W m^{-1} K^{-1})
k_s	Thermal conductivity of the solid (W m^{-1} K^{-1})
K_p	Permeability of the porous medium (m^2)
l_f	Height of channel at inlet (m)
L_x	Length of the heat sink (m)

L_y	Height of the heat sink (m)
L_z	Width of the heat sink (m)
N	Number of channels
Nu	Nusselt number
P	Pressure (Pa)
P_{out}	Outlet pressure (Pa)
q_w	Heat flux on the base surface of the heat sink (W m^{-2})
$\dot{Q}$	Volume flow rate of the channel (m^3 s^{-1})
Re	Reynolds number
R_T	Thermal resistance (K W^{-1})
T_{in}	Inlet temperature (K)
T_w	Wall temperature at the centerline of the base surface (K)
$\overline{T}_w$	Average temperature along the base surface (K)
$T_{w,max}$	Maximum wall temperature of the heat sink
t_B	Thickness of the solid at bottom part of channel (m)
t_T	Thickness of the solid at top part of channel (m)
t_S	Thickness of the solid fins (m)

t_P	Thickness of the porous treatment (m)
u_{in}	Inlet velocity of the coolant (m s^{-1})
$\vec{V}$	Velocity vector (m s^{-1})
W_O	Total width of a single channel (m)
W_f	Width of the coolant pathway (m)
x	x coordinate
y	y coordinate
z	z coordinate

Greek symbols:

ε	Porosity
ΔP	Pressure drop from the inlet to the outlet (Pa)
μ_f	Dynamic viscosity (kg m^{-1} s^{-1})
ρ_s	solid density (kg m^{-3})
ρ_f	Coolant density (kg m^{-3})

Ω	Pumping power of a channel (W)
ε_h	Average heat transfer coefficient ratio
ε_p	Pumping power effectiveness

Subscripts:

e	Effective property of the porous medium
f	Fluid phase
m	Mean value
p	Porous medium
s	Solid phase

1. Introduction

Performance rate of electronic components and integrated circuits is getting faster every day. These high-speed working systems generate high amount of intense heat which should be removed in order to keep their functionality and avoid irretrievable damages caused by the resulting high temperatures [1–6]. Heat sinks can be used to dissipate the generated heat from the device to the outside. Different types of heat sinks exist depending on the application, size, cost, and required removal rate. Microchannel heat sinks (MCHSs), introduced by Tuckerman and Pease in 1981 [7, 8], is one of the most used heat sinks for electronics cooling applications. A microchannel heat sink used in experiments of Hadad et al. [9] with 135 microchannels in which each microchannel has a width of 0.2 mm and length of 64 mm, is shown in Figure 1-1. These types of heat sinks are simple to manufacture, efficient in heat removal, low-cost, and reliable [4–17]. Since their introduction, many studies have worked on their design to introduce new techniques for their thermal enhancement [18–24].

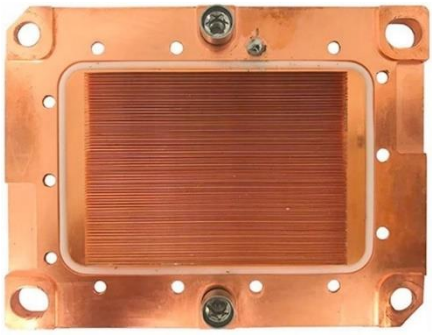

Figure 1-1 A microchannel heat sink with 135 microchannels (width of 0.2 mm and length of 64 mm) [9]. (adapted with copyright permission)

One of the novel techniques to increase the heat transfer capability is using porous metals that increase the surface area between the coolant and the solid [25–28]. Therefore, it has been used in microchannel heat sinks for heat transfer improvement [29–36]. Huang and Vafai [37, 38]

investigated the convective heat transfer for arrays of porous blocks and porous cavity arrangements over an external surface. Ould-Amera [38] placed a porous matrix between the heat generating blocks in a parallel plate channel and found a significant rise in the heat transfer rate. Forced convection in high porosity aluminum metal foams were studied by Calmidi and Mahajan [27] and empirical correlations for Nusselt number in various porous samples were reported. Significant change in the flow patterns and lower friction factor caused by porous baffles in a rectangular channel is reported by Yang and Hwang [40]. Jiang et al. [41] showed enhancement in local heat transfer coefficient when using sintered porous medial in a cooling plate. Fluid flow and forced convection heat transfer in heat sink channels filled by porous media for high-power mini devices has been studied by Haji-Sheikh et al [25], Hetsroni et al. [29], and Hooman [42]. Singh et al. [34] performed series of experiments on a porous heat sink for cooling high-powered microprocessors in server applications and showed higher convective heat transfer and lower thermal resistance accompanied by a significant pressure drop caused by the porous matrix. The porous heat sink that they used for this purpose and magnified sintered porous media are shown in Figure 1-2. Jeng et al. [35] worked on a porous heat sink shown in Figure 1-3 which uses metal foam and an inserted conductive cylinder to increase the average Nusselt number. Porous heat sinks have also been used for thermal management of high-power LEDs by Wan et al. [33]. Hung et al. [32] performed comparative and optimization studies on different porous structures placed inside a microchannel heat sink and identified the candidate structures that can better improve the thermal performance based on a defined performance evaluation parameter. Effect of using gradient porous structures and stacked porous layers inside a channel are studied by Wang et al. [30] and Dathathri and Balaji [43].

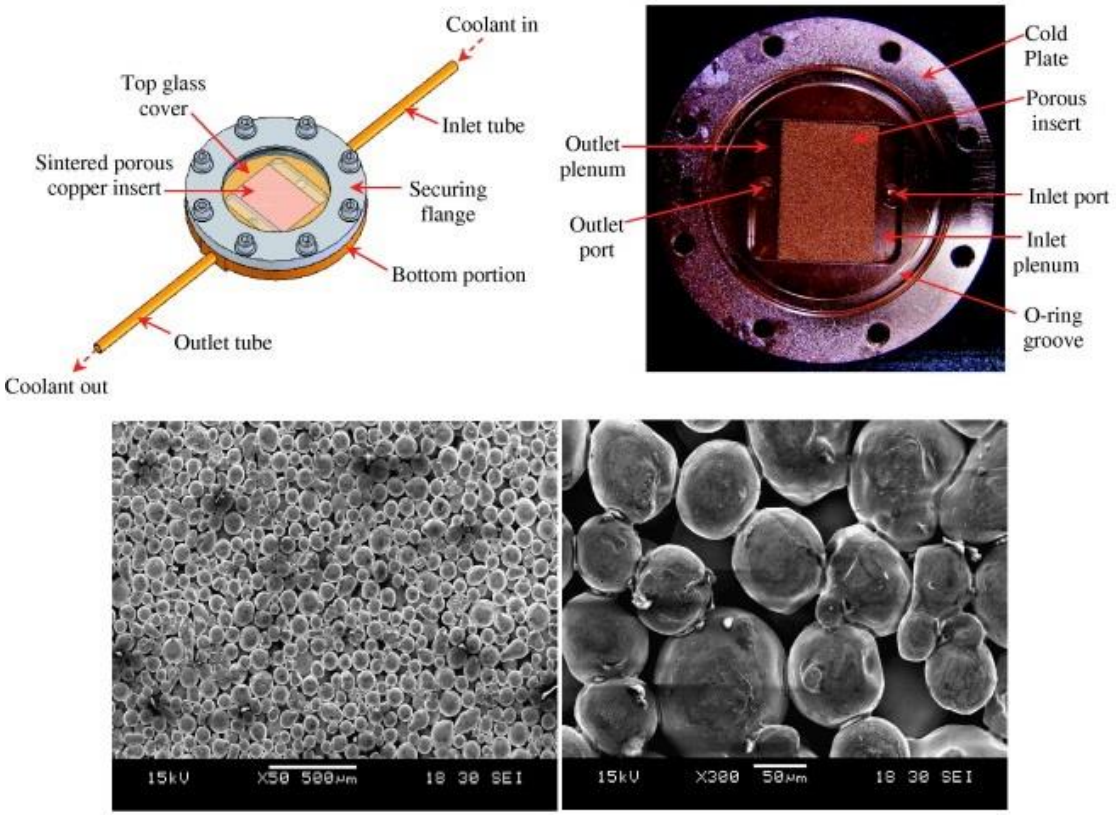

Figure 1-2 Porous heat sink used by Singh et al. [34] for cooling of high-powered microprocessors. The sintered porous media is also shown with two magnifications. (adapted with copyright permission)

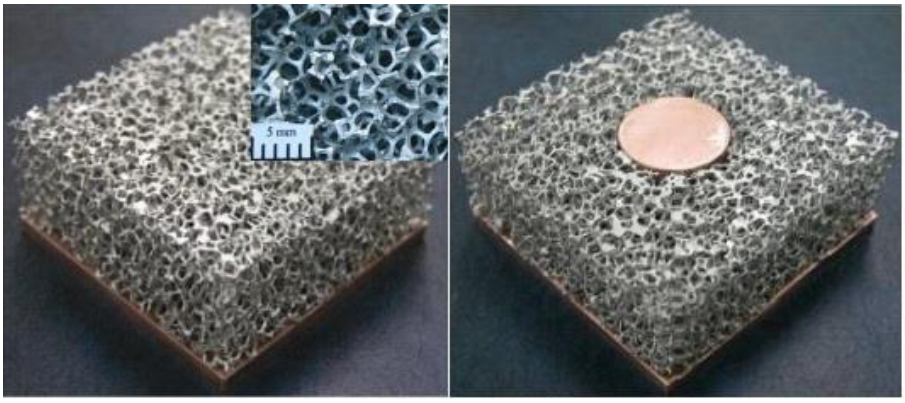

Figure 1-3 A porous heat sink in study of Jeng et al. [35] that uses metal foam (left) and an inserted conductive cylinder inside metal foam (right). (adapted with copyright permission)

Chuan et al. [44] replaced the solid fins of a microchannel heat sink with porous ones and found that porous fins result in a 43% to 47.9% decrease in the pressure drop with only a 5% increase in the thermal resistance. Following this study, Lu et al. [45] numerically studied a wavy microchannel heat sink with porous fins which resulted in a simultaneous reduction in pressure drop and thermal resistance compared to the convectional wavy MCHSs with solid fins.

There are many works that have utilized the benefits of porous media inside a channel for enhancement purposes. Here we have discussed some major studies in this area. However, in most studies, improvement in thermal aspect of the microchannel heat sink is accompanied by unfavorable rise in the pressure drop and vice versa. In this dissertation, our primary objective is to perform an optimization parametric study based on a microchannel heat sink with a compound solid and porous fin design to analyze the scale in which the thermal and hydraulic performances change, and to obtain the designs where both aspects can possibly improve. For this purpose, in chapter one we discuss the proposed porous/solid design for single-layered microchannel heat sinks. Three dimensional models of the MCHSs are created and conjugate heat transfer is studied numerically to obtain the thermohydraulic performance. Afterwards, sensitivity analysis is performed to get a better idea of the performance in specific functional area with respect to the average heat transfer, pumping power, and combined performance evaluation criteria. In chapter two, we apply this idea for double-layered MCHSs and evaluate the thermohydraulic results. The differences between the proposed design for single-layered and double-layered MCHSs are identified. For double-layered MCHSs we categorize different cases in two scenarios. Details are discussed in introduction of chapter 2. In the last chapter, we explore the thermal enhancement ability of the porous media in energy storage systems and indicate the novel surface treatment designs that could also be beneficial in treating the PCM-based energy systems.

2. Problem Description

The three dimensional and front view of the assumed surface treatment utilizing porous substrates for single-layered MCHSs are shown in Figure 1-4. Porous structures are placed on the vertical and horizontal fins.

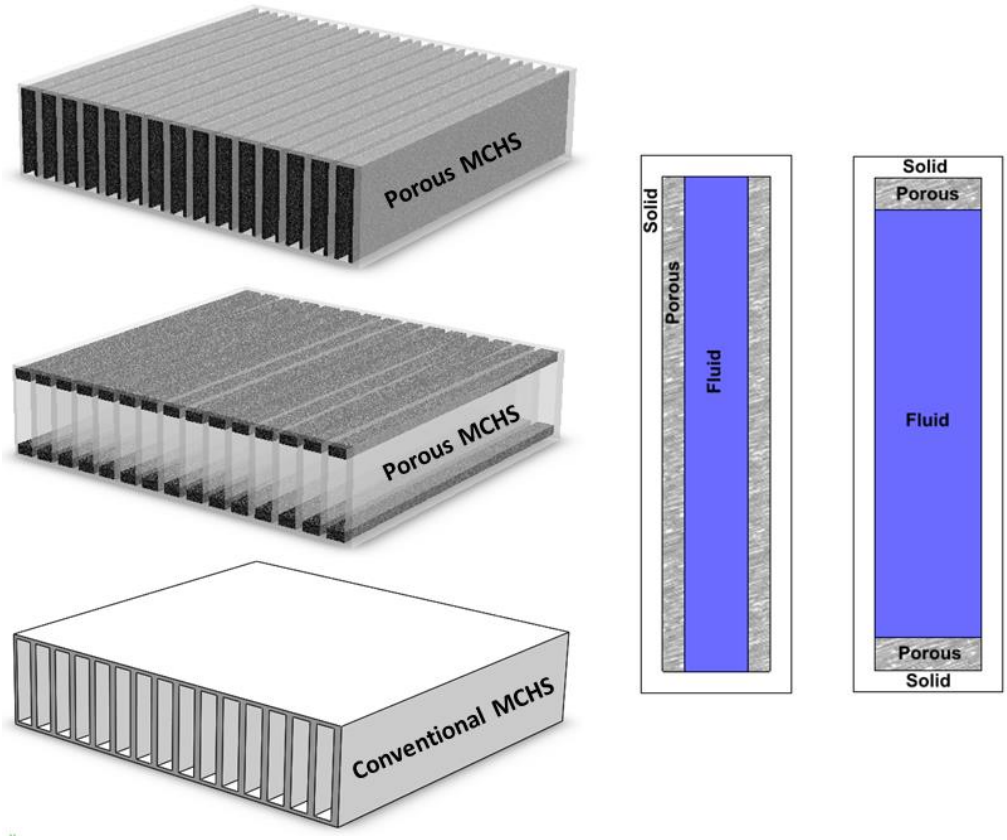

Figure 1-4 Proposed porous structures: conventional and porous MCHS.

Water as the coolant flows inside the microchannels and transfers the heat to the outside environment. The schematic of the porous MCHS and the computational domain are shown in Figure 1-5 (a). Geometric definitions are shown in Figure 1-5 (b). Each microchannel has a total height of L_y and a width of W_O, two half vertical solid fins with thickness of t_S, bottom horizontal

solid fin with thickness of t_B, and top horizontal solid fin with thickness of t_T. Heat enters the domain from the bottom surface and removed by the coolant as shown in Figure 1-5 (c).

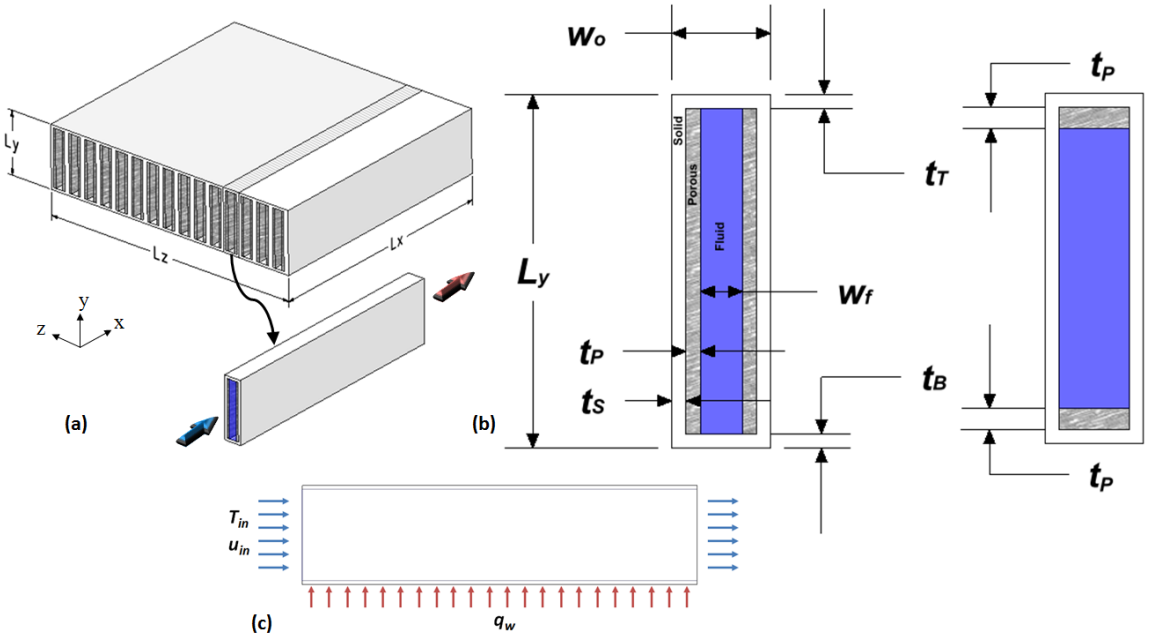

Figure 1-5 (a) Schematic of the porous MCHS and the assumed computational domain; (b) Geometric parameters of the generic porous microchannel; (c) Heat flux is applied at the bottom surface of the channel and removed by the coolant.

3. Numerical Procedure

The sintered porous domains are assumed to be homogeneous, isotropic, and fully saturated with the coolant. Local thermal equilibrium is assumed between the solid and coolant through the porous domains [46–51]. The fluid flow is incompressible, laminar, and steady. Thermo-physical properties are constant in the working temperature ranges and the gravitational and radiation effects are negligible. The heat sink is insulated from the outside environment. To model the fluid flow through the porous domains, Forchheimer-Brinkman-Darcy equations based on a volume-

averaging method are used [50,51]. Based on these assumptions, the governing equations which are continuity, momentum, and energy will be as follows [50]:

$$\nabla.\left(\varepsilon\rho_f\vec{V}\right)=0, \tag{1-1}$$

$$\frac{\rho_f}{\varepsilon^2}\left(\vec{V}.\nabla\right)\vec{V}=\nabla P-\left(\frac{\mu_f}{K_p}+\frac{\rho_f C}{\sqrt{K_p}}\left|\vec{V}\right|\right)\vec{V}+\frac{\mu_f}{\varepsilon}\nabla^2\vec{V} \tag{1-2}$$

$$(\rho c)_e\left(\vec{V}.\nabla T\right)=k_e\nabla^2 T \tag{1-3}$$

where ε is the porosity of the porous domain; ρ_f density of the fluid; $\vec{V}$ velocity vector of the fluid; P pressure; K_p permeability; C the Forchheimer's constant; μ_f viscosity of the fluid; T temperature; k_e effective thermal conductivity and $(\rho c)_e$ is the effective heat capacity of the porous domain. The effective thermal conductivity, k_e is obtained from $k_e=\varepsilon k_f+(1-\varepsilon)k_s$ and $(\rho c)_e$ is $(\rho c)_e=\varepsilon\rho_f c_f+(1-\varepsilon)\rho_s c_s$ in which f and s are indices for fluid and solid respectively [50]. The energy equation for the solid domain is as follows:

$$k_s\nabla^2 T_s=0 \tag{1-4}$$

where k_s is the thermal conductivity of the solid domain.

The boundary conditions are listed as follows:

Inlet

$$u=u_{in},\quad v=0,\quad w=0,\quad T=T_{in}\qquad \text{at } x=0 \tag{1-5}$$

Outlet

$$P=P_{0ut}\qquad \text{at } x=L_x \tag{1-6}$$

Solid-fluid interface

$$\vec{V} = 0, \quad T_f = T_s, \quad -k_f \nabla T_f\big|_n = -k_s \nabla T_s|_n \,, \tag{1-7}$$

where n is the normal unit vector.

Bottom wall

$$q_w = -k_s \nabla T_s|_n \,, \tag{1-8}$$

At symmetric interfaces and insulated walls

$$-k_s \nabla T_s|_n = 0 \tag{1-9}$$

The inlet velocity changes from 0.2 to 2 m/s and a uniform temperature of 300 K is assumed at the inlet of the channels. Constant pressure is assumed at outlet and no slip condition is considered at the solid walls. The top surface is insulated and a heat flux of $q_w = 100$ W/cm^2 is applied at the bottom surface of the MCHSs. The left and right surfaces of the generic microchannel are considered as the periodic boundary conditions.

Other parameters used to evaluate the performance of MCHSs can be described as follows [31,32,44,52,53]:

Reynolds number

$$Re = \frac{\rho_f u_{in} D_h}{\mu_f}, \tag{1-10}$$

Friction factor

$$f = \frac{1}{2} \frac{D_h}{L_x} \frac{\Delta P}{\rho_f u_{in}^2}, \tag{1-11}$$

Pumping power

$$\Omega = \dot{Q}\Delta P = u_{in} l_f w_f \Delta P, \quad (1\text{-}12)$$

Average heat transfer coefficient of the MCHS

$$h_m = \frac{q_w}{(\overline{T}_w - T_{in})}, \quad (1\text{-}13)$$

Nusselt number

$$Nu_m = \frac{h_m D_h}{k_f}, \quad (1\text{-}14)$$

Thermal resistance

$$R_T = \frac{T_{w,max} - T_{in}}{q_w A}, \quad (1\text{-}15)$$

where D_h is the hydraulic diameter of the channel $D_h = 2(l_f w_f)/(l_f + w_f)$; $\dot{Q}$ volume flow rate of the channel; T_{in} inlet temperature; $\overline{T}_w$ average wall temperature along the centerline of the bottom surface; $T_{w,max}$ maximum bottom wall temperature of the MCHS; and A is the surface area of the bottom surface.

To compare the performance of a MCHS with a new design to a basic MCHS, some other comparative parameters are usually used [32]. Average heat transfer effectiveness gives the improvement in the Nusselt number of the new design compared to a basic MCHS.

$$\varepsilon_h = \frac{h_{m,new}}{h_{m,base}}, \quad (1\text{-}16)$$

We also define a "pumping power effectiveness" parameter to be used along with the average heat transfer effectiveness to compare MCHSs [52, 53].

$$\varepsilon_p = \frac{\Omega_{base}}{\Omega_{new}}, \qquad (1\text{-}17)$$

Figure of merit (FOM) is defined to compare two different designs in order to determine the improvement of one design both in terms of heat transfer and pumping power compared to the other. It is described as follows [31,32,44,52,53]:

$$FOM = \frac{(h_{m,new}/h_{m,base})}{(\Omega_{new}/\Omega_{base})^{1/3}}, \qquad (1\text{-}18)$$

To solve the governing equations, the finite volume approach was used adopting a SIMPLE scheme [54]. A grid independency is performed to obtain the appropriate size of the computational cells for the purpose of accuracy and reducing the computational time. The results are summarized in Table 1-1. The grid size of 120 × 80 × 50 is used accordingly. Each equation is solved with a convergence criterion of 10^{-6}. For validation, experimental works of Hetsroni et al. [29] and Jiang et al. [41] on porous samples with porosities of $\varepsilon = 0.402$ and $\varepsilon = 0.444$ are chosen. As shown in Figure 1-6, an excellent agreement between the numerical and experimental results is achieved implying the satisfactory reliability and accuracy of the current numerical procedure.

Table 1-1 Grid independency examination

Grid	Number of nodes	h_m (kW m^{-1} K^{-1})	f
100 × 60 × 40	240000	12.424	0.2177
120 × 80 × 50	480000	12.422	0.2185
140 × 100 × 60	840000	12.422	0.2189

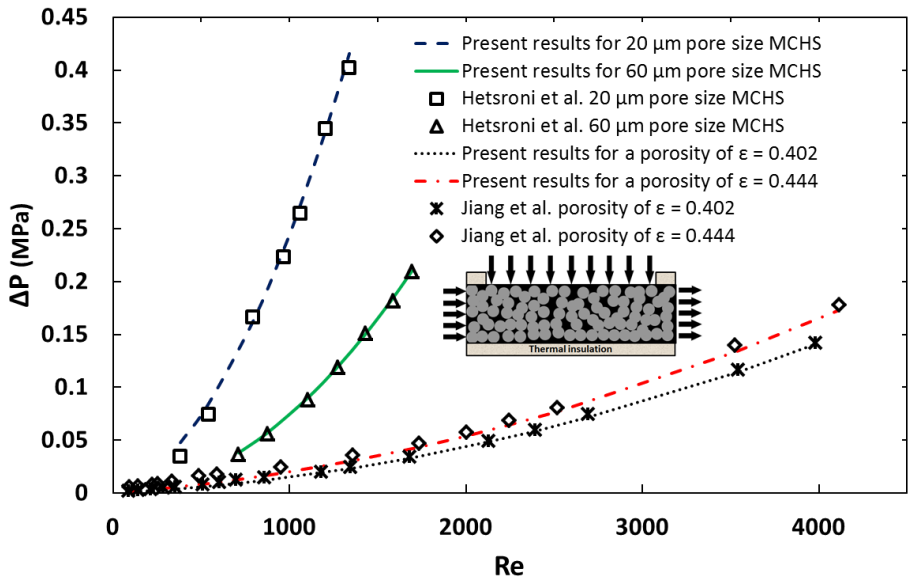

Figure 1-6 Comparison of the present results with the experimental data of Hetsroni et al. [29] and Jiang et al. [41].

4. Results and discussion

Here we present and discuss the results for the porous-treated microchannel heat sinks. For comparison, we consider a conventional microchannel heat sink with vertical solid fin thickness of $t_S = 0.1$ mm, and bottom and top solid thicknesses of $t_B = 0.1$ mm and $t_T = 0.1$ mm without any porous substrate as the basic MCHS. Performance improvement of other MCHSs are evaluated based on the comparison with the assumed basic MCHS. Thermal properties of the coolant, the solid, and the porous domain are listed in Table 1-2. All geometrical parameters for this chapter are listed in Table 1-3. Reynolds number has been changed from 20 to 200.

Table 1-2 Thermal properties of coolant, solid section, and porous structure

Materials	ρ (kg m^{-3})	C_p (J kg^{-1} K^{-1})	k (W m^{-1} K^{-1})	μ (Pa s)
Coolant: Pure water	998.2	4182	0.6	0.000855
Substrate: Steel	8030	8030	16.27	
Porous medium: Steel	8030	8030	16.27	

Table 1-3 Geometrical parameters used for MCHSs.

Parameter	Minimum value	Constant value	Maximum value
L_x (mm)	-	10	-
L_y (mm)	-	2.5	-
L_z (mm)	-	10.6	-
w_o (mm)	-	0.7	-
w_f (mm)	0.05	-	0.6
t_T (mm)	0.04	-	2.3
t_B (mm)	0.04	0.1	2.3
t_P (mm)	0.005	-	0.3
t_S (mm)	0.025	-	0.325

4.1 Heat Transfer and Pumping Power

For parametric optimization, the vertical solid fin thickness, t_S, has been increased from 0.025 to 0.325 mm, while for each solid thickness, the porous thickness, t_P, has been changed from 0.005 to 0.3 mm. The bottom and top solid thicknesses are increased from 0.04 to 2.3 mm. The temperature of the coolant increases from inlet to the exit with its maximum value occurring at the bottom surface. Heat transfer coefficient of the MCHSs with various porous insert thicknesses on the vertical fins is plotted in Figure 1-7. As can be seen, increasing the porous thickness results in increase of the heat transfer coefficient until an optimum point is reached. After that point, adding more porous domain will adversely decrease the heat transfer coefficient. Also, after a specific solid thickness, $t_S = 0.25$ mm, adding any porous substrate to the MCHS will decrease the average heat transfer coefficient. The average heat transfer of the basic conventional MCHS is shown on the figure with a straight solid line for performance evaluation reference. Maximum heat transfer is observed for a MCHS with solid thickness of $t_S = 0.25$ mm and porous thicknesses of $t_P = 0.025$ mm. However, at this solid/porous fin thickness considerable higher pressure drops and pumping

powers are seen as plotted in Figure 1-8. It can also be noticed that no optimum point occurs in the pressure drop curves. The rise in pressure drop for higher solid/porous thicknesses is exponential.

To be able to evaluate both thermal and hydraulic performances simultaneously, Figure of merit (FOM) is compared for the considered MCHSs. In Figure 1-9 FOM of the MCHSs is plotted versus the porous substrate thickness for different vertical solid fin thicknesses. It can be seen that, for all solid thicknesses there is a range of porous substrate thickness that results in a higher FOM than the conventional MCHS shown with the straight line. As t_S increases the maximum FOM occurs at a lower t_P. The highest FOM occurs for a porous MCHS with $t_S = 0.2$ mm and $t_P = 0.025$ mm which has only 9% lower heat transfer coefficient than the one with highest $\bar{h}_m$, but has 59% lower pressure drop. Therefore, FOM can be used as a reliable measure to obtain MCHSs with superior performance considering both heat transfer and pressure drop aspects.

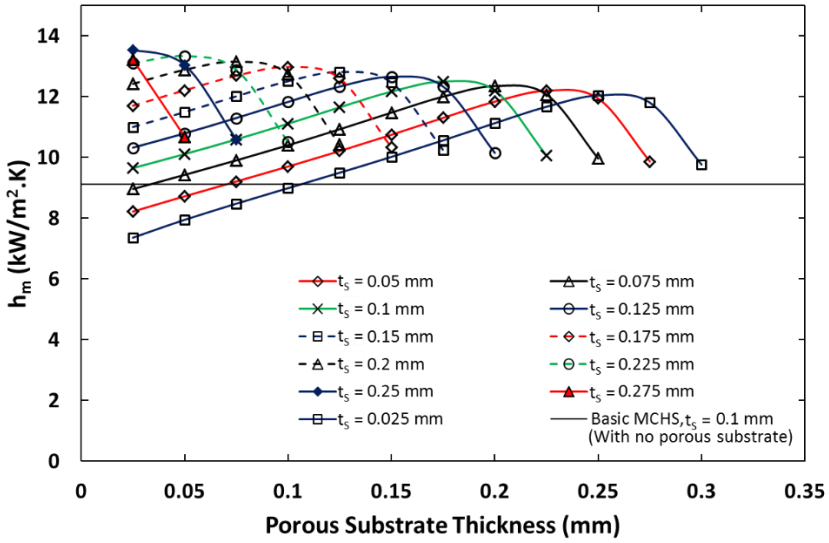

Figure 1-7 Heat transfer coefficient of MCHSs with different vertical solid fin thicknesses and varying porous substrate thicknesses.

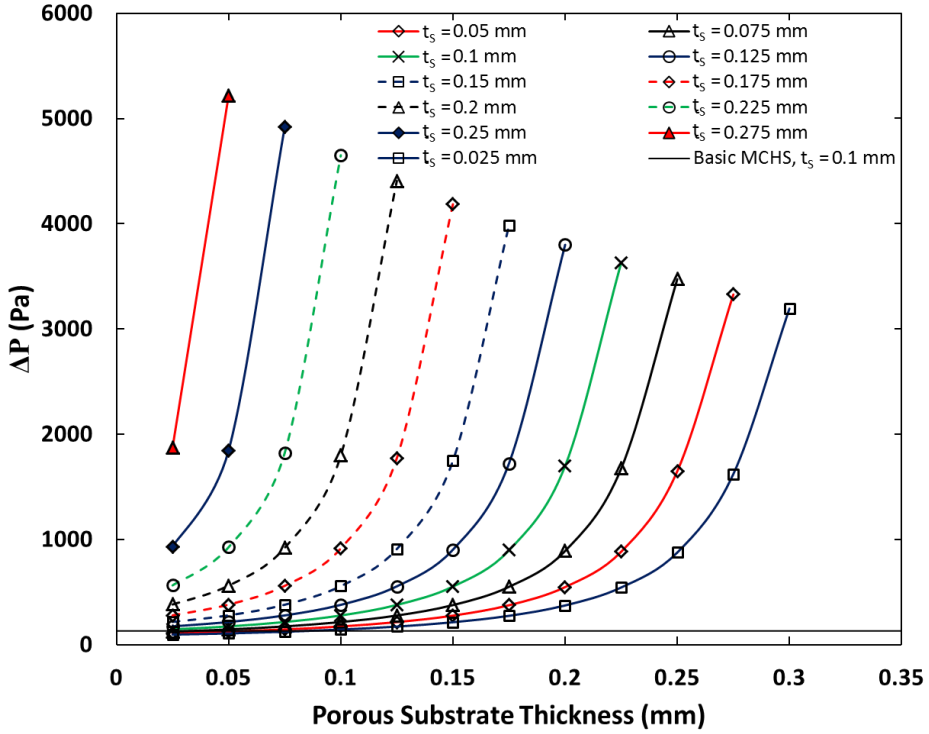

Figure 1-8 Pressure drop of microchannel heat sinks versus the porous substrate thickness for different vertical solid thicknesses.

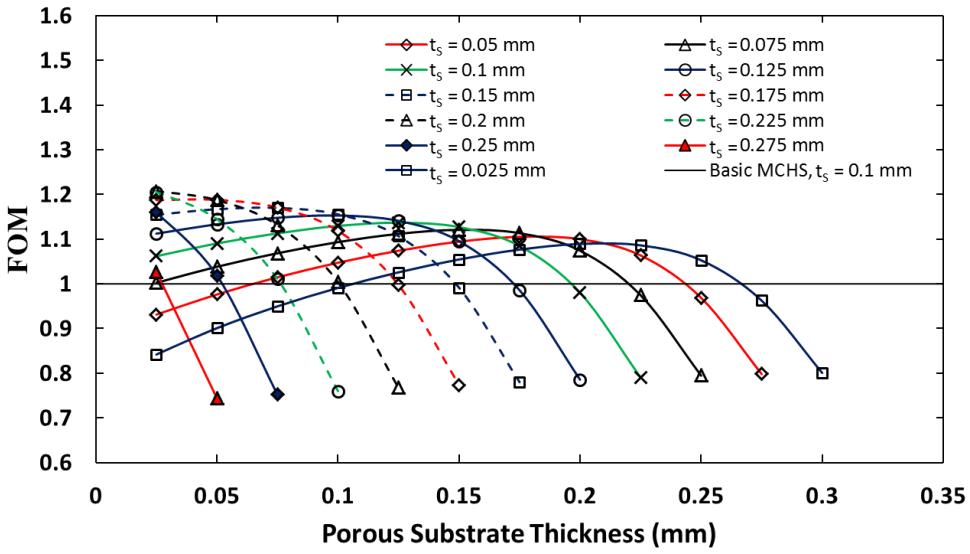

Figure 1-9 FOM of microchannel heat sinks versus the porous substrate thickness for different vertical solid thicknesses.

Porous substrates are also placed on the bottom and top horizontal fins of the microchannel heat sink to see their effect on thermal and hydraulic performances. As can be seen in Figure 1-10, the critical point can also be found for porous substrates thickness on the horizontal fins. The optimal heat transfer point for the bottom fin occurs at lower porous substrate thicknesses while for the top fins it occurs at higher thicknesses. The pressure drop curves for the horizontal fins are shown with dash lines. As the case for the vertical fins, increasing the comping solid/porous thickness increases the pressure drop. Furthermore, bigger solid to porous ration results in a higher pressure drop and consequently pumping power.

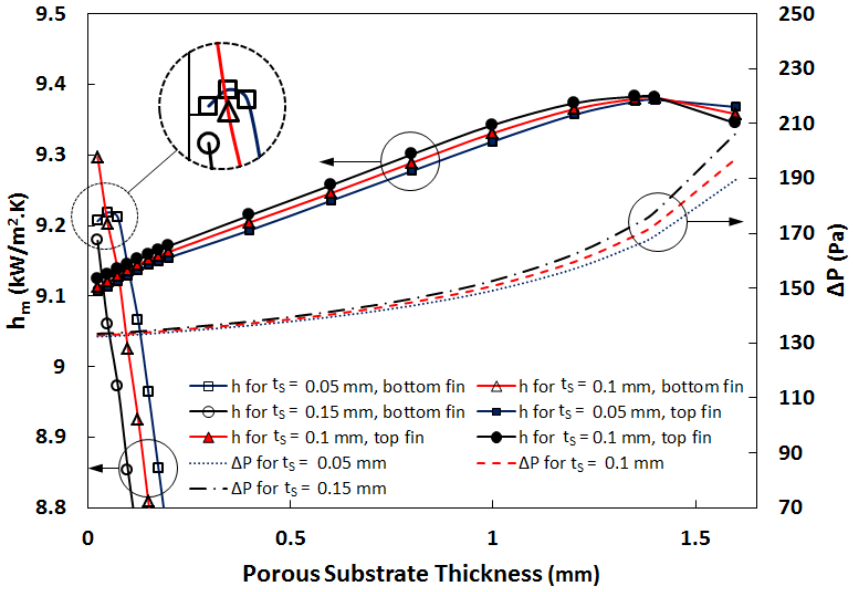

Figure 1-10 Heat transfer coefficient and pressure drop of MCHSs with different horizontal solid fin thicknesses and varying porous substrate thicknesses. (solid lines represent h_m and dash lines represent ΔP).

4.2 Sensitivity Analysis

In this section, we perform a sensitivity analysis for some chosen solid and porous fin thicknesses which we are interested in terms of heat transfer and pumping performance. The analyzed porous MCHSs are compared based on the defined basic conventional MCHS using

evaluation parameters ε_h and ε_P. Porous MCHSs with vertical solid fin thicknesses close to $t_S = 0.1$ mm are shown in Figure 1-11 (a). Compared to the basic MCHS, improvement in the thermal aspect is identified with $R_{T0}/R_T > 1$ and in hydraulic aspect with $\Omega_0/\Omega > 1$. As can be seen, there is a range for the porous substrate thickness for the majority of solid fin thicknesses where both aspects can be improved. This range is shown for each t_S with $t_{P,opt}$ and the regions where ε_h and ε_P are larger than 1 are illustrated by dashed areas. Reducing the solid part of the fin results in a decrease of the effective thermal conductivity but on the other hand reduces the pressure drop. To compensate for the loss in thermal conductivity, more porous substrate can be added when the pressure drop is still lower than the basic MCHS. For porous MCHSs with solid fin thickness close to the basic MCHS, the dashed areas become larger due to higher effective thermal conductivity. The point of intersection between the ε_h and ε_P lines is the point of interest for simultaneous improvement in heat transfer and pumping power.

A similar sensitivity analysis is shown in Figure 1-11 (b) for porous MCHSs with vertical solid thicknesses close to $t_S = 0.225$ mm where the highest FOM was observed. The same trend can also be seen here with pumping power ratio lines (ε_P) getting steeper. For all considered solid thicknesses from $t_S = 0.2$ mm to $t_S = 0.22$ mm, there is a range of porous substrate thicknesses that higher heat transfer coefficient and lower pumping power compared to the conventional MCHS with $t_S = 0.225$ mm are obsereved. The range of t_P where this simultaneous enhancement occurs, is shown in Figure 1-11 (b) as well as the dashed areas in which ε_h and ε_P are both larger than 1.

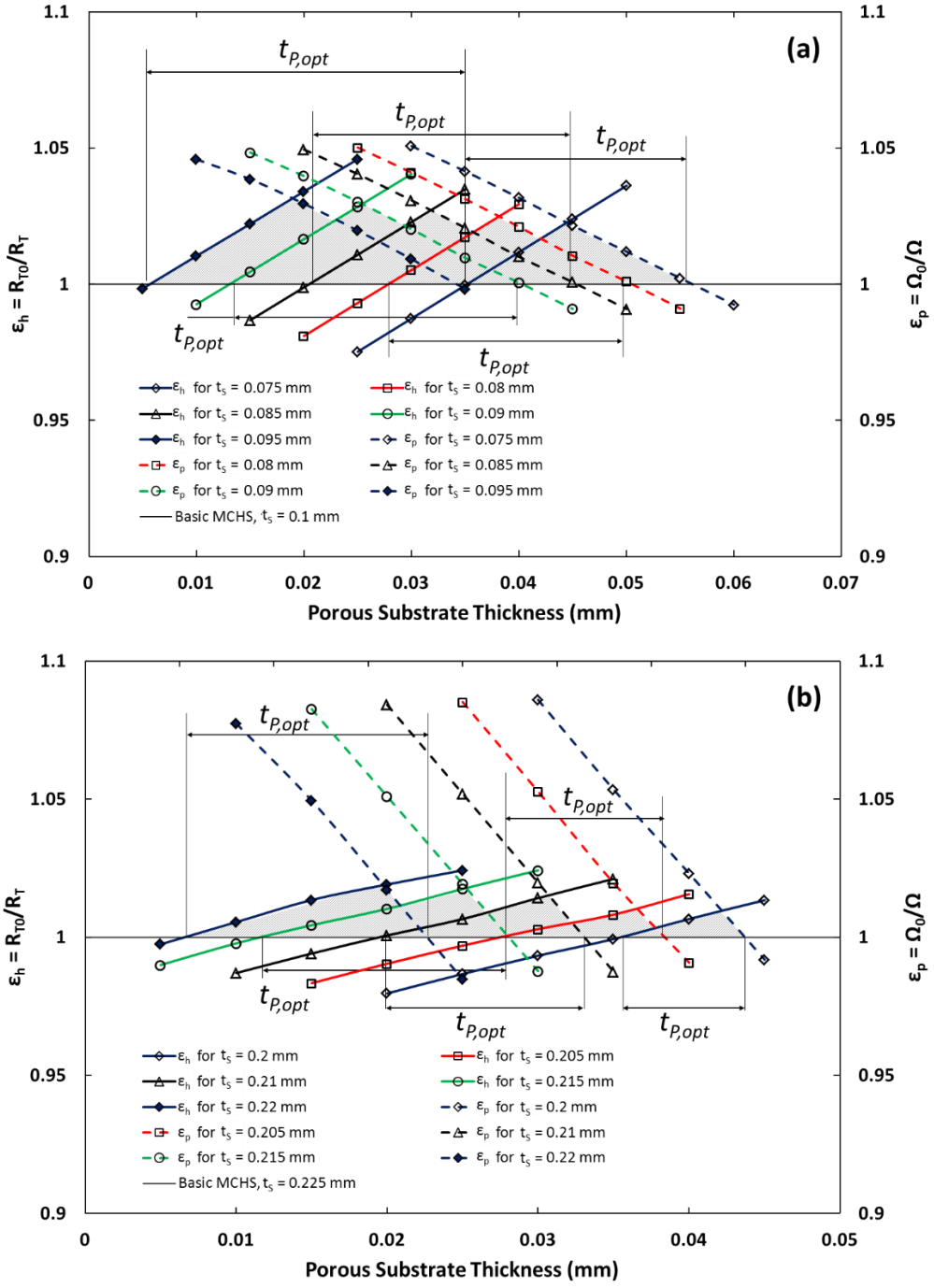

Figure 1-11 Effect of porous substrate thickness on primary thermofluid parameters, ε_h and ε_P, for different vertical solid fin thicknesses around (a) $t_S = 0.1$ mm and (b) $t_S = 0.225$ mm. (Dash lines represent ε_P and solid lines represent ε_h)

The variations of performance parameters ε_h and ε_P for solid thickness $t_S = 0.275$ are shown in Figure 1-12 where highest heat transfer for the MCHS is observed. As can be seen, the ε_P lines are steeper due to exponential increase in the pressure drop. The ε_h lines rise to a maximum and then decrease by increasing t_P. Since at this solid thickness highest heat transfer is achieved for the assumed geometrical set, smaller porous layer thicknesses have ε_h and ε_P higher than 1. For smaller t_S, increasing t_P will increase ε_h but before ε_h gets to 1, an optimum is reached. Therefore, increasing t_P cannot compensate the lower effective conductivity. However, for t_S close to 0.275 mm, the effective conductivity is close to the basic MCHS, and a range of porous substrate thickness is observed which increases the heat transfer and decreases the pressure drop at the same time. The optimum range for t_P at $t_S = 0.27$ mm, is shown in Figure 1-12 as well as the dashed area in which ε_h and ε_P are larger than 1 simultaneously.

ε_h and ε_P variations at various porous substrate thicknesses for the bottom fin thickness of $t_S = 0.095$ mm is shown in Figure 1-13 with a comparison to the conventional MCHS with $t_S = 0.1$ mm. ε_h lines rise to a maximum and then decreases while ε_P lines continually increase. When the top and bottom fins are studied, increasing the porous substrate thickness results in a decrease in the pumping power until a minimum is achieved. Further increasing the thickness of the porous substrate will increase the pumping power. Therefore, for the fin thicknesses below the optimal pumping power point, ε_P lines show an ascending trend. The pumping power effectiveness curve for this case is included in Figure 1-13. For the top fin, variations of ε_h and ε_P have a similar trend. Similar to the discussed results for the vertical fins, a range of porous substrate thickness is also observed here for solid thicknesses smaller than the thermal optimum point, which can decrease the thermal resistance and pumping power simultaneously.

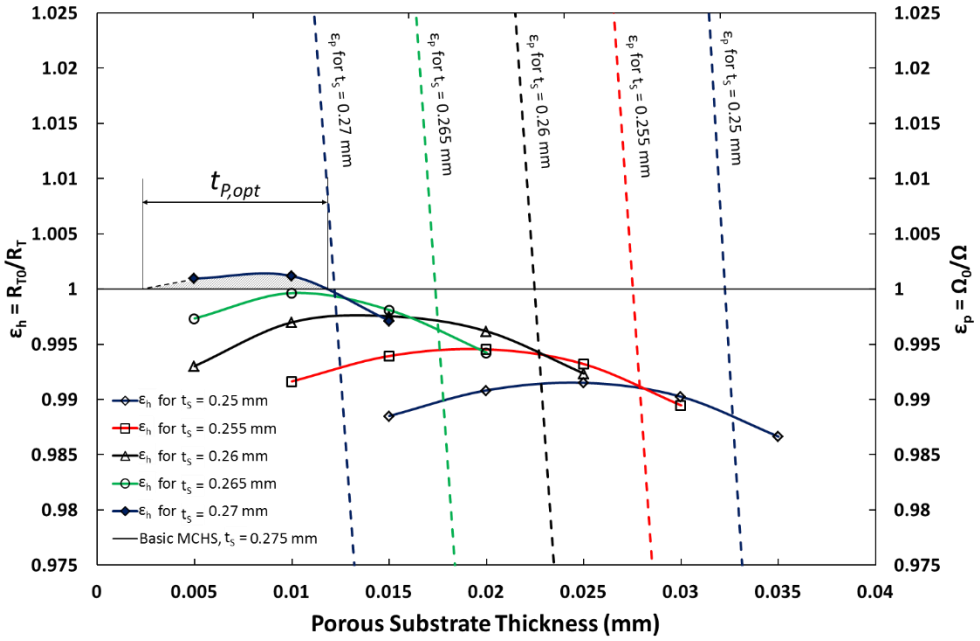

Figure 1-12 Effect of porous substrate thickness on primary thermofluid parameters, ε_h and ε_P, for different vertical solid fin thicknesses around $t_S = 0.275$ mm. (Dash lines represent ε_P and solid lines represent ε_h)

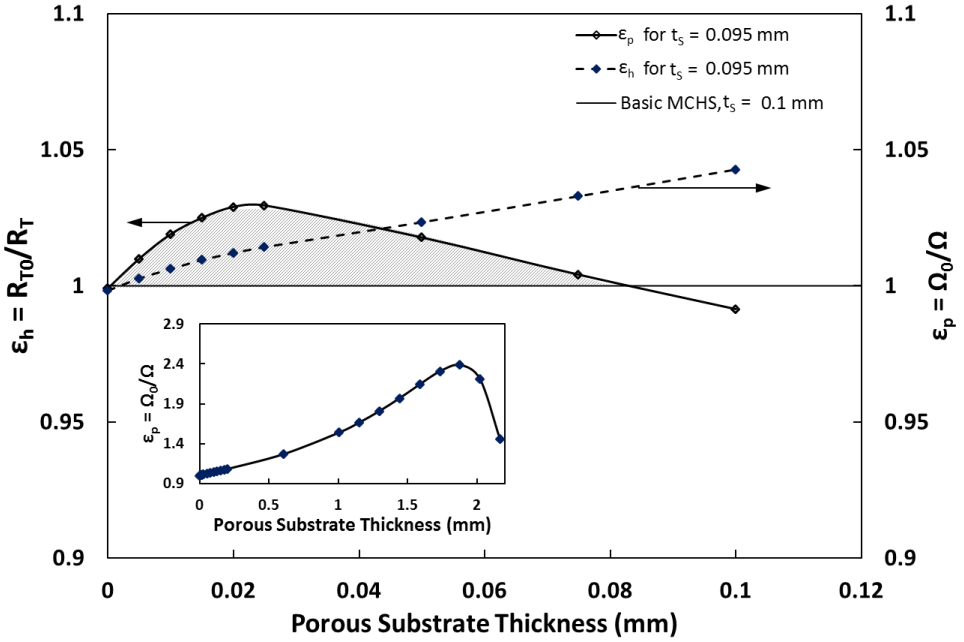

Figure 1-13 Effect of porous substrate thickness on primary thermofluid parameters, ε_h and ε_P, for bottom solid fin thickness of $t_S = 0.095$ mm. (Dash line represents ε_P and solid line represents ε_h)

The general proposed porous MCHS setup is shown in Figure 1-14. When the thickness of the solid fin is reduced and replaced by a porous substrate, the hydraulic performance is improved due to the lower pressure drop. However, this may reduce the total heat transfer coefficient because of the lower effective thermal conductivity. Adding an additional porous substrate can compensate for the thermal loss while the pressure drop is still lower compared to the reference conventional MCHS. Therefore, the solid reduction and porous substrate thicknesses can be chosen based on a multi-objective optimization so that the heat transfer increase while the pumping power is reduced.

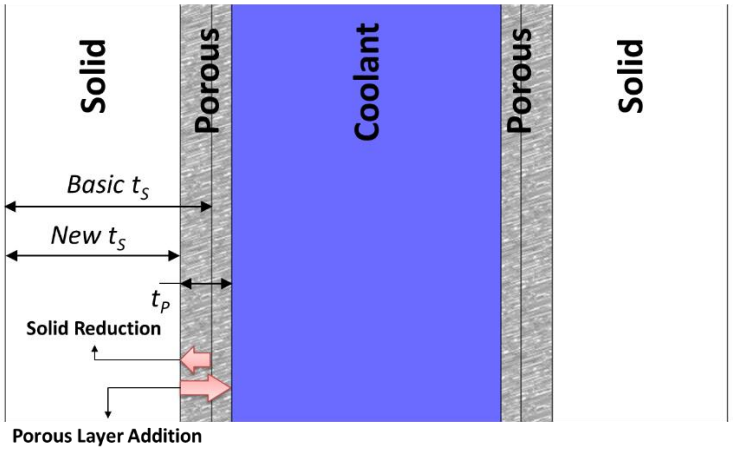

Figure 1-14 Porous substrate setup for a microchannel heat sink to improve hydraulic and thermal performance.

4.3 Effect of Velocity, Material, and Porosity

In this section, we discuss the effects of operating parameters such as velocity, heat sink material, and porosity of the porous substrates on the performance of the studied porous MCHSs. Effect of inlet velocity on thermal resistance and FOM of the porous MCHS is shown in Figure 1-15 for various solid fin thicknesses. The thermal resistance and FOM are shown for a porous substrate thickness of $t_P = 0.025$ mm with varying solid thickness for three inlet velocities, $u =$ 0.2 m/s, $u = 1$ m/s, and $u = 2$ m/s. As can be seen, increasing the inlet velocity reduces the thermal

resistance but more pumping power is required for operating the porous MCHS. The optimum heat transfer point is moved towards the higher solid-porous fin thicknesses. This is due to higher convective heat transfer coefficient of the flow at higher velocities which allows a larger solid-porous fin. Porous MCHSs with a larger solid/porous fin have a higher effective thermal conductivity, and consequently, higher total heat transfer coefficient and lower thermal resistance.

Using different heat sink materials for the studied porous MCHSs is compared in Figure 1-16. The results for thermal resistance and FOM of porous MCHSs made with copper and steel are shown. Similar to the case of steel, when copper is used as the heat sink material, an optimum solid thickness is observed for heat transfer. Also, the lowest thermal resistance of the porous MCHSs mad of copper occurs at lower porous thicknesses. The same behavior can be seen for the highest FOM. Because of higher conductivity of copper, porous-MCHSs made of copper have lower thermal resistance compared to the steel porous-MCHSs. The FOM lines show that adding porous substrate can increase the thermal performance of the MCHSs while reducing the pressure drop. Steel MCHSs have slightly higher FOM implying that using a porous substrate is slightly more effective for a steel MCHS which has a lower thermal conductivity. The optimum FOM point for copper is at a smaller solid thickness compared to steel. This is because optimum FOM occurs at slightly lower solid thicknesses than the optimum thermal resistance points for both materials.

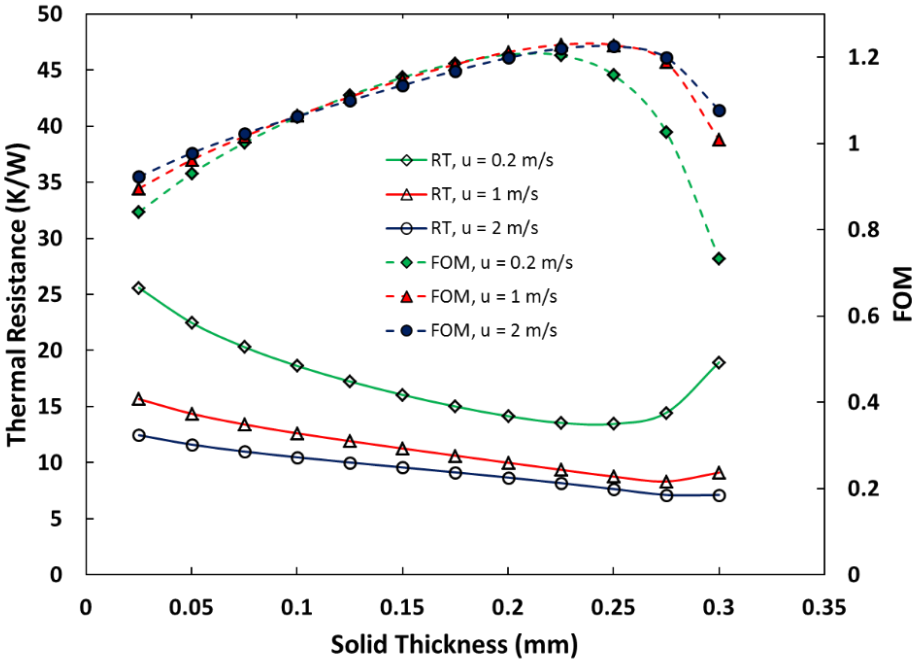

Figure 1-15 Effect of vertical solid thickness and inlet velocity on the thermal resistance and Figure of Merit for $t_P = 0.025$ mm. (Dash lines represent FOM and solid lines represent thermal resistance)

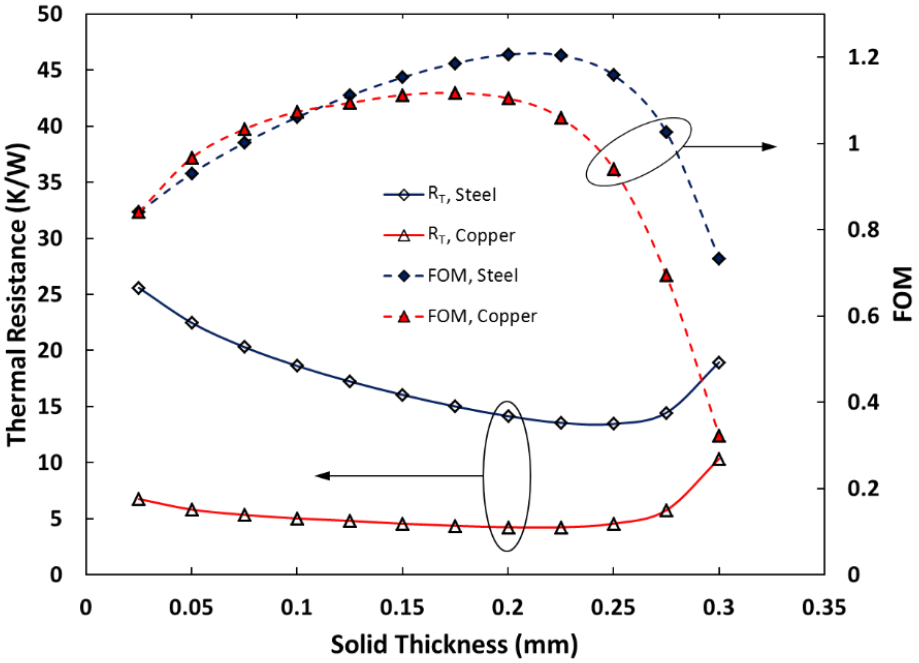

Figure 1-16 Comparison of thermal resistance and Figure of Merit for steel and copper microchannel heat sinks. (Dash lines represent FOM and solid lines represent thermal resistance)

The effect of porosity of the porous substrates on the performance of the MCHSs is shown in Figure 1-17. Thermal resistance and Figure of Merit is compared when porous substrates with porosity of 0.32 and 0.44 and thickness of $t_P = 0.025$ mm are placed on the fins as surface treatment. Thermal resistance for different porosities is also shown for various vertical wall solid thicknesses and porous substrate thickness of $t_P = 0.1$ mm. For both porosities there is an optimum point for the thermal resistance and Figure of Merit. Higher MCHSs thermal performance is found at lower porous substrate thicknesses. Between the two porosities, thermal resistance of MCHSs with porosity of 0.32 is lower than MCHSs with higher porosity of 0.44. Moreover, at higher porosities the pumping power is reduced, and it is easier for the coolant to pass through the channel. When considering both thermal and hydraulic aspects, pumping power reduction is more significant than the increase in thermal resistance. As can be seen in Figure 1-17, FOM for MCHSs with porosity of 0.44 is higher than the MCHSs with porosity of 0.32, and a decrease in pressure drop at a higher porosity is more effective than an increase in thermal resistance. Furthermore, an increase in thermal resistance for higher solid thicknesses is relatively small due to the small thickness of the porous layer compared to the solid layer. Thermal resistance is also compared at a larger porous layer thickness of $t_P = 0.1$ mm for the two considered porosities in Figure 1-17. The effect of higher porosity is more noticeable at a higher porous substrate thickness.

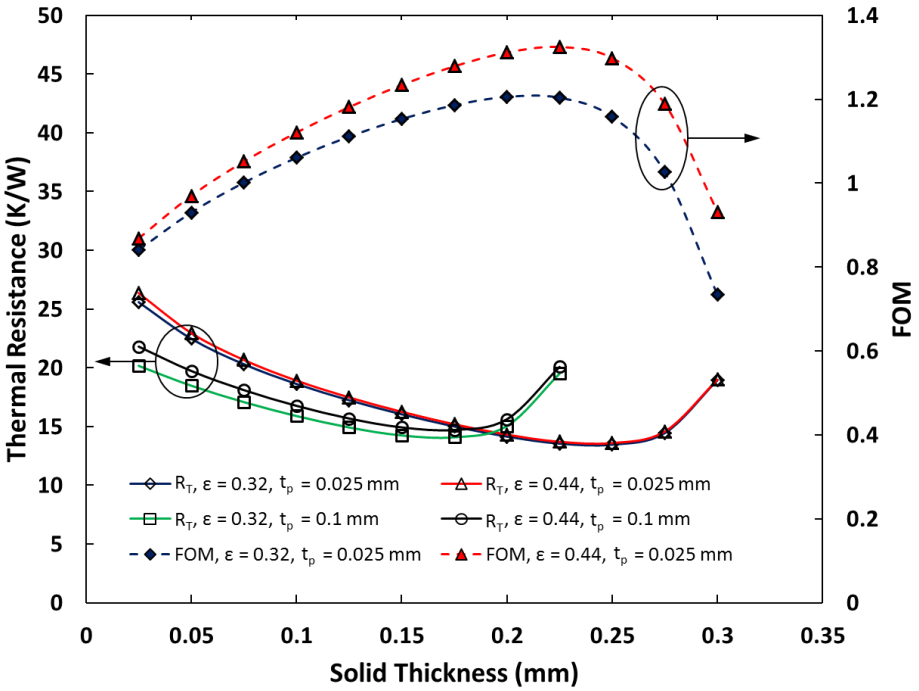

Figure 1-17 Effect of porosity on thermal resistance and Figure of Merit for different vertical solid fin and porous substrate thicknesses. (Dash lines represent FOM and solid lines represent thermal resistance)

5. Conclusions

In the first chapter of this thesis, enhancement effect of porous substrates as surface treatment on the microchannel heat sinks is investigated. Optimized designs with respect to heat transfer and pumping power are discussed in detail. Following are the conclusions of this study:

- Porous substrates can potentially increase the thermal and hydraulic performance of conventional microchannel heat sinks. If the solid and porous substrate thicknesses are carefully selected based on an optimization study, the optimized design can decrease the thermal resistance and the required pumping power simultaneously.

- An optimum fin thickness is observed for the studied MCHS which results in the highest total heat transfer coefficient. At fin thicknesses below this point, adding porous substrate increases the heat transfer coefficient while imposing lower pressure drop compared to a fully solid domain. After the optimum point, adding more porous substrate has an adverse effect on heat transfer and the pressure drop.

- Figure of Merit can be used to compare MCHSs considering both heat transfer coefficient and pressure drop factors at the same time. For all conventional MCHSs studied here, a porous MCHS design is found that can increase the FOM.

- At higher flow rates, thermal resistance is reduced while the pressure drop increases, and the optimum thermal and FOM points occur at higher porous-solid thicknesses. For heat sinks with higher conductive materials, lower thermal resistance can be achieved at the same pressure drop levels, and optimum thermal and FOM point occur at smaller porous-solid fin thicknesses.

- At higher porosities, the pumping power decreases and the thermal resistance increases, but the rise in the thermal resistance is not as significant as the reduction in the pumping power. Effect of porosity is more significant at larger porous substrate thicknesses.

References

[1] A. Adham, N. Mohd-Ghazali and R. Ahmad, "Thermal and hydrodynamic analysis of microchannel heat sinks: A review," Renew sustain Energy Rev, vol. 21, pp. 614-22, 2013.

[2] B. Agostini, M. Fabbri, J. Park, L. Wojtan, J. Thome and B. Michel, "State of the art of high heat flux cooling technologies," Heat Transfer Eng., vol. 28, p. 258–281, 2007.

[3] C. Zhao and T. Lu, "Analysis of microchannel heat sinks for electronics cooling," International Journal of Heat and Mass Transfer, vol. 45, pp. 4857-4869, 2002.

[4] I. Hassan, P. Phutthavong and M. Abdelgawad, "Micro-channel Heat Sinks, An Overview of the State-of-the-Art," Microscale Thermophysical Engineering, vol. 8, pp. 183-205, 2004.

[5] I. Mudawar, "Assessment of high-heat-flux thermal management schemes," Trans. Compon. Packag. Technol. , vol. 24, p. 122–141, 2001.

[6] P. Smakulski and S. Pietrowicz, "A review of the capabilities of high heat flux removal by porous materials, microchannels and spray cooling techniques," Applied Thermal Engineering, vol. 104, pp. 636-646, 2016.

[7] D. B. Tuckerman, "Heat-Transfer Microstructures for Integrated Circuits," Stanford University, 1984.

[8] D. B. Tuckerman and F. R. Pease, "Microcapillary Thermal Interface Technology for VLSI Packaging," Digest of Technical Papers—Symposium on VLSI Technology, pp. 60-61, 1983.

[9] Y. Hadad, B. Ramakrishnan, R. Pejman, S. Rangarajan, P. R. Chiarot, A. Pattamatta and B. Sammakia, "Three-objective shape optimization and parametric study of a micro-channel heat sink with discrete non-uniform heat flux boundary conditions," Applied Thermal Engineering, vol. 150, pp. 720-737, 2019.

[10] A. Weisberg, H. Bau and J. Zemel, "Analysis of microchannels for integrated cooling," Int. J. Heat Mass Transf, vol. 35 , pp. 2465-2474, 1992.

[11] T. Harms, M. Kazmierczak and F. Gerner, "Developing convective heat transfer in deep rectangular microchannels," Int. J. Heat Fluid Flow, vol. 20, pp. 149-157, 1999.

[12] A. Fedorov and R. Viskanta, "Three-dimensional conjugate heat transfer in the microchannel heat sink for electronic packaging," Int. J. Heat Mass Transf., vol. 43, pp. 399-415, 2000.

[13] R. Chein and J. Chen, "Numerical study of the inlet/outlet arrangement effect on microchannel heat sink performance," Int. J. Therm. Sci., vol. 48, pp. 1627-1638, 2009.

[14] S. Kim and D. Kim, "Forced convection in microstructures for electronic equipment cooling," J. Heat Transf., vol. 3, pp. 639-645, 1999.

[15] W. Qu and I. Mudawar, "Analysis of three-dimensional heat transfer in micro-channel heat sinks," Int. J. Heat Mass Transf., vol. 45, pp. 3973-3985, 2002.

[16] J. Ryu, D. Choi and S. Kim, "Numerical optimization of the thermal performance of a microchannel heat sink," Int. J. Heat Mass Transf., vol. 45, pp. 2823-2827, 2002.

[17] Z. Y. Guo and Z. Li, "Size Effect on Single-Phase Channel Flow and Heat Transfer at Microscale," International Journal of Heat and Fluid Flow, vol. 24, p. 284–297, 2003.

[18] S. Lu and K. Vafai, "A comparative analysis of innovative microchannel heat sinks for electronic cooling," International Communications in Heat and Mass Transfer, vol. 76, p. 271–284, 2016.

[19] K. Vafai and L. Zhu, "Analysis of two-layered micro-channel heat sink concept in electronic cooling," International Journal of Heat and Mass Transfer, vol. 42, pp. 2287-2297, 1999.

[20] S. Chong, K. Ooi and T. Wong, "Optimisation of single and double layer counter flow microchannel heat sinks," Appl. Therm. Eng., vol. 22, pp. 1569-1585, 2002.

[21] X. Wei, Y. Joshi and M. Patterson, "Experimental and numerical study of a stacked microchannel heat sink for liquid cooling of microelectronic devices," J. Heat Transf., vol. 129, pp. 1432-1444, 2007.

[22] T. Hung, W.-M. Yan and W.-P. Li, "Analysis of heat transfer characteristics of double-layered microchannel heat sink," Int. J. Heat Mass Transf., vol. 55, pp. 3090-3099, 2012.

[23] A. Khaled and K. Vafai, "Cooling augmentation using microchannels with rotatable separating plates," International Journal of Heat and Mass Transfer, vol. 54, p. 3732–3739, 2011.

[24] K. Vafai and A. Khaled, "Analysis of flexible micro-channel heat sink systems," International Journal of Heat and Mass Transfer, vol. 48, p. 1739–1746, 2005.

[25] A. Haji-Sheikh, D. Nield and K. Hooman, "Heat transfer in the thermal entrance region for flow through rectangular porous passages," International Journal of Heat and Mass Transfer, vol. 49, p. 3004–3015, 2006.

[26] A. Zehforoosh and S. Hossainpour, "Numerical investigation of pressure drop reduction without surrendering heat transfer enhancement in partially porous channel," International Journal of Thermal Sciences, vol. 49, p. 1649–1662, 2010.

[27] V. Calmidi and R. Mahajan, "Forced convection in high porosity metal foams," ASME Journal of Heat Transfer, vol. 122, p. 557–565, 2000.

[28] J. Stark, R.Prasad and T.L.Bergman, "Experimentally validated analytical expressions for the thermal efficiencies and thermal resistances of porous metal foam-fins," International Journal of Heat and Mass Transfer, vol. 111, pp. 1286-1295, 2017.

[29] G. Hetsroni, M. Gurevich and R. Rozenblit, "Sintered porous medium heat sink for cooling of high-power mini-devices," International Journal of Heat and Fluid Flow, vol. 27, p. 259–266, 2006.

[30] B. Wang, Y. Hong, L. Wang, X. Fang, P. Wang and Z. Xu, "Development and numerical investigation of novel gradient-porous heat sinks," Energy Conversion and Management, vol. 106, pp. 1370-1378, 2015.

[31] T. Hung and W. Yan, "Thermal performance enhancement of micro-channel heat sinks with porous metallic medium," Numerical Heat Transfer Part A: Application, vol. 63, p. 666–686, 2013.

[32] T. Hung, Y. Huang and W. Yan, "Thermal performance analysis of porous-microchannel heat sinks with different configuration designs," International Journal of Heat and Mass Transfer, vol. 66, pp. 235-243, 2013.

[33] Z. Wan, J. Liu, K. Su, X. Hu and S. M, "Flow and heat transfer in porous micro heat sink for thermal management of high power LEDs," Microelectronics Journal, vol. 42, p. 632–637, 2011.

[34] R. Singh, A. Akbarzadeh and M. Mochizuki, "Sintered porous heat sink for cooling of high-powered microprocessors for server applications," International Journal of Heat and Mass Transfer, vol. 52, p. 2289–2299, 2009.

[35] T. Jeng, S. Tzeng and F. Tang, "Fluid flow and heat transfer characteristics of the porous metallic heat sink with a conductive cylinder partially filled in a rectangular channel," International Journal of Heat and Mass Transfer, vol. 53, p. 4216–4227, 2010.

[36] H. Shen, X. Liu, H. Yan, G. Xie and B. Sunden, "Enhanced Thermal Performance of Internal Y-Shaped Bifurcation Microchannel Heat Sinks With Metal Foams," ASME. J. Thermal Sci. Eng. Appl., vol. 10, pp. 011001-011001-8, 2017.

[37] P. Huang and K. Vafai, "Flow and heat transfer control over an external surface using a porous block array arrangement," International Journal of Heat and Mass Transfer, vol. 36, pp. 4019-4032, 1993.

[38] P. Huang and K. Vafai, "Passive alteration and control of convective heat transfer utilizing alternate porous cavity-block wafers," International Journal of Heat and Fluid Flow, vol. 15, pp. 48-61, 1994.

[39] Y. Ould-Amer, S. Chikh, K. Bouhadef and G. Lauriat, "Forced convection cooling enhancement by use of porous materials," International Journal of Heat and Fluid Flow, vol. 19, pp. 251-258, 1998.

[40] Y.-T. Yang and C.-Z. Hwang, "Calculation of turbulent flow and heat transfer in a porous-baffled channel," International Journal of Heat and Mass Transfer, vol. 46, pp. 771-780, 2003.

[41] P.-X. Jiang, M. Li, T.-J. Lu, L. Yu and Z.-P. Ren, "Experimental research on convection heat transfer in sintered porous plate channels," International Journal of Heat and Mass Transfer, vol. 47, pp. 2085-2096, 2004.

[42] K.Hooman, "Heat and fluid flow in a rectangular microchannel filled with a porous medium," International Journal of Heat and Mass Transfer, vol. 51, pp. 5804-5810, 2008.

[43] S. Dathathri and C. Balaji, "Heat transfer and optimization studies on layered porous stackings under an imposed pressure drop," International Communications in Heat and Mass Transfer, vol. 60, pp. 32-36, 2015.

[44] L. Chuan, X.-D. Wang, T.-H. Wang and W.-M. Yan, "Fluid flow and heat transfer in microchannel heat sink based on porous fins," International Communications in Heat and Mass Transfer, vol. 65, p. 52–57, 2015.

[45] G. Lu, J. Zhao, L. Lin, X.-D. Wang and W.-M. Yan, "A new scheme for reducing pressure drop and thermal resistance simultaneously in microchannel heat sinks with wavy porous fins," International Journal of Heat and Mass Transfer, vol. 111, pp. 1071-1078, 2017.

[46] B. Alazmi and K. Vafai, "Analysis of Fluid Flow and Heat Transfer Interfacial Conditions between a Porous Medium and a Fluid Layer," International Journal of Heat and Mass Transfer, vol. 44, pp. 1735-1749 , 2001.

[47] A. Amiri, K. Vafai and T. M. Kuzay, "Effect of Boundary Conditions on Non-Darcian Heat Transfer Through Porous Media and Experimental Comparisons," Numerical Heat Transfer Journal Part A, vol. 27, pp. 651-664, 1995.

[48] K. Vafai and R. Thiyagaraja, "Analysis of Flow and Heat Transfer at the Interface Region of a Porous Medium," International Journal of Heat and Mass Transfer, vol. 30, pp. 1391-1405, 1987.

[49] K. Vafai, "Convective Flow and Heat Transfer in Variable Porosity Media," Journal of Fluid Mechanics, vol. 25, pp. 233-259, 1984.

[50] K. Vafai and C. Tien, "Boundary and inertia effects on flow and heat transfer in porous media," Int. J. Heat Mass Transfer, vol. 24, p. 195–203, 1981.

[51] C. Hsu and P. Cheng, "Thermal dispersion in a porous medium," International Journal of Heat and Mass Transfer, vol. 33, pp. 1587-1597, 1990.

[52] A. Ghahremannezhad and K. Vafai, "Thermal and hydraulic performance enhancement of microchannel heat sinks utilizing porous substrates," International Journal of Heat and Mass Transfer, vol. 122, pp. 1313-1326, 2018.

[53] A. Ghahremannezhad, H. Xu, M. A. Nazari, M. H. Ahmadi and K. Vafai, "Effect of porous substrates on thermohydraulic performance enhancement of double layer microchannel heat sinks," International Journal of Heat and Mass Transfer, vol. 131, pp. 52-63, 2019.

[54] S. Patankar, Numerical Heat Transfer and Fluid Flow, Hemisphere/McGraw-Hill, 1980.

Chapter 2: Thermohydraulic Enhancement in Double-Layered MCHSs with Porous Substrates

Nomenclature:

A	Heat sink's bottom surface area (m^2)
C	Forchheimer's constant
c_f	Heat capacity of the coolant (J kg^{-1} K^{-1})
c_s	Heat capacity of the solid (J kg^{-1} K^{-1})
D_h	Hydraulic diameter of the channel (m)
f	Friction factor
FOM	Figure of merit
h_m	Average heat transfer coefficient (W m^{-2} K^{-1})
k_e	Effective thermal conductivity of the porous medium (W m^{-1} K^{-1})
k_f	Thermal conductivity of the coolant (W m^{-1} K^{-1})
k_s	Thermal conductivity of the solid (W m^{-1} K^{-1})
K_p	Permeability of the porous medium (m^2)
l_f	Height of channel at inlet (m)
L_x	Length of the heat sink (m)

L_y	Height of the heat sink (m)
L_z	Width of the heat sink (m)
N	Number of channels
Nu	Nusselt number
P	Pressure (Pa)
P_{out}	Outlet pressure (Pa)
q_w	Heat flux on the base surface of the heat sink (W m^{-2})
$\dot{Q}$	Volume flow rate of the channel (m^3 s^{-1})
Re	Reynolds number
R_T	Thermal resistance (K W^{-1})
T_{in}	Inlet temperature (K)
T_w	Wall temperature at the centerline of the base surface (K)
$\overline{T}_w$	Average temperature along the base surface (K)
$T_{w,max}$	Maximum wall temperature of the heat sink
t_B	Thickness of the solid at bottom part of channel (m)
t_T	Thickness of the solid at top part of channel (m)
t_S	Thickness of the solid fins (m)

t_P	Thickness of the porous treatment (m)
u_{in}	Inlet velocity of the coolant (m s^{-1})
$\vec{V}$	Velocity vector (m s^{-1})
W_O	Total width of a single channel (m)
W_f	Width of the coolant pathway (m)
x	x coordinate
y	y coordinate
z	z coordinate

Greek symbols:

ε	Porosity
ΔP	Pressure drop from the inlet to the outlet (Pa)
μ_f	Dynamic viscosity (kg m^{-1} s^{-1})
ρ_s	solid density (kg m^{-3})
ρ_f	Coolant density (kg m^{-3})
Ω	Pumping power of a channel (W)
ε_h	Average heat transfer coefficient ratio
ε_p	Pumping power effectiveness

Subscripts:

e	Effective property of the porous medium
f	Fluid phase
m	Mean value
p	Porous medium
s	Solid phase

1. Introduction

As discussed in chapter 1, the high heat fluxes generated in high performing circuits is a major challenge and microchannel heat sinks are cooling devices introduced for thermal management of such systems [1-18]. Many studies have worked to increase the heat transfer capability of MCHSs and proposed new techniques [19]. One of the techniques to improve the performance of the microchannel heat sinks is using double or multilayer microchannels which are stacked over each other and the coolant passes through them with an opposite direction. A double layer microchannel heat sink with counter current flow arrangement have been proposed by Vafai and Zhu [20]. A performance comparison with single layered MCHSs showed that temperature rise in double layered MCHSs have been significantly reduced and a more uniform cooling is achieved. Also, a lower pressure drop is achieved compared to the single-layered MCHSs at the same heat transfer level. Optimal thermal resistance for single and double layered MCHSs is discussed in the optimization study of Chong et al. [21]. Wei et al. [22] performed experimental and numerical

studies on stacked microchannel heat sinks and examined different flow arrangements. It was founded that counterflow arrangement provided more uniform temperature profile. Heat transfer and pressure drop in a double layer MCHS for different flow conditions and channels' height is studied by Xie et al. [23]. Characteristics of double layer MCHS with different materials, coolants, and geomatical parameters is numerically investigated by Hung et al. [24]. Experimental investigations on copper made single layered and double layer MCHSs by Lu et al. [25] showed that at the same level of heat removal, double layered MCHSs require much lower pressure drop. Effect of geometric and flow parameters on the performance of double layered MCHSs and the optimal aspect ratio and flow rate is studied by Wu et al. [26]. A truncated top channel is used in a double layered MCHS by Leng et al. [27, 28] and more uniform bottom temperature and lower thermal resistance are reported.

Another technique that is recently gaining attractions for performance enhancement of microchannel heat sinks is utilization of porous media. In chapter 1, some of the works in this area are briefly mentioned. Studies done by Hooman [29] on MCHSs filled with porous media, Hung et al. [30–32] on using different porous configurations in MCHSs, Chuan et al. [33] on using porous fins in MCHSs, Shen et al. [34,35] on using an internal Y-shaped porous bifurcation inside the microchannels, and others [36, 37] are some examples working on this subject. However, studies that have utilized porous media in double layered MCHSs are very rare. In a recent study, Wang et al. [38] have used porous fins in a double-layered MCHS and numerically investigated the thermal resistance and pumping power at a wide range of Reynolds numbers. The porous double-layered designs indicated 45.3–48.5% reduction in pumping power, while only 14.8–16.2% increase in thermal resistance.

In this chapter, we analyze thermal and hydraulic performance of double layered microchannel heat sinks where porous substrates are placed on the vertical fins. A comprehensive

optimization study is performed on the double layered MCHSs to capture the conjugate heat transfer phenomenon at various porous-solid fin thicknesses. We consider two scenarios; first both top and bottom microchannels have the same geometrical properties, and second, the top and bottom microchannels may have different solid and porous fin geometrical properties. To obtain the candidate optimal designs, sensitivity analysis is performed. Finally, the effects of flow rate, porosity, and heat sink material are discussed.

2. Analysis

Three dimensional models of the porous treated double layered MCHSs are constructed in order to investigate the conjugate heat transfer. The schematic of the porous double layered MCHSs is shown in Figure 2-1. The periodic unit used for simulations is shown in Figure 2-2 (a) and the geometrical parameters for one porous double layer microchannel are shown in Figure 2-2 (b). L_x is the length, L_y is the height, and L_z is the width of the MCHS. Each double layer microchannel has a total height of L_y and a width of w_o, half vertical solid fins with thicknesses of t_{SB} and t_{ST} for bottom and top branch respectively, bottom horizontal solid fin with thickness of t_B, middle horizontal solid fin with thickness of t_M, and top horizontal solid fin with thickness of t_T. Two vertical porous structures with thicknesses of t_{PB} for the bottom branch and t_{BT} for the top branch are placed on the vertical solid fins. The coolant is assumed to be pure water, and the solid parts of the heat sink as well as the porous domains are considered to be stainless steel. Opposite flow directions are assumed at the bottom and the top branch for the counter-flow double layer MCHS and the heat is applied at the bottom surface as in most heat sink applications.

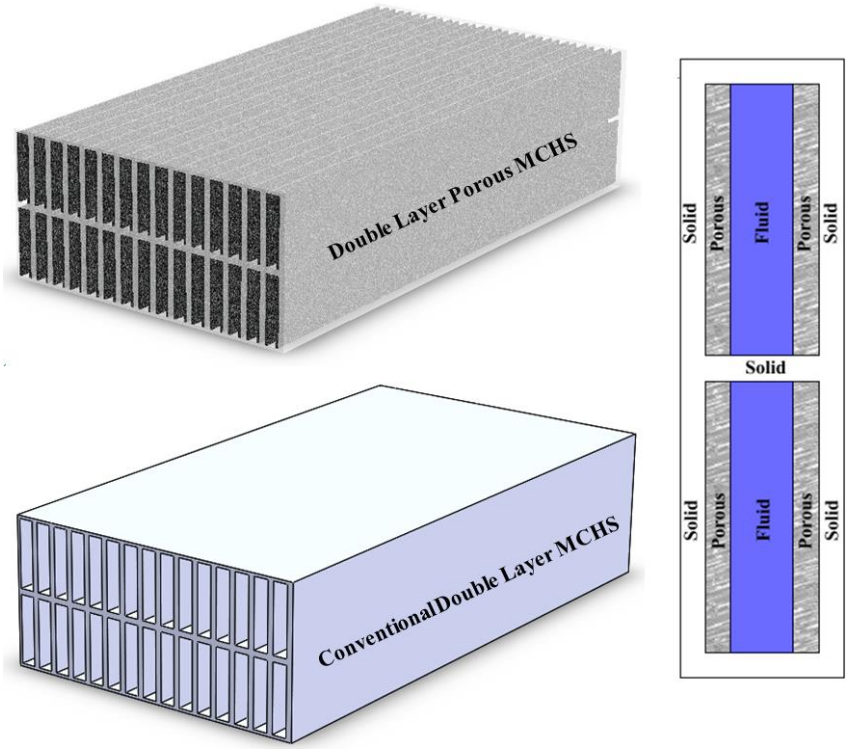

Figure 2-1 Schematic of a conventional double layer MCHS and a double layer porous MCHS.

3. Numerical procedure

Three dimensional models of the double-layered MCHSs are developed and conjugate heat transfer is numerically simulated. The numerical procedure is similar to the single layered MCHSs and the related equations and defined parameters can be found in detail in chapter 1. The total pumping power for double layered MCHSs is defined as:

$$\Omega = \left(\dot{Q}\Delta P\right)_{Bottom} + \left(\dot{Q}\Delta P\right)_{Top} = \left(u_{in} l_f w_f \Delta P\right)_{Bottom} + \left(u_{in} l_f w_f \Delta P\right)_{Top}, \qquad (2\text{-}1)$$

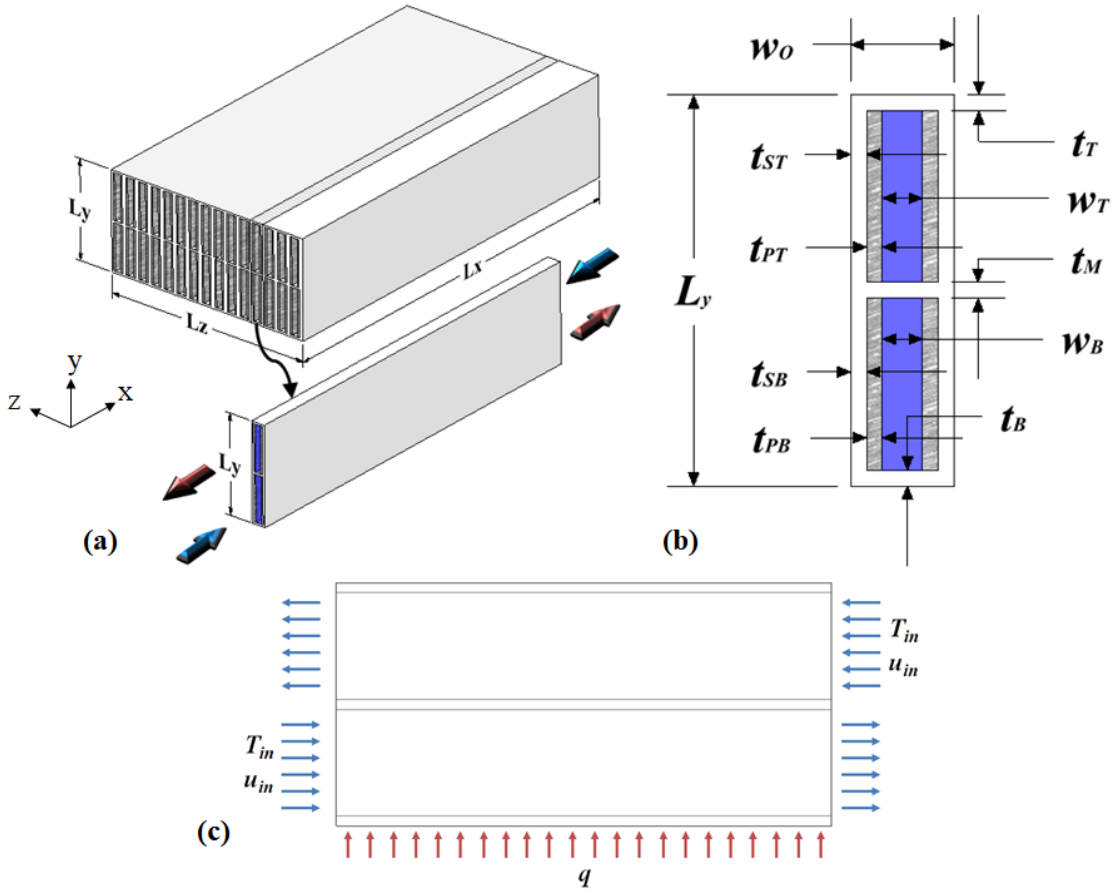

Figure 2-2 (a) Schematic of the proposed double Layer MCHS; A generic channel is used as the simulation domain; (b) Geometric parameters of the generic double layer porous channel; (c) Heat flux is applied at the bottom surface of the channel.

The comparative parameters such as heat transfer effectiveness, pumping power effectiveness, and FOM are defined in a similar way as for the single layer MCHSs. To perform a complete comprehensive parametric optimization with multiple parameters, about 1500 double-layered MCHSs with different geometrical and material properties are simulated. The finite volume approach is employed to numerically solve the governing equations with a SIMPLE (Semi-Implicit Method for Pressure Linked Equations) scheme [39]. Grid independency tests are performed for each case. Heat transfer coefficient and friction factor for three different grids are shown in Table

2-1 for a candidate double-layered MCHS. Based on the results, the grid scheme of 120 × 130 × 50 is selected for reasonable accuracy and computational time. Validation of the developed model for a porous microchannel is described in chapter 1.

Table 2-1 Grid independency examination

Grid	Number of nodes	h_m (kW m^{-1} K^{-1})	f
100 × 100 × 40	400000	8.0819	0.12137
120 × 130 × 50	780000	8.0801	0.12130
140 × 180 × 60	1512000	8.0796	0.12128

4. Results and discussion

Different solid and porous fin thicknesses for the bottom and top microchannels are studied to reveal the thermal and hydraulic behavior of the different double layered MCHSs through parametric optimization. To perform such an optimization, we define two scenarios. First, the bottom and top microchannels are identical, and both solid and porous thicknesses for both microchannels are the same. Second scenario is where the porous and solid thicknesses for the bottom and top microchannels can be different. For all studied cases, a basic conventional double layered MCHS with no porous substrates is considered to be the reference for comparison. For the reference double-layered MCHS, the vertical solid fin of the bottom and top channels are $t_{SB} = t_{ST} = 0.1$ mm, and the thickness of the horizontal bottom, middle, and top solid fins are $t_B = 0.1$ mm, $t_M = 0.1$ mm, and $t_T = 0.1$ mm, respectively. The performance of the new designs is evaluated based on comparing them with the basic double layered MCHS. Thermo-physical properties of the coolant, the solid domains, and the porous substrates are listed in Table 2-2. Assumed values for the geometrical parameters of the double-layered MCHSs are listed in Table 2-3.

Table 2-2 Thermal properties of coolant, solid section, and porous structure

Materials	ρ (kg m^{-3})	C_p (J kg^{-1} K^{-1})	k (W m^{-1} K^{-1})	μ (Pa s)
Coolant: Pure water	998.2	4182	0.6	0.000855
Substrate: Steel	8030	8030	16.27	
Porous medium: Steel	8030	8030	16.27	

Table 2-3 Geometrical parameters used for the double-layered porous MCHSs.

Parameter	Value
L_x (mm)	10
L_y (mm)	3
L_z (mm)	12.2
w_o (mm)	0.8
w_B (mm)	0.05 - 0.7
w_T (mm)	0.05 - 0.7
t_T (mm)	0.1
t_B (mm)	0.1
t_M (mm)	0.1
t_{PB} (mm)	0.005 – 0.35
t_{PT} (mm)	0.005 – 0.35
t_{SB} (mm)	0.025 – 0.35
t_{ST} (mm)	0.025 – 0.35

4.1 Heat Transfer and Pumping Power

4.1.1 First Scenario

Here, we analyze the thermal and hydraulic behavior of the porous double-layered MCHSs when both bottom and top channels are identical. Therefore, they have the same solid and porous fin thicknesses ($t_{SB} = t_{ST}, t_{PB} = t_{PT}$). The vertical solid fin thicknesses of the bottom and top channels are from 0.025 mm to 0.3 mm while for each solid thickness, the bottom and top porous substrate thicknesses are changed from 0.025 mm to 0.275 mm.

Figure 2-3 shows the average heat transfer coefficient of double-layered MCHSs for different solid fin thicknesses versus porous substrate thickness. For the majority of the solid fin thicknesses, increasing the thickness of the porous substrate results in increase of the average heat transfer coefficient until an optimum point is reached. Further addition of porous substrate after this point results in a decrease of heat transfer coefficient. Moreover, for a specific porous substrate thickness, increasing the solid thickness also increases the heat transfer coefficients. Average heat transfer coefficient of the reference double-layered MCHS with a solid fin thickness of $t_{SB} = t_{ST} =$ 0.1 mm is also shown in Figure 2-3 with a straight line. For all double-layered porous MCHSs, there is a range of the porous fin thickness that the average heat transfer coefficient is higher than that of the basic MCHS. The highest thermal performance is observed at higher solid fin thickness of $t_{SB} = t_{ST} = 0.3$ mm and low porous fin thickness of $t_{PB} = t_{PT} = 0.025$ mm.

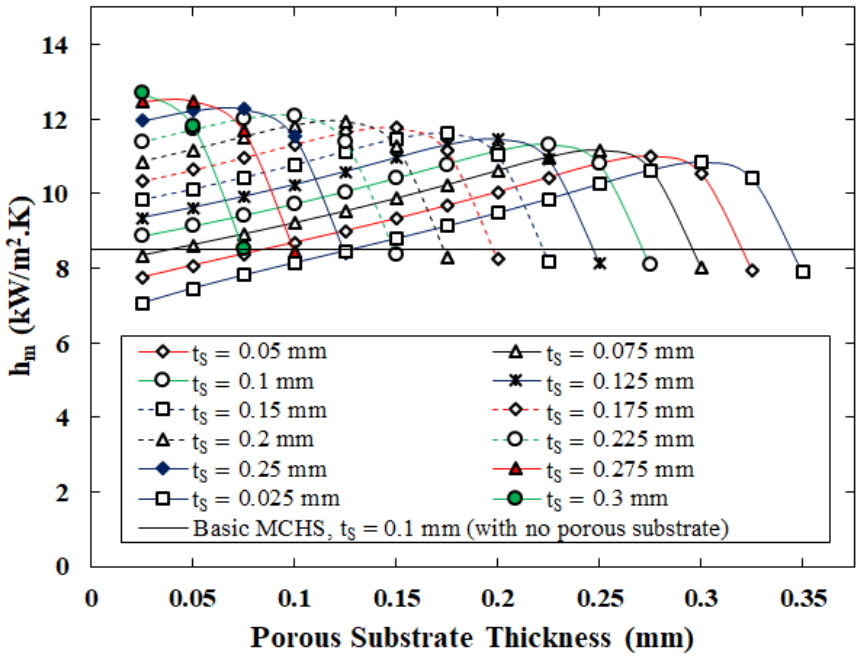

Figure 2-3 Heat transfer coefficient of double-layered porous MCHSs with different bottom and top solid fin thicknesses ($t_S = t_{SB} = t_{ST}$) versus bottom and top porous substrate thicknesses ($t_P = t_{PB} = t_{PT}$).

As discussed, better thermal performance occurs at higher solid-porous fin thickness, but higher pressure drops also occur at larger fin thickness as shown in Figure 2-4. Pressure drop is plotted for double-layered porous MCHSs with different solid fin thicknesses versus porous substrate thickness. Pressure drop of the basic double-layered MCHS is also shown as reference with the black straight line. As can be seen, increase in the thickness of the porous substrate results in increase of the pressure drop. At larger solid-porous fin thickness the increase is exponential. Also, at a certain porous substrate thickness, increasing the solid fin thickness will increase the pressure drop.

To evaluate both improvements in thermal and hydraulic aspects, Figure of Merit (FOM) is used when comparing a new design to a basic design [32,36,40,41]. In Figure 2-5, FOM is plotted for double-layered MCHSs with different solid fin thicknesses versus their porous substrate thickness. For solid fin thicknesses from 0.025 to 0.225 mm, FOM first increases by adding porous substrate until an optimum point is reached and then starts to decrease. For bigger solid fin thicknesses from 0.225 to 0.3 mm which are closer to the optimal heat transfer point, adding porous substrate results in a decrease of FOM. This is due to higher role of pressure drop in FOM compared to heat transfer at larger solid-porous fin thicknesses. The same behavior can be observed when considering effect of varying solid fin thickness at a constant porous substrate thickness. FOM increases by increasing t_{SB} and t_{ST} until an optimum point and then starts to decrease. Highest FOM occurs for the double-layered MCHS with a t_{SB} and t_{ST} close to (but smaller than) the optimal heat transfer point and small t_{PB} and t_{PT}. This double-layered MCHS has only 5% lower heat transfer coefficient compared to the double-layered MCHS with the highest h_m, while having 58% lower pressure drop. This suggests that FOM can be a reliable and useful performance parameter when choosing a candidate MCHS considering both thermal and hydraulic aspects.

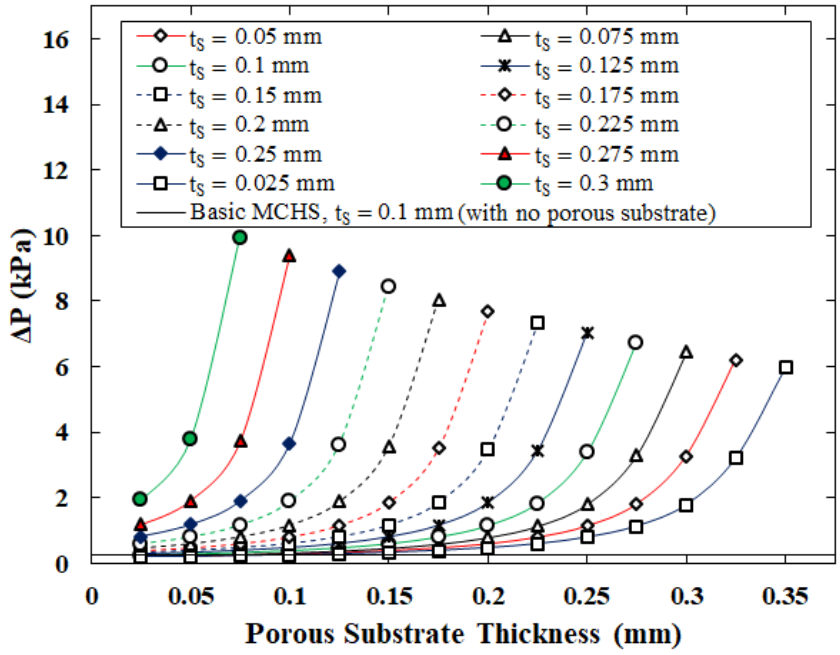

Figure 2-4 Pressure drop of double-layered porous microchannel heat sinks versus the bottom and top porous substrate thicknesses ($t_P = t_{PB} = t_{PT}$) for different bottom and top solid thicknesses ($t_S = t_{SB} = t_{ST}$).

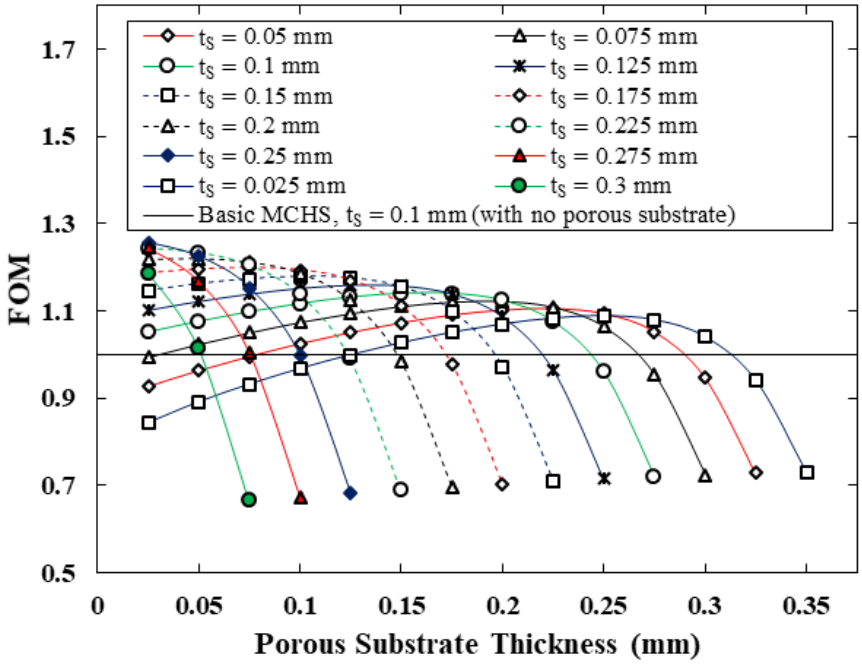

Figure 2-5 FOM of double-layered porous microchannel heat sinks versus the bottom and top porous substrate thicknesses ($t_P = t_{PB} = t_{PT}$) for different bottom and top solid thicknesses ($t_S = t_{SB} = t_{ST}$).

4.1.2 Second Scenario

In this category, bottom and top channels can have different geometrical parameters and their thermohydraulic performance is evaluated. The vertical solid fin thickness of the bottom channel, t_{ST}, is changed from 0.1 to 0.3 mm, while for each t_{ST}, the vertical solid fin thickness of the top channel is also changed from 0.1 to 0.3 mm. For each combination of t_{SB} and t_{ST}, the bottom and top porous substrates, t_{PB} and t_{PT}, are changed from 0.025 to 0.275 mm.

Variation of average heat transfer coefficient of double-layered porous MCHSs is shown in Figure 2-6 versus the bottom solid and the porous substrate thickness for three different t_{ST}. As can be seen, for the double layered MCHSs where t_{SB} and t_{ST} are either 0.1 or 0.2 mm, by increasing the bottom or top porous substrate thickness, heat transfer coefficient increases until a maximum point is reached and then starts to decrease. When t_{SB} or t_{ST} are 0.3 mm adding porous substrate results in a decrease in heat transfer coefficient. Furthermore, thermal performance of the double layered porous MCHS is more sensitive to the solid-porous fin thickness of the bottom microchannel compared to the top one because it is closer to the heat source. As shown in Figure 2-6, at a constant t_{SB}, t_{ST}, and t_{PB}, variations in t_{PB} can result in about 28% change in h_m while at a constant t_{SB}, t_{ST}, and t_{PT}, variations in t_{PT} cause about 8% maximum change in h_m. Similar conclusion can be found when changing the solid fin thickness. At a constant t_{ST}, increasing t_{SB} results in higher rise in the heat transfer coefficient compared to the case when t_{ST} is increased at a constant t_{SB}. Higher sensitivity of heat transfer to the top channel's solid-porous fin thickness occurs when the bottom channel has higher solid-porous fin thickness. Moreover, it is found that at the optimal thermal performance point in double-layered MCHSs the geometrical parameters for the bottom and top channels are different. As shown in Figure 2-6, the highest heat transfer occurs when the bottom channel has a solid-porous fin thickness of about 0.325 mm while the top channel

has a lower solid-porous fin thickness of about 0.275 mm. Therefore, difference between the bottom and top microchannel can be considered in the design of double-layered porous MCHSs for better performance.

The pressure drop variation of the double-layered MCHSs with different bottom and top solid fin thicknesses versus the bottom and top porous substrate thickness is shown in Figure 2-7. By increasing the solid-porous fin thickness, the pressure drop increases linearly at lower fin. Changing t_{SB} or t_{ST} and t_{PB} or t_{PT} has an identical effect on the rise in pressure drop in the bottom and top microchannels. As discussed before, to achieve high thermal performance in the studied double-layered porous MCHSs here, the porous-solid fin thickness of the bottom channel needs to be relatively high which is in the region where there is also considerable pressure drop. However, the porous-fin thickness of the top channel does not need to be as high as the bottom channel, and at the optimal thermal point of the MCHS, the fin thickness of the top channel is smaller than the bottom channel. This can be a benefit compared to single-layered porous MCHSs and a potential area to improve the thermal and hydraulic performance of microchannels.

The variation of FOM for double-layered porous MCHSs with different bottom and top solid fin thicknesses versus the bottom and top porous substrate thickness is shown in Figure 2-8. As can be seen, the double-layered porous MCHSs generally have higher FOM at higher t_{SB}. At a constant t_{ST} and t_{PT}, for $t_{SB} = 0.1$ mm and $t_{SB} = 0.2$ mm, adding porous substrate to the bottom channel increases the FOM until a maximum point is reached. However, for all double-layered porous MCHSs, increasing t_{PT} or t_{ST} results in a reduction of FOM. This is due to lower thermal sensitivity to the top channel fin compared to the hydraulic sensitivity. Therefore, the solid and porous fin thicknesses of the top channel in double-layered porous MCHSs can be designed to achieve lower pressure drops while the keeping the thermal performance at the same level.

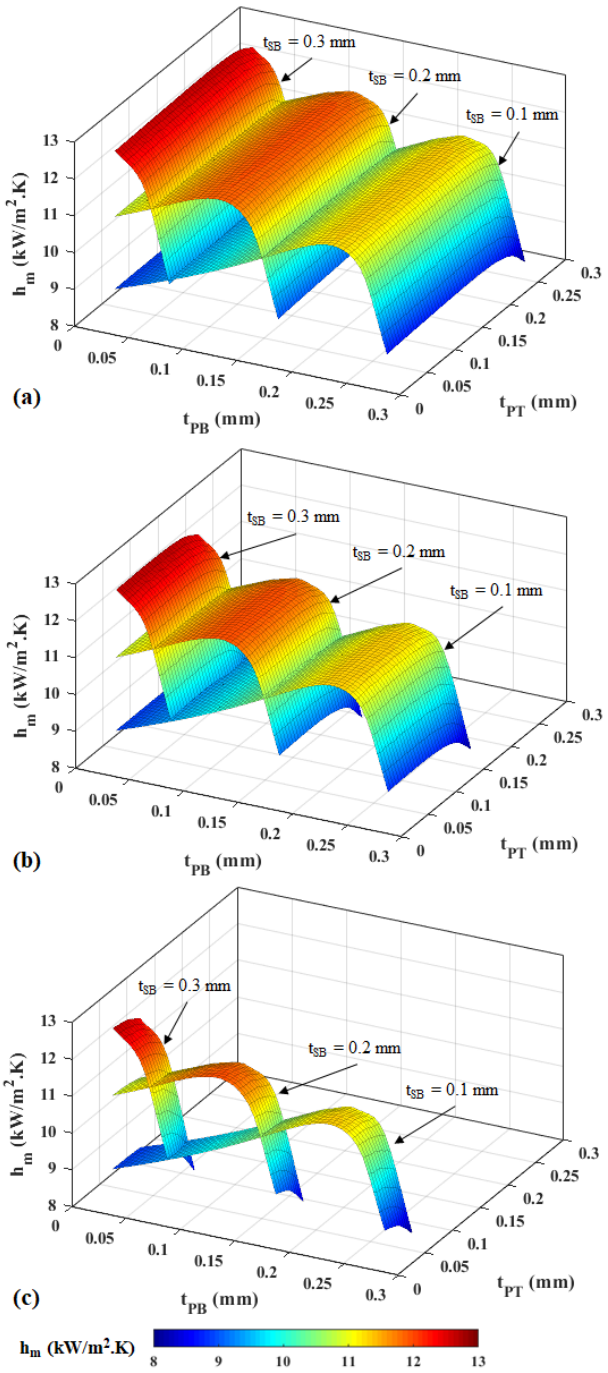

Figure 2-6 Average heat transfer coefficient of double-layered porous MCHSs with different t_{SB} versus bottom and top porous substrate thicknesses for (a) $t_{ST} = 0.1$ mm, (b) $t_{ST} = 0.2$ mm, and (c) $t_{ST} = 0.3$ mm.

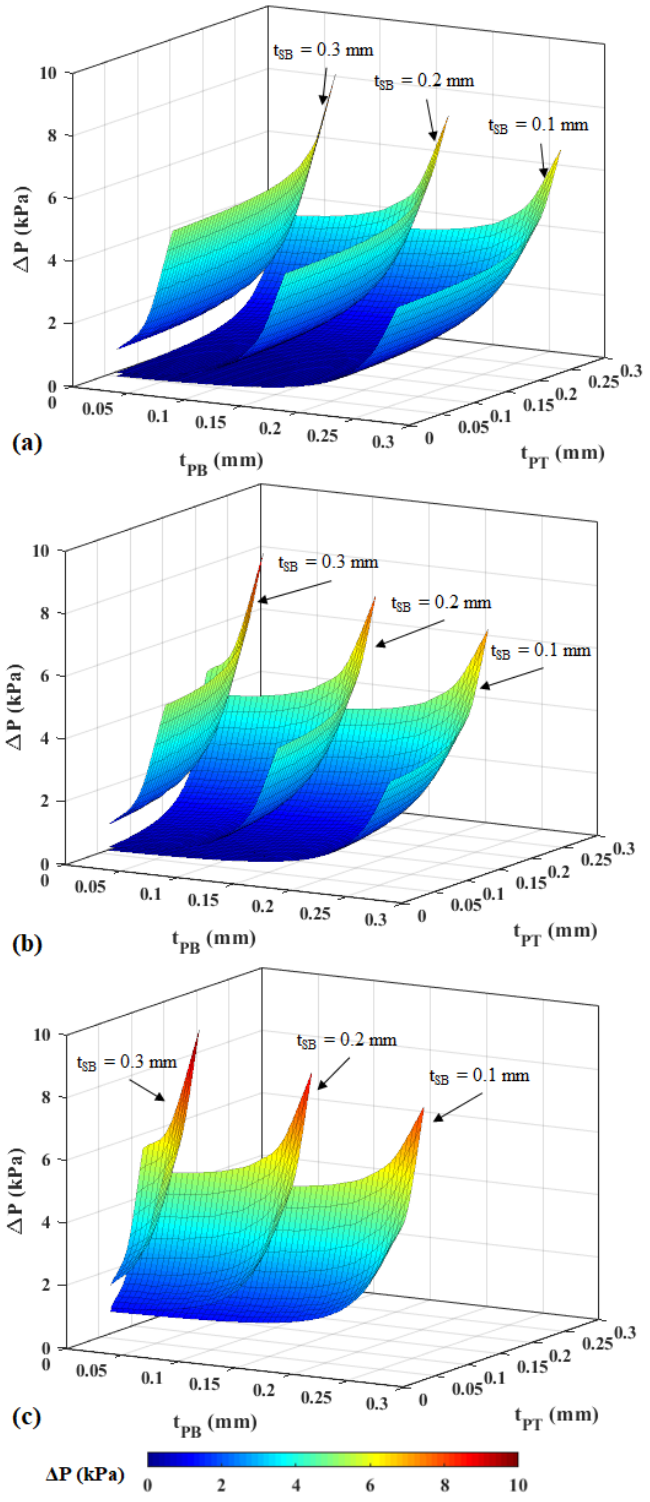

Figure 2-7 Pressure drop of double-layered porous MCHSs with different t_{SB} versus bottom and top porous substrate thicknesses for (a) $t_{ST} = 0.1$ mm, (b) $t_{ST} = 0.2$ mm, and (c) $t_{ST} = 0.3$ mm.

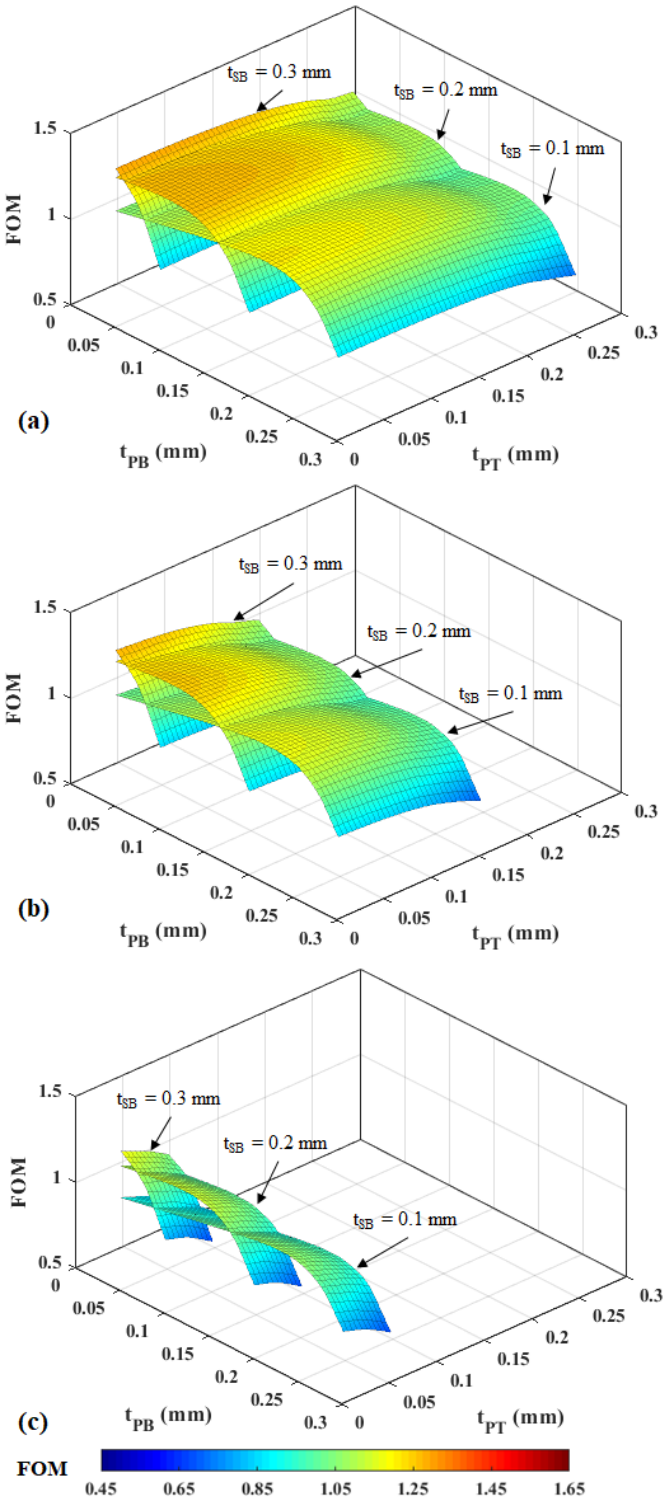

Figure 2-8 Variation of FOM for double-layered porous MCHSs with different t_{SB} versus bottom and top porous substrate thicknesses for (a) $t_{ST} = 0.1$ mm, (b) $t_{ST} = 0.2$ mm, and (c) $t_{ST} = 0.3$ mm.

4.2 Sensitivity Analysis

In this section, a sensitivity analysis is performed on variations of the porous substrate thickness for double layered porous-MCHSs with their solid fin thickness close to candidate conventional MCHSs. For this purpose, similar to the approach used for single layered MCHSs, the heat transfer and pumping power effectiveness of the porous double-layered MCHSs are compared to the basic conventional ones. For a specific double layered porous MCHS, an ε_h and/or ε_P larger than 1, indicates better heat transfer and/or lower pumping power.

Figure 2-9 (a) shows variations of ε_h and ε_P for different double-layered porous MCHSs with bottom and top solid thickness close to $t_S = t_{SB} = t_{ST} = 0.1$. The same porous substrate thickness is assumed for the bottom and top microchannels. The basic conventional double-layered MCHS with $t_{SB} = t_{ST} = 0.1$ mm is represented by the solid line. The double layered MCHSs with ε_h and ε_p higher than 1 have a better thermal and hydraulic performance compared to the basic MCHS. As can be seen, for porous double layered MCHSs with different solid fin thickness, there is a range of bottom and top porous substrate thickness where ε_h and ε_p are larger than 1. The dashed areas represent these regions for each porous MCHS. Also, the optimized range of bottom and top porous substrate thicknesses is shown with $t_{p,opt}$. As discussed in the previous section, higher FOM was achieved at $t_S = t_{SB} = t_{ST} = 0.275$ mm. In Figure 2-9 (b), the variations of ε_h and ε_P for different double-layered porous MCHSs with bottom and top solid thickness close to 0.275 mm are shown. For simplicity, the thickness of the bottom and top channels' porous substrates are kept the same. As the case for $t_S = t_{SB} = t_{ST} = 0.1$ mm, for the porous double-layered MCHSs with bottom and top solid thickness between 0.25 mm to 0.27 mm, there is range of porous substrate thickness that increases the heat transfer coefficient and decreases the pumping power at the same time compared to the conventional MCHS with $t_S = 0.275$ mm. These areas are

shown by the dashed lines and the optimized porous range for each MCHS is shown with $t_{p,opt}$. For both cases, the dashed area becomes larger when the solid thickness gets closer to the basic MCHS thickness. At solid thicknesses close to the basic MCHS, effective conductivity of the fin is less affected. This allows a larger range of porous substrates which can be added to the basic MCHSs to have higher ε_h and ε_p. For each case, the best performing double layered porous MCHS considering both thermal and hydraulic effects, is the one where lines of ε_h and ε_P intersect. Among all the peaks for different solid thicknesses, the highest one falls into the region where the solid thickness is the closes to the basic conventional MCHS. This is because of a higher solid-porous fin effective conductivity and bigger range of porous substrate thickness where ε_h and ε_p can be larger than 1.

Variations of ε_h and ε_P for different bottom and top solid fin thicknesses around $t_S = 0.325$ mm where optimum thermal point occurs, are shown in Figure 2-10. At can be seen, at this solid thickness due to exponential rise in pressure drop with a slight increase in the porous substrate thickness, the ε_p lines are steeper. Moreover, since the solid thicknesses are close to the optimal thermal point, ε_h lines rise to a maximum point and decrease afterwards. For solid thicknesses of 0.3 mm and 0.305 mm, ε_h lines reach their optimum point before hitting the basic MCHS line and ε_h stays smaller than 1. However, for other solid thicknesses which are closer to the basic MCHS fin thickness (0.325 mm), regions with ε_h and ε_p larger than 1 can be achieved by adding porous substrates. This is due to higher porous-solid fin effective conductivity which allows the double layered porous MCHSs to simultaneously have higher heat transfer and lower pressure drop than the basic double-layered MCHS. The optimized areas are shown with the dashed lines.

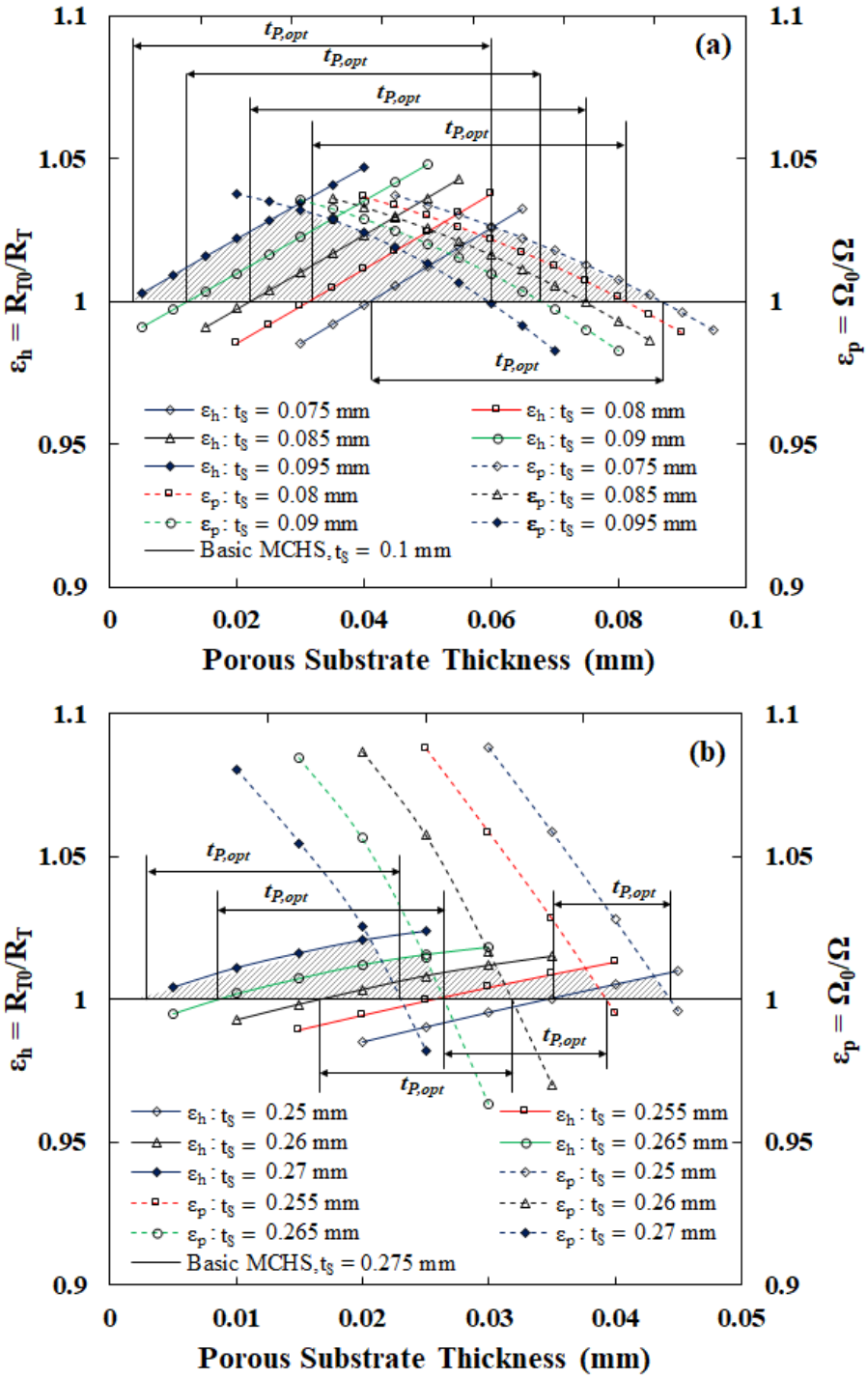

Figure 2-9 Effect of bottom and top porous substrate thickness on primary thermofluid parameters, ε_h and ε_P, for different bottom and top solid fin thicknesses around (a) $t_S = t_{SB} = t_{ST} = 0.1$ mm and (b) $t_S = t_{SB} = t_{ST} = 0.275$ mm. (Dash lines represent ε_P and solid lines represent ε_h)

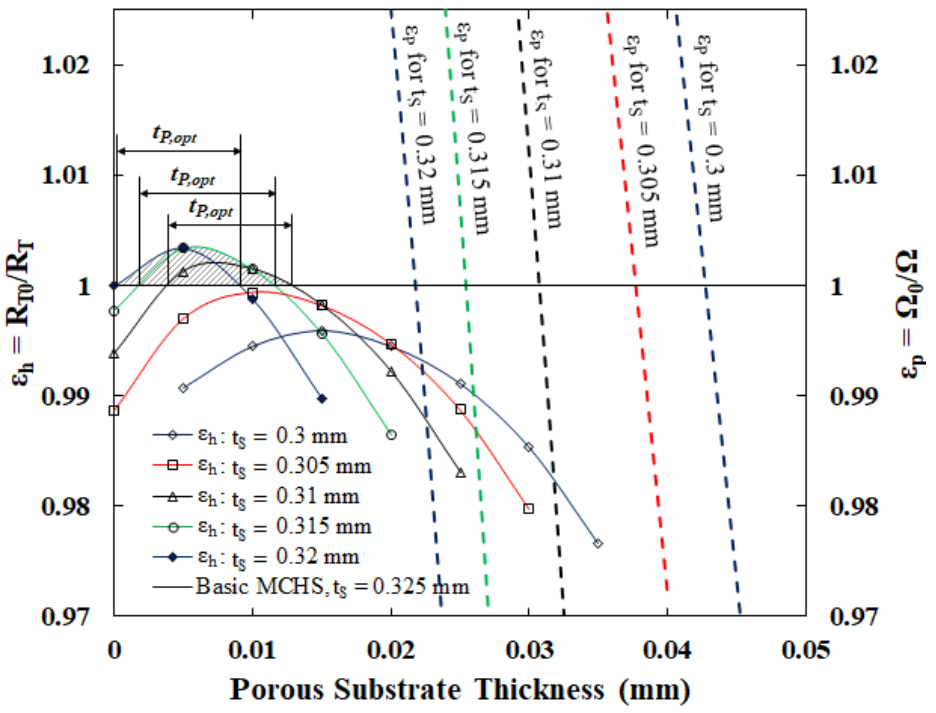

Figure 2-10 Effect of porous substrate thickness on primary thermofluid parameters, ε_h and ε_P, for different bottom and top solid fin thicknesses around $t_S = t_{SB} = t_{ST} = 0.325$ mm. (Dash lines represent ε_P and solid lines represent ε_h)

The concept of optimizing double-layered MCHSs utilizing porous substrates for simultaneous improvement in thermal and hydraulic performances is shown in Figure 2-11. A solid reduction in either top or bottom channel and replacing it with a porous substrate with an optimized higher thickness can increase the solid-porous fin's effective conductivity while imposing lower pumping power. This simultaneous performance improvement occurs at a specific range of porous substrate thickness. The procedure to achieve this optimized region is discussed in this section for some candidate double-layered MCHSs. The same concept can be applied for double-layered MCHSs with any geometrical configuration.

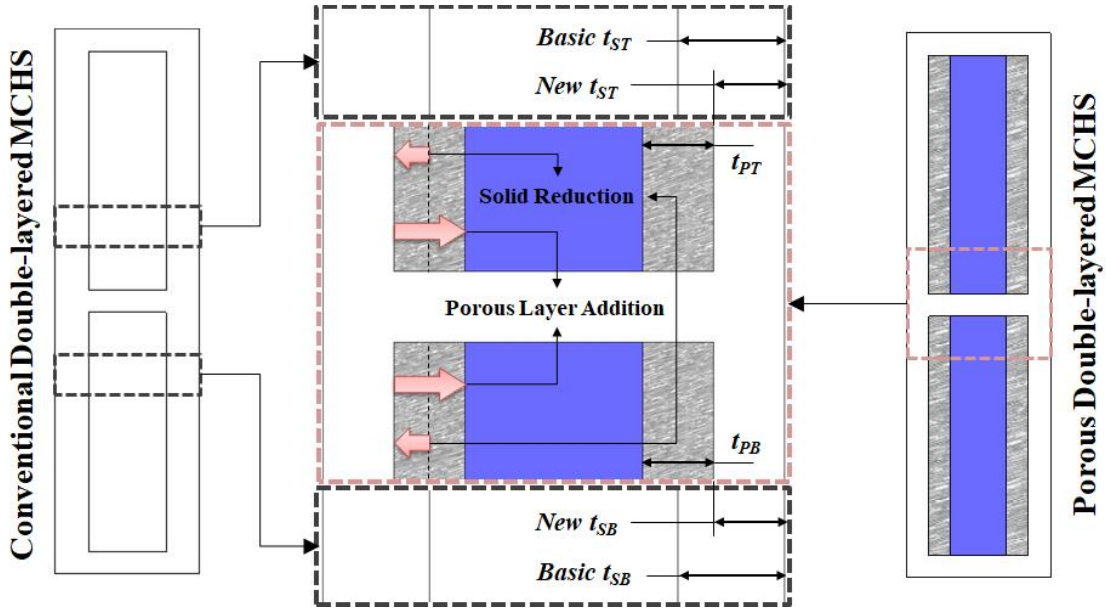

Figure 2-11 Porous substrate setup for double-layered microchannel heat sinks to improve their hydraulic and thermal performance simultaneously.

4.3 Effect of Velocity, Material, and Porosity

In this section, the effects of velocity, heat sink material, and porosity on the performance of the porous double layered MCHSs are discussed. Figure 2-12 shows the effect of coolant velocity on the thermal resistance and Figure of Merit for bottom and top porous substrates thickness of $t_{PB} = t_{PT} = 0.025$ mm. The inlet velocity is change from 0.2 m/s to 2 m/s. Bottom and top channels are assumed to be identical and their solid thickness is changed at constant porous substrate thickness of 0.025 mm where highest FOM and lowest thermal resistance where achieved. At higher inlet velocities, lower thermal resistances can be achieved but more pumping power is required. For all velocities, by increasing the solid thicknesses the thermal resistance reaches to a minimum and then starts to increase. FOM for all velocities increases until a maximum point and starts to decrease afterwards. Furthermore, at higher velocities the optimal heat transfer point occurs at higher bottom and top solid-porous fin thicknesses. Increasing the inlet velocity results in

increase of the coolant flow's heat transfer coefficient and as a result, the thickness of the solid-porous fin can be increased to obtain a higher effective thermal conductivity. Higher flow heat transfer coefficient and higher fin effective conductivity results in higher total heat transfer of the double layered porous MCHS.

Figure 2-13 shows the effect of heat sink material on the performance of double-layered porous microchannel heat sinks. The porous substrates for the bottom and top channels have a thickness of $t_{PB} = t_{PT} = 0.025$ mm. The effect of increasing the bottom and top solid thicknesses on the thermal resistance and FOM are plotted for copper and steel MCHSs. The general thermal and FOM behavior for both materials of the double-layered MCHSs is similar. The thermal resistance of the copper porous MCHSs are lower than that of the steel MCHSs since copper has a higher thermal conductivity. The FOM lines show combined thermal and hydraulic performances of the double-layered MCHSs. At higher solid fin thicknesses, FOM for steel double-layered MCHSs is higher than copper double-layered MCHSs. Since the basic double-layered MCHSs assumed to calculate FOM are also made of copper and steel, it can be concluded that utilizing porous substrates in steel MCHSs is slightly more effective than copper MCHSs. Moreover, the optimal thermal and FOM performances for copper MCHSs occur at slightly lower solid-porous fin thicknesses.

Figure 2-14 shows the effect of porosity on thermal resistance and FOM of double-layered porous MCHSs for different bottom and top solid fin and porous substrate thicknesses. The porous substrate placed on the microchannels has a thickness of 0.025 mm and 0.15 mm. Thermal resistance and FOM are plotted versus bottom and top solid fin thicknesses for porosities of 0.32 and 0.44. The same optimal thermal point behavior is found for both porosities. As can be seen, at porous substrate thicknesses of 0.025 mm and 0.15 mm, the thermal resistance of the double layered

porous MCHSs with porosity of 0.44 is higher than the MCHSs with porosity of 0.32. The change in thermal resistance is more noticeable at higher porous substrate thickness of 0.15 mm. This is due to lower effective thermal conductivity of the solid/porous fin at higher porosity of 0.44. However, this change in thermal resistance is relatively small specially in lower porous substrate thicknesses of 0.025 mm. On the other hand, the pumping power at higher porosity of 0.44 is reduced. To compare the combined changes in thermal resistance and pumping power, FOM for the two porosities are plotted. As can be seen, FOM for a porosity of 0.44 is higher than porosity of 0.32. This indicates that although the heat transfer of the double-layered MCHS is lower at higher porosity, the reduction in pumping power is more effective, and thereby, resulting in a higher FOM.

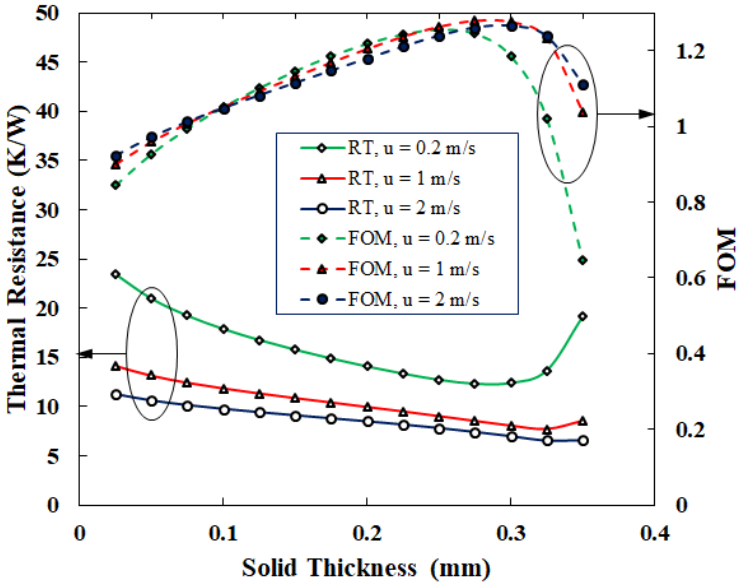

Figure 2-12 Effect of bottom and top solid thickness $t_S = t_{SB} = t_{ST}$ and inlet velocity on the thermal resistance and Figure of Merit for $t_{PB} = t_{PT} = 0.025$ mm. (Dash lines represent FOM and solid lines represent thermal resistance)

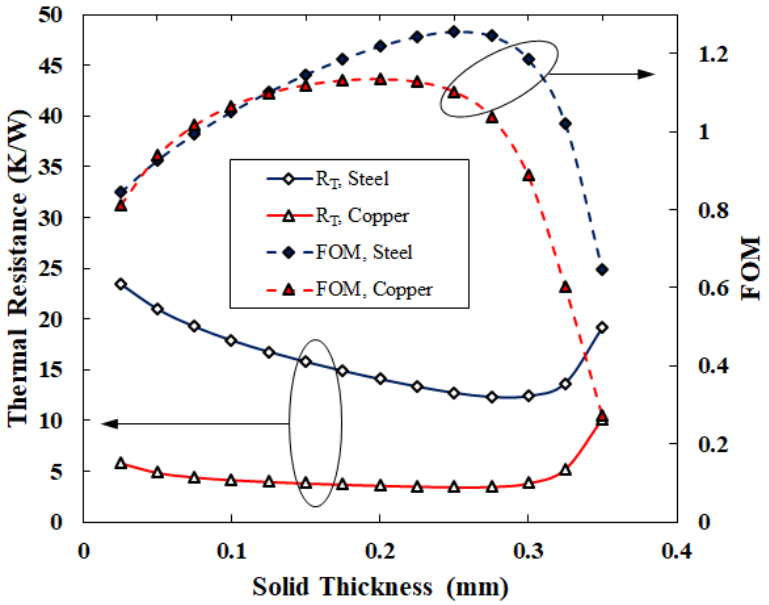

Figure 2-13 Comparison of thermal resistance and Figure of Merit for steel and copper double-layered porous microchannel heat sinks. (Dash lines represent FOM and solid lines represent thermal resistance)

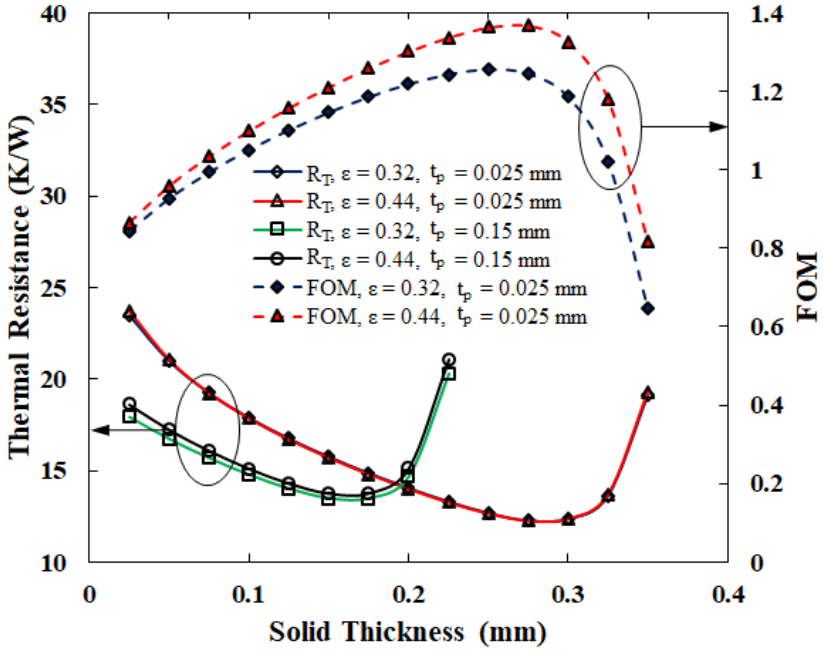

Figure 2-14 Effect of porosity on thermal resistance and Figure of Merit of double-layered porous MCHSs for different bottom and top solid fin and porous substrate thicknesses. (Dash lines represent FOM and solid lines represent thermal resistance)

5. Conclusions

In this chapter, thermal and hydraulic performance of the double-layered porous microchannel heat sinks is comprehensively analyzed through numerical simulations. Effect of utilizing porous substrates is investigated and superior are discussed. The conclusions are as follows:

- Porous substrates can be utilized in double-layered microchannel heat sinks to increase their thermal and hydraulic performance. By a careful design based on an optimization study, thermal resistance and pumping power of double-layered microchannel heat sinks can be reduced simultaneously.
- There is an optimum solid-porous fin thickness for the bottom and top channel that highest heat transfer coefficient can be achieved. Similarly, there is an optimum thickness where FOM is maximum. The optimal FOM point occur at slightly lower solid/porous fin thickness compared to the optimal thermal point.
- Thermal performance of double-layered porous MCHSs is more sensitive to the solid-porous fin thickness of the bottom channel than the top channel. Also, at the optimal thermal point, the solid-porous fin thickness of the bottom channel is higher than the thickness of the top channel. Moreover, since the sensitivity of the thermal resistance to the top solid-porous fin thickness is relatively low, highest FOM of the double-layered porous MCHS occur at high bottom fin thickness and low top fin thickness.
- At higher flow rates, lower thermal resistance and higher pressure drop are observed. The optimal thermal and FOM points for higher flow rates occur at higher porous-solid fin thicknesses.

- Using a higher conductive material for fins decreases the thermal resistance at the same pumping power. Furthermore, at higher thermal conductivity, optimal thermal and FOM point occur at lower solid-porous fin thickness.
- Using a porous substrate with higher porosity results in a rise in thermal resistance and a reduction in pumping power. However, the reduction in pumping power is more significant than rise in thermal resistance. Effect of changing porosity is more noticeable at higher porous substrate thicknesses.

References

[1] A. Adham, N. Mohd-Ghazali and R. Ahmad, "Thermal and hydrodynamic analysis of microchannel heat sinks: A review," Renew sustain Energy Rev, vol. 21, pp. 614-22, 2013.

[2] B. Agostini, M. Fabbri, J. Park, L. Wojtan, J. Thome and B. Michel, "State of the art of high heat flux cooling technologies," Heat Transfer Eng., vol. 28, p. 258–281, 2007.

[3] C. Zhao and T. Lu, "Analysis of microchannel heat sinks for electronics cooling," International Journal of Heat and Mass Transfer, vol. 45, pp. 4857-4869, 2002.

[4] I. Hassan, P. Phutthavong and M. Abdelgawad, "Micro-channel Heat Sinks, An Overview of the State-of-the-Art," Microscale Thermophysical Engineering, vol. 8, pp. 183-205, 2004.

[5] I. Mudawar, "Assessment of high-heat-flux thermal management schemes," Trans. Compon. Packag. Technol. , vol. 24, p. 122–141, 2001.

[6] P. Smakulski and S. Pietrowicz, "A review of the capabilities of high heat flux removal by porous materials, microchannels and spray cooling techniques," Applied Thermal Engineering, vol. 104, pp. 636-646, 2016.

[7] D. B. Tuckerman, "Heat-Transfer Microstructures for Integrated Circuits," Stanford University, 1984.

[8] D. B. Tuckerman and F. R. Pease, "Microcapillary Thermal Interface Technology for VLSI Packaging," Digest of Technical Papers—Symposium on VLSI Technology, pp. 60-61, 1983.

[9] A. Weisberg, H. Bau and J. Zemel, "Analysis of microchannels for integrated cooling," Int. J. Heat Mass Transf, vol. 35, pp. 2465-2474, 1992.

[10] T. Harms, M. Kazmierczak and F. Gerner, "Developing convective heat transfer in deep rectangular microchannels," Int. J. Heat Fluid Flow, vol. 20, pp. 149-157, 1999.

[11] A. Fedorov and R. Viskanta, "Three-dimensional conjugate heat transfer in the microchannel heat sink for electronic packaging," Int. J. Heat Mass Transf., vol. 43, pp. 399-415, 2000.

[12] J. Ryu, D. Choi and S. Kim, "Three-dimensional numerical optimization of a manifold microchannel heat sink," Int. J. Heat Mass Transf., vol. 46, pp. 1553-1562, 2003.

[13] R. Chein and J. Chen, "Numerical study of the inlet/outlet arrangement effect on microchannel heat sink performance," Int. J. Therm. Sci., vol. 48, pp. 1627-1638, 2009.

[14] S. Kim and D. Kim, "Forced convection in microstructures for electronic equipment cooling," J. Heat Transf., vol. 3, pp. 639-645, 1999.

[15] W. Qu and I. Mudawar, "Analysis of three-dimensional heat transfer in micro-channel heat sinks," Int. J. Heat Mass Transf., vol. 45, pp. 3973-3985, 2002.

[16] J. Ryu, D. Choi and S. Kim, "Numerical optimization of the thermal performance of a microchannel heat sink," Int. J. Heat Mass Transf., vol. 45, pp. 2823-2827, 2002.

[17] Z. Y. Guo and Z. Li, "Size Effect on Single-Phase Channel Flow and Heat Transfer at Microscale," International Journal of Heat and Fluid Flow, vol. 24, p. 284–297, 2003.

[18] E. Sparrow, J. Abraham and P. Chevalier, "A DOS-Enhanced Numerical Simulation of Heat Transfer and Fluid Flow Through an Array of Offset Fins With Conjugate Heating in the Bounding Solid," Journal of Heat Transfer, vol. 127, pp. 27-33, 2005.

[19] S. Lu and K. Vafai, "A comparative analysis of innovative microchannel heat sinks for electronic cooling," International Communications in Heat and Mass Transfer, vol. 76, p. 271–284, 2016.

[20] K. Vafai and L. Zhu, "Analysis of two-layered micro-channel heat sink concept in electronic cooling," International Journal of Heat and Mass Transfer, vol. 42, pp. 2287-2297, 1999.

[21] S. Chong, K. Ooi and T. Wong, "Optimisation of single and double layer counter flow microchannel heat sinks," Appl. Therm. Eng., vol. 22, pp. 1569-1585, 2002.

[22] X. Wei, Y. Joshi and M. Patterson, "Experimental and numerical study of a stacked microchannel heat sink for liquid cooling of microelectronic devices," J. Heat Transf., vol. 129, pp. 1432-1444, 2007.

[23] G. Xie, Y. Liu, B. Sunden and W. Zhang, "Computational Study and Optimization of Laminar Heat Transfer and Pressure Loss of Double-Layer Microchannels for Chip Liquid Cooling," J. Thermal Sci. Eng. Appl , vol. 5, no. 1, p. 011004, 2013.

[24] T. Hung, W.-M. Yan and W.-P. Li, "Analysis of heat transfer characteristics of double-layered microchannel heat sink," Int. J. Heat Mass Transf., vol. 55, pp. 3090-3099, 2012.

[25] B. Lu, W. J. Meng and F. Mei, "Experimental investigation of Cu-based, double-layered, microchannel heat exchangers," Journal of Micromechanics and Microengineering, vol. 23, 2013.

[26] J. Wu, J. Zhao and K. Tsenga, "Parametric study on the performance of double-layered microchannels heat sink," Energy Conversion and Management, vol. 80, pp. 550-560, 2014.

[27] C. Leng, X.-D. Wang and T.-H. Wang, "An improved design of double-layered microchannel heat sink with truncated top channels," Applied Thermal Engineering, vol. 79, pp. 54-62, 2015.

[28] C. Leng, X.-D. Wang, T.-H. Wang and W.-M. Yan, "Multi-parameter optimization of flow and heat transfer for a novel double-layered microchannel heat sink," International Journal of Heat and Mass Transfer, vol. 84, pp. 359-369, 2015.

[29] K.Hooman, "Heat and fluid flow in a rectangular microchannel filled with a porous medium," International Journal of Heat and Mass Transfer, vol. 51, pp. 5804-5810, 2008.

[30] T. Hung, Y. Huang and W. Yan, "Thermal performance analysis of porous-microchannel heat sinks with different configuration designs," International Journal of Heat and Mass Transfer, vol. 66, pp. 235-243, 2013.

[31] T. Hung, Y. Huang, T. Sheu and W. Yan, "Numerical Optimization of the Thermal Performance of a Porous-Microchannel Heat Sink," Numerical Heat Transfer, Part A: Applications, vol. 65 , pp. 419-434, 2014.

[32] T. Hung and W. Yan, "Optimization of Design Parameters for a Sandwich-Distribution Porous-Microchannel Heat Sink," Numerical Heat Transfer, Part A: Applications, vol. 66 , pp. 229-251, 2014.

[33] L. Chuan, X.-D. Wang, T.-H. Wang and W.-M. Yan, "Fluid flow and heat transfer in microchannel heat sink based on porous fins," International Communications in Heat and Mass Transfer, vol. 65, p. 52–57, 2015.

[34] H. Shen, X. Liu, H. Yan, G. Xie and B. Sunden, "Enhanced Thermal Performance of Internal Y-Shaped Bifurcation Microchannel Heat Sinks With Metal Foams," ASME. J. Thermal Sci. Eng. Appl., vol. 10, pp. 011001-011001-8, 2017.

[35] B. Shen, H. Yan, B. Sunden, H. Xue and G. Xie, "Forced convection and heat transfer of water-cooled microchannel heat sinks with various structured metal foams," International Journal of Heat and Mass Transfer, vol. 113, pp. 1043-1053, 2017.

[36] B. Wang, Y. Hong, L. Wang, X. Fang, P. Wang and Z. Xu, "Development and numerical investigation of novel gradient-porous heat sinks," Energy Conversion and Management, vol. 106, pp. 1370-1378, 2015.

[37] G. Lu, J. Zhao, L. Lin, X.-D. Wang and W.-M. Yan, "A new scheme for reducing pressure drop and thermal resistance simultaneously in microchannel heat sinks with wavy porous fins," International Journal of Heat and Mass Transfer, vol. 111, pp. 1071-1078, 2017.

[38] S.-L. Wang, X.-Y. Li, X.-D. Wang and G. Lu, "Flow and heat transfer characteristics in double-layered microchannel heat sinks with porous fins," International Communications in Heat and Mass Transfer, vol. 93, pp. 41-47, 2018.

[39] S. Patankar, Numerical Heat Transfer and Fluid Flow, Hemisphere/McGraw-Hill, 1980.

[40] A. Ghahremannezhad and K. Vafai, "Thermal and hydraulic performance enhancement of microchannel heat sinks utilizing porous substrates," International Journal of Heat and Mass Transfer, vol. 122, pp. 1313-1326, 2018.

[41] A. Ghahremannezhad, H. Xu, M. A. Nazari, M. H. Ahmadi and K. Vafai, "Effect of porous substrates on thermohydraulic performance enhancement of double layer microchannel heat sinks," International Journal of Heat and Mass Transfer, vol. 131, pp. 52-63, 2019.

Chapter 3: Thermal Enhancement of PCM-based Energy Systems Using Gradient Porous Metal Foams

Nomenclature

A_m	Constant parameter (m^2)
a_{fs}	Interfacial area density (m^{-1})
C	Inertial coefficient (m^{-1})
C_p	Specific heat capacity (J kg^{-1} K^{-1})
d_f	Fiber diameter (m)
d_p	Pore diameter (m)
E	Energy storage quantity (J)
g	Gravitational acceleration (m s^{-2})
h_{fs}	Interfacial heat transfer coefficient (W m^{-2} K^{-1})
K	Permeability (m^2)
k_e	Effective thermal conductivity (W m^{-1} K^{-1})
k_{td}	Thermal dispersion conductivity (W m^{-1} K^{-1})
L	Latent heat (J kg^{-1})
L_x	Width of the energy system (m)
L_y	Height of the energy system (m)
m	Mass (Kg)
Nu	Nusselt number
P	Power input (W)
PPI	Pore density

Pr	Prantdl number
Ra	Reighley number
p	Pressure (Pa)
S	Source term
T	Temperature (K)
T_0	Initial temperature (K)
T_{m1}	Solidus temperature (K)
T_{m2}	Liquidus temperature (K)
t	time (s)
u	Velocity in x direction (m s^{-1})
v	Velocity in y direction (m s^{-1})
x	x coordinate (m)
y	y coordinate (m)

Greek

α	Thermal diffusivity (m^2 s^{-1})
β	Liquid fraction within the pore space
γ	Thermal expansion coefficient (K^{-1})
δ	Liquid fraction
ε	Porosity
ε_x	Gradient porosity changing in x direction
ε_y	Gradient porosity changing in y direction
μ	Dynamic viscosity (kg m^{-1} s^{-1})

ν	Kinematic viscosity ($m^2\ s^{-1}$)
ρ	Density ($kg\ m^{-3}$)
ω	Constant parameter

Subscripts

eff	Effective value
f	Phase change material
s	Metallic foam
x	x direction
y	y direction

1. Introduction

Latent heat thermal energy storage systems have recently gained a great amount of attractions due to their high energy density, storage capacity, and ability to work at constant temperatures. These systems are widely used in many applications to reserve energy and release it when required [1–4]. For this purpose, phase change materials can be used in energy storage systems as a renewable energy resource for storage and retrieval. Melting evolution of paraffin as a phase change material inside an enclosure heated from the left wall is shown in Figure 3-1. To improve the performance of the energy storage systems, it is important to study their melting behavior and heat transfer characteristics [5–15].

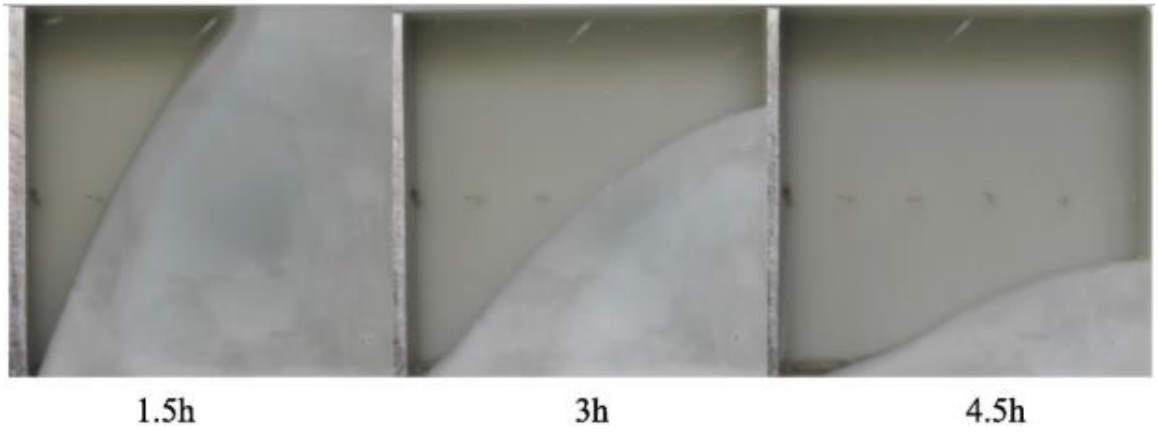

Figure 3-1 Melting evolution of paraffin in an enclosure heated from left in experimental work of Zheng et al. [42] (adapted with copyright permission).

In early stages, the melting behavior of PCMs has been investigated by designing experiments and numerical analysis [16–18]. Wang et al. [19] performed various experiments to study melting process on a heated vertical wall in a rectangular enclosure. Desai and Vafai [20] used a finite element formulation to investigate melting process in a rectangular cavity. Voller and Prakash [21] developed a fixed grid methodology to perform numerical simulations for phase-change in the mushy region.

To improve self-insulating behavior of PCM-based energy storage systems and increase their conductivity, porous metal foams are used as thermal conductivity enhancers [22–24]. These metal foams have high thermal conductivity, high porosity, and large surface area per unit volume which makes them perfect candidate for performance enhancement of various thermal systems [6,25–27]. The potential performance improvement due to utilizing porous metal foams in energy systems that work with PCMs has been discussed in many works. Tong et al. [28] used a high porosity metal matrix inside PCMs to increase their heat transfer rate. Py [29] presented a combination of paraffin PCM impregnated in a compressed expansed natural graphite. Lafdi et al.

[30] experimentally investigated the phase change heat transfer in PCMs within aluminium metal foams. Their results indicated that higher porosity and bigger pore size foams reached the steady-state temperatures faster than the other configurations. Karaipekli et al. [31] and Jiao et al. [32] performed series of experiments and indicated the enhanced conductivity of stearic acid PCMs embedded in expanded graphite, perlite, and carbon fibers as the TCEs. Zhao et al. [33] worked on melting and solidification processes for PCMs embedded in metal foams considering the effect of natural convection. The results showed faster phase change process in PCM/foam combination and increase in overall heat transfer rate by 3 to 10 times. Tian and Zhao [34] numerically investigated the heat transfer enhancement by using metal foams in PCMs. Their results showed that although the natural convection is suppressed when using a metal foam, the overall heat transfer was improved because of the increased thermal conductivity inside the PCM. Oya et al. [35] showed higher effective thermal conductivity using porous nickel as a TCE in erythriotl PCMs. Li et al [36] performed numerical and experimental studies to investigate the melting phase change heat transfer in paraffin-metallic foam composites. The effect of porosity and pore density on the wall temperature were studied and evolution of the solid-liquid interface location were predicted. Liu et al. [37] established a numerical model using enthalpy porosity theory to predict the melting process of PCMs in a shell-and-tube type latent heat thermal energy storage. Xiao et al. [38, 39] carried out several experiments to study the thermal behavior of paraffin/nickel and paraffin/copper foam composite phase change materials. Xu et al. [40] studied the melting performance of phase materials within porous media in a horizontal concentric-tube thermal storage unit and discussed about the porosity parameters, location, and height ratio of the porous inserts. Mahdi and Nsofor [41] used a combination of porous metal foams and nanoparticles to improve the melting of phase change materials in a triplex-tube heat exchanger. Zheng et al. [42] performed series of experiments on the melting process of copper foam/paraffin PCMs and studied the effect of heating position on

the thermal performance. They also established a numerical model and indicated that the copper foam/paraffin shortens the melting time by 20% compared to pure PCMs. Melting evolution of the PCM in the copper foam in experiments of Zheng et al. [42] is shown in Figure 3-2.

Some researchers have studied the melting process of PCMs in metal foams at pore-scale. Chen et al. [43] performed experimental studies to investigate the pore-scale melting behavior of paraffin wax PCMs embedded in aluminum foams. They also used a lattice Boltzman model to simulate the phase change process. Sundarram and Li [44] numerically investigated the pore size and porosity of PCM/microcellular metal foams. Feng et al. [45] used a pore-scale and a volume-averaged method to model melting of PCM in finned metal foams and reported a reasonable agreement between prediction results of the two approaches.

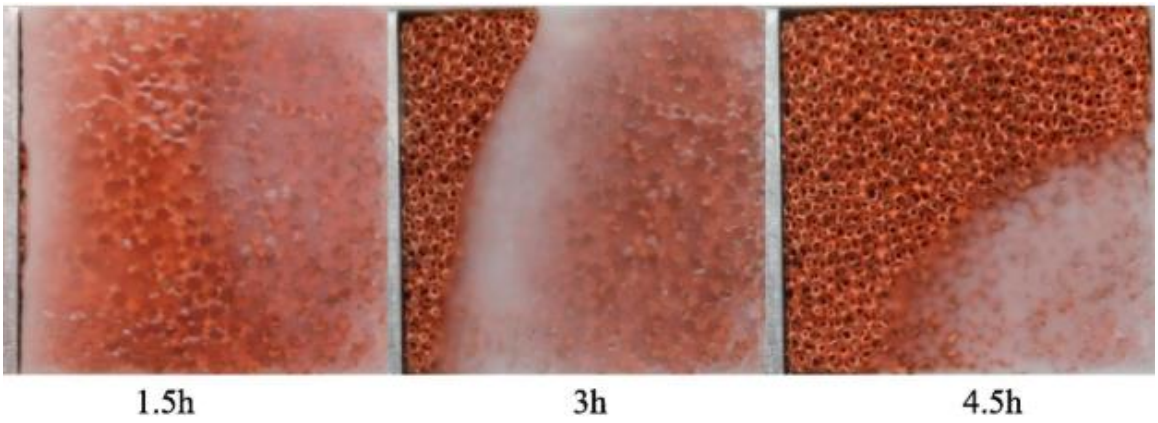

Figure 3-2 Melting evolution of PCM inside an enclosure filled with copper foam in experiments of Zheng et al. [42] (adapted with copyright permission.)

A number of works have focused on the characteristics of the metal foam and used non-uniform structures to investigate the possible effects on melting behavior of PCMs. Yang et al. [46] proposed a linearly changed porosity of copper foam inside a sodium nitrate PCM to improve the thermal storage performance. The results showed that the linearly changed porosity decreases the melting time compared to the constant porosity foams. Tao et al. [47] investigated the heat storage

performance of foam/paraffin composites for various PPI and porosities. A foam scheme with non-uniform porosity was proposed which can improve the heat transfer. Yang et al. [48] experimentally investigated the solidification of distilled water saturated in metallic foams with graded structures. Results showed that when porous layers with different porosities are stacked up, solidification time is effectively reduced. Zhu et al. [49] proposed a structure of finned metal foam with graded porosity which can further accelerate the melting process and enhance the heat transfer. Zhang and He [50] performed numerical investigations using stacked up porous metal foams with different porosities, and also foams with linearly changing porosity inside PCMs. Their results showed enhanced heat transfer process when using metal foams with a porosity gradient. Kumar and Saha [51] used variable porosity metal foams in shell and tube latent heat thermal energy storage and numerically studied the geometrical parameters affecting the temperature distribution.

To come up with effective designs for energy storage systems, more in depth investigation is required specially on the structure of the porous foams which play an important role as thermal conductivity enhancers. In this chapter, we perform a comprehensive study on metal foams with graded structures and their effect on the performance of the energy storage systems. We discuss various foam structures with positive and negative change rate at different spatial directions of the enclosure. Different foam characteristics such as porosity parameters, pores per inch (PPI), and size of the system are taken into account and the melting rate and energy storage density are investigated.

2. Physical and numerical model description

2.1 Physical model

Schematic of the energy storage system is shown in Figure 3-3. The rectangular enclosure has dimensions of $L_x \times L_y = 100 \times 100$ mm^2. The metallic foam is assumed to be made of copper, and paraffin is employed as the phase change material. Based on the position of the heat source and direction of the gradient porosity, fifteen different cases are considered and compared. The heat source with a constant hot temperature is placed either at left, bottom, or top of the system while other walls are insulated. For each heat source position, five porous foam configurations are studied. Uniform porosity foam (UPF), positive gradient porosity foam in x direction (PGPFX), negative gradient porosity foam in x direction (NGPFX), positive gradient porosity foam in y direction (PGPFY), and negative gradient porosity foam in y direction (NGPFY), which are shown in Figure 3-3 (a), (b), (c), (d), and (e) respectively.

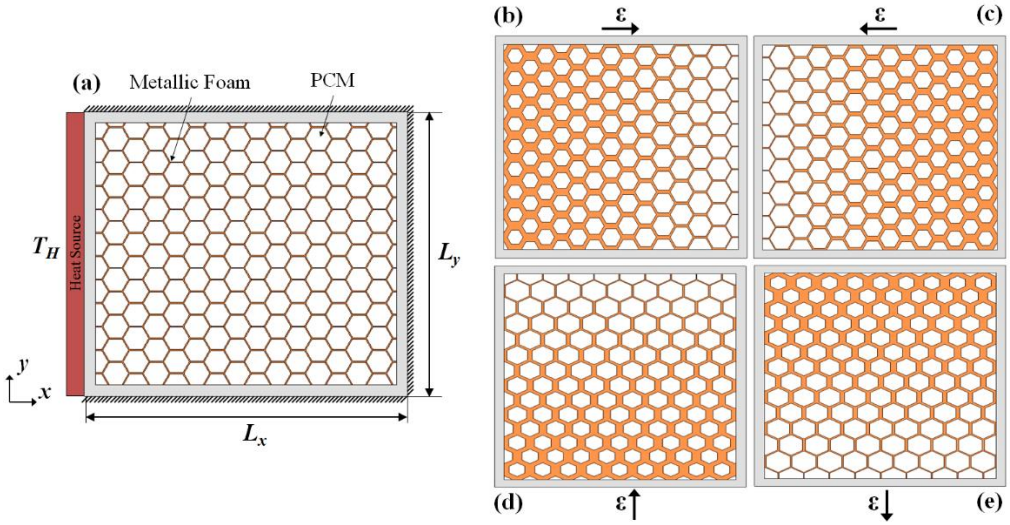

Figure 3-3 Geometry of the energy storage system. (a) Uniform porosity foam (UPF); (b) positive gradient porosity foam in x direction (PGPFX); (c) negative gradient porosity foam in x direction (NGPFX); (d) positive gradient porosity foam in y direction (PGPFY); (e) negative gradient porosity foam in y direction (NGPFY).

2.2 Mathematical formulation

To evaluate the heat transfer performance and study the transient phase change process of the two-dimensional porous configurations, a numerical model is used considering the effects of natural convection and heat conduction. The following assumptions are made to establish the numerical model:

(a) The flow of the liquid phase of PCM is assumed to be incompressible and laminar.

(b) The thermal properties of PCM and foam are constant and isotropic.

(c) The viscosity of the liquid PCM is assumed to remain constant.

Boussinesq approximation is used to represent the natural convection and a non-local thermal equilibrium (NLTE) model is employed to account for the transient heat exchange between the PCM and the foam caused by their temperature difference. The governing equations based on volumetric averaging method using Darcy-Brinkman-Forchheimer model for PCM-based heat sink are as follows [52–54]:

Continuity:

$$\frac{\partial \rho_f}{\partial t} + \frac{\partial (\rho_f u)}{\partial x} + \frac{\partial (\rho_f \mathrm{v})}{\partial y} = 0 \qquad (3\text{-}1)$$

Momentum:

$$\frac{\rho_f}{\delta}\frac{\partial u}{\partial t} + \frac{\rho_f}{\delta^2}\left(u\frac{\partial u}{\partial x} + \mathrm{v}\frac{\partial u}{\partial y}\right) = \frac{\mu_f}{\delta}\left(\frac{\partial^2 u}{\partial x^2} + \frac{\partial^2 \mathrm{v}}{\partial y^2}\right) - \frac{\partial p}{\partial x} + S_x \qquad (3\text{-}2)$$

$$\frac{\rho_f}{\delta}\frac{\partial \mathrm{v}}{\partial t} + \frac{\rho_f}{\delta^2}\left(u\frac{\partial \mathrm{v}}{\partial x} + \mathrm{v}\frac{\partial \mathrm{v}}{\partial y}\right) = \frac{\mu_f}{\delta}\left(\frac{\partial^2 u}{\partial x^2} + \frac{\partial^2 \mathrm{v}}{\partial y^2}\right) - \frac{\partial p}{\partial x} + S_y \qquad (3\text{-}3)$$

where ρ_f is the density, μ_f is the dynamic viscosity, u the velocity in x direction, v the velocity in y direction, p the pressure, and δ is the liquid fraction. S_x and S_y are momentum source terms which can be written as:

$$S_x = -\frac{A_m(1-\beta)^2}{\beta^3+\omega}u - \frac{\mu_f}{K}u - \frac{\rho_f C_F}{\sqrt{K}}|\vec{V}|u \quad (3\text{-}4)$$

$$S_y = -\frac{A_m(1-\beta)^2}{\beta^3+\omega}\mathrm{v} - \frac{\mu_f}{K}\mathrm{v} - \frac{\rho_f C_F}{\sqrt{K}}|\vec{V}|\mathrm{v} + \gamma\rho_f g(T_f - T_0) \quad (3\text{-}5)$$

The first term in equations (3-4) and (3-5) are due to the mushy zone where PCM undergoes a phase change process. A_m is the mushy zone constant and is set to 10^5 [55]. ω is a constant term which is set to be 0.001 [55]. β is the liquid fraction of the phase change material within the pore space which can be defined as:

$$\begin{aligned} &\beta = 0 && \text{if } T_f < T_{m1} \\ &\beta = 1 && \text{if } T_f > T_{m2} \\ &\beta = \frac{T_f - T_{m1}}{T_{m2} - T_{m1}} && \text{if } T_{m1} < T < T_{m2} \end{aligned} \quad (3\text{-}6)$$

$$\delta = \varepsilon\beta \quad (3\text{-}7)$$

K is permeability and C_F is Forchheimer constant which are determined based on following equations [56]:

$$K = 0.00073(1-\varepsilon)^{-0.224}\left(\frac{d_f}{d_p}\right)^{-1.11} d_p^2 \quad (3\text{-}8)$$

$$\frac{d_f}{d_p} = 1.18\sqrt{\frac{1-\varepsilon}{3\pi}} \quad (3\text{-}9)$$

where d_p is pore diameter and d_f is the fiber ligament diameter. The last term in equation (3-5) is the Boussinesq approximation for natural convection. γ is thermal expansion coefficient.

Energy equation for metal foam:

$$(1-\varepsilon)\rho_s C_{ps}\frac{\partial T_s}{\partial t} = k_{se}\left(\frac{\partial^2 T_s}{\partial x^2} + \frac{\partial^2 T_s}{\partial y^2}\right) + h_{fs}a_{fs}(T_f - T_s) \quad (3\text{-}10)$$

Energy equation for the phase change material:

$$\varepsilon\rho_f C_{pf}\frac{\partial T_f}{\partial t}+\varepsilon\rho_f C_{pf}\left(u\frac{\partial T_f}{\partial x}+\mathrm{v}\frac{\partial T_f}{\partial y}\right) = \left(k_{fe}+k_{td}\right)\left(\frac{\partial^2 T_f}{\partial x^2}+\frac{\partial^2 T_f}{\partial y^2}\right)+h_{fs}a_{fs}\left(T_s-T_f\right)-\varepsilon\rho_f L\frac{\partial\beta}{\partial t} \quad (3\text{-}11)$$

where ρ_f and ρ_s are densities of PCM and metal foam respectively; C_{pf} and C_{ps} are specific heat capacities of PCM and metal foam respectively; L is the latent heat of PCM; T_f and T_s are the temperatures of the PCM and metal foam; L is the latent heat; k_{se} and k_{fe} are the effective thermal conductivities of the metal foam and the PCM, which are calculated based on the method proposed by Mesalhy et al. [57]. k_{td} is the thermal dispersion conductivity which can be neglected since the effect of thermal dispersion is not considerable compared to the effect of high thermal conductivity of the metal foam. a_{sf} and h_{sf} are the interfacial area density and interfacial heat transfer coefficient, which are determined by the method developed by Calmidi [58] and Churchill and Chu [59] to account for heat transfer between foam and PCM due to natural convection.

$$h_{sf}=\frac{k_{sf}Nu}{d_f}=\frac{k_f}{d_f}\left(0.36+\frac{0.518\,Ra_d^{\frac{1}{4}}}{\left(1+\left(\frac{0.559}{Pr}\right)^{\frac{9}{16}}\right)^{\frac{4}{9}}}\right) \quad (3\text{-}12)$$

where $Ra_d=\frac{g\gamma\Delta T d_f^3}{\alpha_f\nu_f}$. α_f and ν_f are the thermal diffusivity and kinematic viscosity of the PCM. The gradient porous structure is shown in Figure 3-3 and defined as:

$$\begin{array}{ll}\varepsilon=\varepsilon_0+mx & \text{in } x \text{ direction}\\ \varepsilon=\varepsilon_0+my & \text{in } y \text{ direction}\end{array} \quad (3\text{-}13)$$

where ε_0 is porosity of the porous medium at left or bottom wall where $x=0$ mm or $y=0$ mm, and m is a constant. All parameters and properties which are dependent on the porosity of the TCE

are changed accordingly. Thermophysical properties of the PCM and metal foam are summarized in Table 3-1 [42].

Table 3-1 Properties of the PCM and metal foam

Material	ρ (kg m^{-3})	C_p (J kg^{-1} K^{-1})	k (W m^{-1} K^{-1})	μ (Pa s)	L (kJ/kg)	T_m	γ
PCM (Paraffin)	900	2300	0.3	0.00324	148.8	323-331	0.0005
Copper foam	8900	386	380	-	-	-	

2.3 Initial and boundary conditions

Schematic of the computational domain and boundary conditions are shown in Figure 3-3 (a). Initially, the whole domain including the PCM and the metal foam are at a temperature of 287 K. A heat source with constant temperature higher than the melting temperature of the PCM is placed at either left, bottom, or top wall. For each heat source case, all other walls are kept insulated from outside. The boundary conditions can be written as:

Initial condition

$$T_s = T_f = T_0 = 287\ \text{K} \qquad @\ t = 0 \qquad 0 \le x \le 100, \qquad 0 \le y \le 100 \tag{3-14}$$

Boundary conditions

$$\begin{aligned}
&\text{Heat source at left:} && T = T_H, \quad x = 0, && 0 \le y \le 100, && \text{other walls:} && \frac{\partial T}{\partial n} = 0 \\
&\text{Heat source at bottom:} && T = T_H, \quad y = 0, && 0 \le x \le 100, && \text{other walls:} && \frac{\partial T}{\partial n} = 0 \\
&\text{Heat source at top:} && T = T_H, \quad y = 100, && 0 \le x \le 100, && \text{other walls:} && \frac{\partial T}{\partial n} = 0 \\
&\text{For all walls:} && u = \text{v} = 0
\end{aligned} \tag{3-15}$$

T_H is the hot temperature of the heat sources and is set to be 340 K. n is the normal direction against the boundary wall which is x for left and right walls and y for bottom and top walls. For the cases which are uniform or have a gradient structure in y direction, and are heated from the bottom or top wall, only half of the enclosure is simulated with a symmetry boundary condition.

2.4 Numerical procedure

The unsteady melting phase change process of the PCM inside the metal foam is simulated using a finite volume approach with ANSYS FLUENT 18. PISO scheme is used for pressure-velocity coupling and PRESTO! method is adopted for spatial discretization of the pressure equations. Convergence criterion for completion of the solution is set to be 10^{-6}. Three mesh sizes of 10000, 22500, and 40000 are used to ensure the results are independent of the number of computational cells. As shown in Table 3-2, the results for temperature at a specific point inside the enclosure for the three mesh sizes are very close with an average difference of 0.5%. Therefore, the 22500 mesh distribution is used. For enclosures with bigger size, higher number of the computational cells was considered. Time steps of 0.1 s, 0.25 s, and 0.5 s were used to test the time independency as shown in Figure 3-4. A time step of 0.25 s can be used to ensure accuracy and performing simulations within a reasonable computational time. The adopted numerical model is validated with the experimental results of Zhao et al. [33]. The same domain size, material properties, and boundary conditions are used, and temperatures are recorded at identical thermocouple locations. Figure 3-5 shows the comparison of current numerical results and experimental results of Zhao et al. [33]. As can be seen, current numerical results match well with the experiments and as a result, the numerical setup is very reliable for the objective of this work.

Table 3-2 Grid independence results

Grid	$T_{t=4000\ s}$	$T_{t=8000\ s}$	$T_{t=12000\ s}$	$T_{t=18000\ s}$
10000	38.820	48.027	51.991	55.898
22500	39.018	48.707	52.606	56.274
40000	39.018	48.707	52.606	56.273

Complete melting time, energy density, and energy storage rate are used to evaluate the performance of the porous TCEs. The energy storage quantity is obtained by [49]:

$$E(t) = E_{PCM}(t) + E_{foam}(t) = \delta m_{PCM} L + m_{PCM} C_{pf}(T - T_0) + m_{foam} C_{ps}(T - T_0) \quad (3\text{-}16)$$

The energy density is defined as the energy storage quantity per unit mass at the complete melting time. The energy storage rate is calculated by dividing the obtained energy density by the complete melting time.

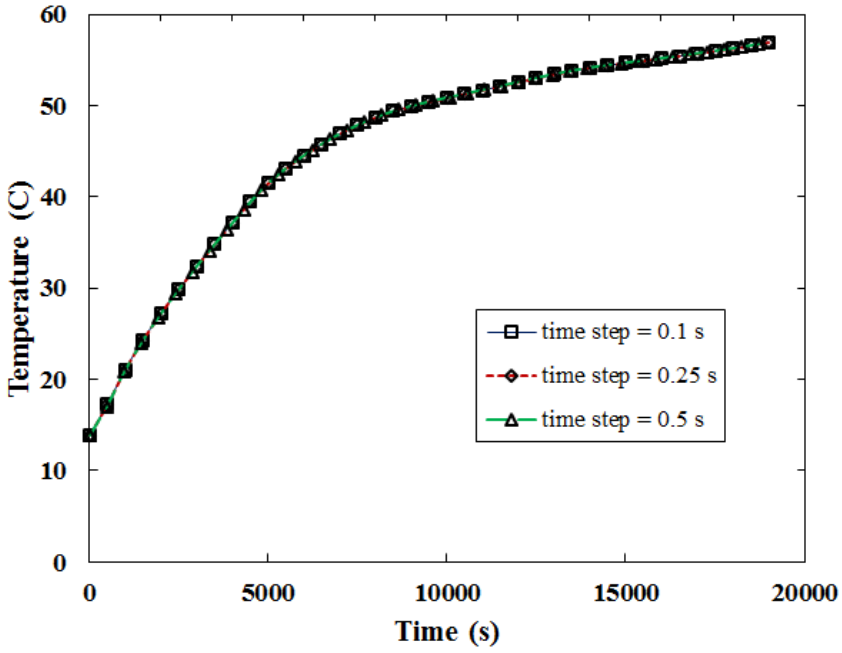

Figure 3-4 Time step independence study

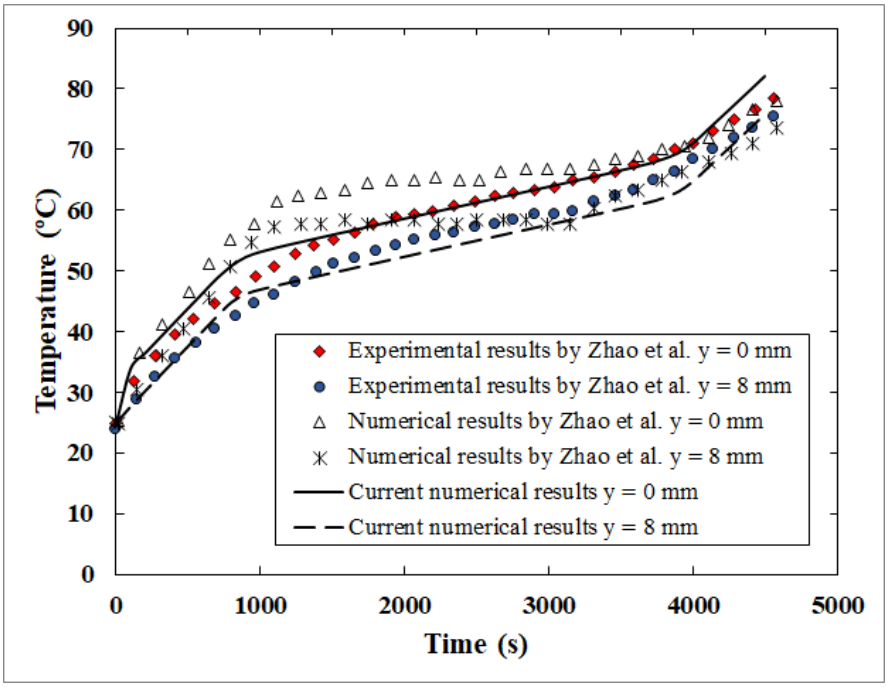

Figure 3-5 Comparison of current numerical results with the experimental and numerical results of Zhao et al. [33]

3. Results and discussion

3.1. Effects of gradient porous TCE on melting process of PCM

In this section melting process of the paraffin as the phase change material is discussed in presence of gradient porous metal foams. For all cases, the porous metal foams have an average porosity of 0.845 and PPI of 5. The porosity of the gradient porous foams linearly changes from 0.70 to 0.99 in various directions with porosity change rate of $m = 2.9$. Figure 3-6 shows the phase change process of the uniform and gradient porosity TCEs when heated from left, bottom, and top side. The heater temperature at the heat source is $T_H = 340$ K. The red parts inside the enclosure represent the liquid PCM and the blue parts represent the solid PCM. For all cases, melting of the PCM embedded inside the porous matrix starts at the heat source and continues until all the PCM

is completely turned into liquid. Natural convection and thermal conduction are the two main heat transfer mechanisms which cause the phase change of the PCM inside the enclosure. Heat is conducted mainly through the porous metal foam and partly through the liquid/solid PCM. Natural convection is formed because of the resulting liquid circulations inside the unit. The presence of the porous matrix increases the effective thermal conductivity but at the same time, increases the resistance to the natural convection. Therefore, the porous characteristics of the metal foam can significantly influence the heat transfer process inside the energy storage unit. Different porous metal foam structures under various heating locations are shown in Figure 3-6 to study the resulting effects on the PCM's phase change process. Despite the described general melting behavior that applies to all cases, each case can have its unique behavior which is discussed further in this section.

When the heat source is placed at the left wall, as shown in Figure 3-6 (a), the main direction of the heat flux is from left to right and perpendicular to the downward direction of the gravity. The melting evolution is depicted for five different porous structures, namely, UPF, PGPFX, NGPFX, PGPFY, and NGPFY. It can be seen in Figure 3-6 (a) that as the PCM melts and turns into the liquid phase, it starts to move upward at the left heat source, and as a result, a circulation is formed at the left side of the enclosure which represents the natural convection. The resulting circulations get bigger with time and help for a faster melting of the PCM. For all five porous structures, the effect of the natural convection is stronger at the left and top parts of the enclosure, and as a result, the PCM melts faster and moves further at the top part compared to the bottom part. This causes the overall melting front to tilt during the phase change process with the slope increasing gradually due to the growing natural convection. As can be seen in Figure 3-6 (a), when the heat source is placed at the left wall, the PGPFY case has the fastest melting among the five cases with its PCM being completely melted at $t = 4575$ s. This happens as a result of strength of the natural convection and the distribution of conductivity which will be discussed here for each

case. The porosity gradient direction for the PGPFX and NGPFX cases is parallel to the main direction of the heat transfer which is left to right. PGPFX has the lowest porosity at the left wall, and therefore, provides the highest thermal conduction and the most resistance to natural convection at the vicinity of the heat source. Consequently, compared to other four porous structures, melting front proceeds further inside the enclosure for PGPFX at the bottom and top parts in the beginning of the phase change process when the liquid circulations are smaller. Gradually, more amount of PCM turns into liquid and bigger circulations are formed which shows its effects more at the top part of the enclosure. For PGPFX, the melting rate becomes relatively slower at the final stages of phase change process because of higher suppression of natural convection and also lower thermal conductivity at the bottom right section of the enclosure where there are still final portions of solid PCM to be melted. The NGPFX structure has an exactly opposite porosity gradient with lowest porosity at the left, and therefore, lowest conduction and also lowest resistance to natural convection at the heat source. As a result, the melting behavior of the NGPFX structure at the vicinity of the heat source is closest to a pure PCM case in which low conductivity prevents heat penetration towards the bulk PCM and natural convection is the main melting mechanism. It is shown in Figure 3-6 (a) that the PCM in NGPFX case melts considerably faster at the top part of the enclosure and low conductivity at the heat source results in a slower melting at the bottom part. As a result, the NGPFX has the slowest overall melting time although it imposes the least resistance to natural convection. This shows the importance of providing higher thermal conduction at the vicinity of the heat source for faster melting of PCM in energy storage units. The porosity gradient direction for the PGPFY and NGPFY structures is perpendicular to the main heat transfer direction. The porosity for PGPFY case starts from a lower value at the bottom part and linearly increases in upward direction providing more space for PCM circulations at the top part. Therefore, for PGPFY, heat conduction and resistance to natural convection is highest at

the bottom and lowest at the top. This configuration allows a relatively better natural convection at the top part while providing high thermal conductivity at the whole bottom part of the enclosure. Therefore, the two main heat transfer mechanisms are both effectively present at the heat source. The advantage of lower suppression of circulations at the top and higher conductivity at the bottom shows itself at final stages of melting especially at the bottom right section of the unit where other porous structures have slower melting rate. The NGPFY case has an opposite porosity gradient direction to PGPFY and provides highest conduction and resistance to convection at the top and lowest at the bottom part. This configuration worsens the difficulty in melting of PCM at the bottom part of the enclosure due to lack of thermal conductivity at this section which eventually results in a higher complete melting time.

Figure 3-6 (b) shows the phase change process for the five considered porous structures when the heat source is placed at the bottom wall. In this case, the main direction of heat transfer is parallel but opposite to the direction of gravity and there is no favored part for natural convection unlike the case in which the heat source is placed at the left wall. It can be seen in Figure 3-6 (b) that when the PCM is heated from below some spaced counter-rotating roll cells are created at the heat source. As time passes, the small roll cells evolve and are combined to create bigger circulations until the melting front reaches the top side and the whole PCM is melted. It can be seen that among all five cases, PCM melts is completely melted at t=5000 s in PGPFX and NGPFX, and they have the fastest melting when the heat source is located at the bottom wall. For this heating configuration, the porosity gradient direction of PGPFX and NGPFX is perpendicular to the main direction of heat transfer. In PGPFX, the porosity linearly increases from left to the right wall. At the right side of the heat source where the porosity is higher, the natural convection effects get stronger with more roll cells being formed; while at the left side, lower porosity suppresses natural convection effects and fewer roll cells are observed. However, relatively higher amount of metal

foam facilitates the thermal conduction at the left side of the heat source. After a while, all formed roll cells at the left and right side are combined to a global roll cell. The melting is slightly delayed at the right side of the enclosure. Since there is no favored part for natural convection when the heat source is placed at the bottom wall, PGPFX and NGPFX have exactly the same but mirrored melting behavior. For the homogeneous case, as the PCM melts, the roll cells combine to create two bigger dominant melting cells which stay until the end and accelerate the melting process. In their experimental work, Zheng et al. [42] have also discussed about these two symmetrical annular flows for homogeneous metal foam when the heat source is placed at the bottom wall. As shown in Figure 3-6 (b), the porosity gradient direction of PGPFY and NGPFY is parallel to the main direction of heat transfer. PGPFY has the lowest porosity at the bottom part, and hence the highest thermal conduction which leads to the dominant role of heat conduction in the phase change. It can be seen that formation of the roll cells is delayed for PGPFY due to the suppression of natural convection at the bottom wall and liquid circulations are formed when the overall melting front gets closer to the top wall. NGPFY has the highest porosity at the heat source, and therefore, natural convection effects are dominant at the heat source resulting in closer formed roll cells to the bottom wall compared to the PGPFY case. However, it can be seen in Figure 3-6 (b) that lack of thermal conduction at the heat source for NGPFY leads to a significantly slower melting rate compared to other cases.

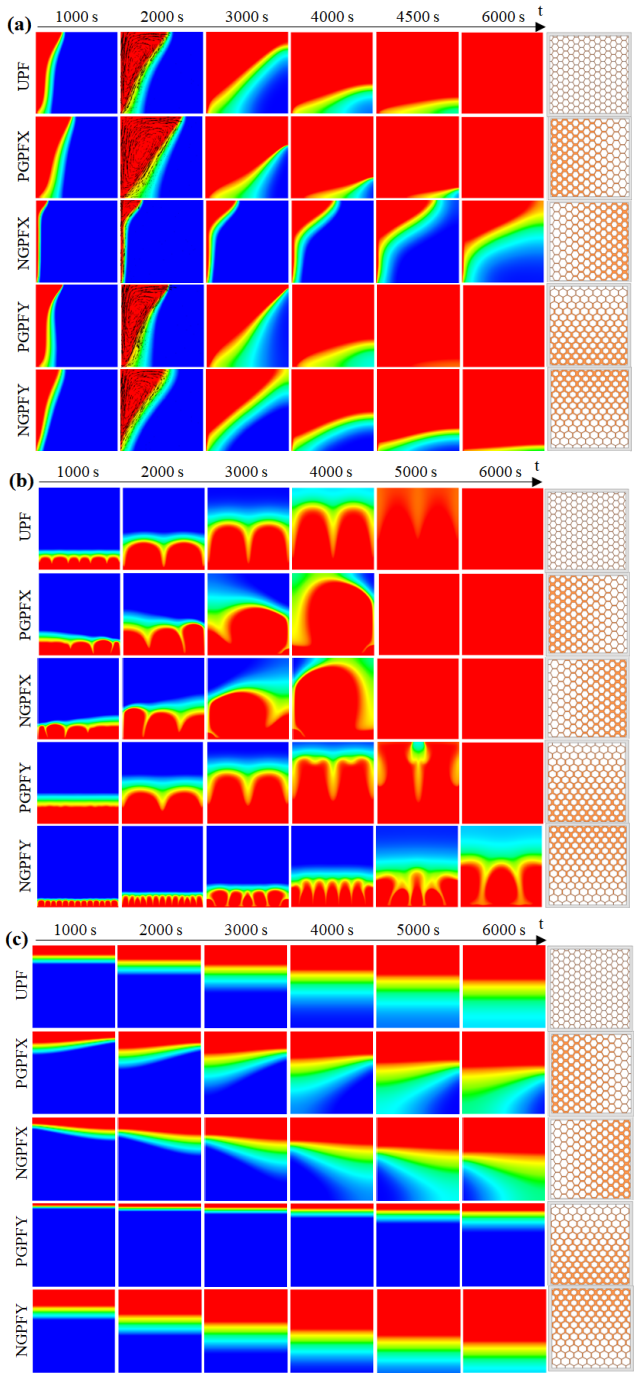

Figure 3-6 Melting evolution of different porous foam structures as TCE in PCM: UPF with $\varepsilon = 0.895$, PGPFX with $\varepsilon_x = 0.7$ to 0.99, NGPFX with $\varepsilon_x = 0.99$ to 0.7, PGPFY with $\varepsilon_y = 0.7$ to 0.99, and NGPFY with $\varepsilon_y = 0.99$ to 0.7, when heating from (a) left, (b) bottom, and (c) top wall with heat source temperature of $T_H = 340$ K.

Figure 3-6 (c) shows the melting evolution for the five cases when the heat source is placed at the top wall. Phase change process starts from the top wall and moves downward until all of the PCM is melted. For this configuration where the main heat transfer is in the direction of gravity, no natural convection is formed, and the heat is transferred from top to the bottom surface exclusively by thermal conduction. As a result, the case that provides the highest thermal conductivity at the vicinity of the heat source, which here is the NGPFY case, has the fastest melting. On the other hand, the PGPFY case has the slowest melting due to a lower conductivity at the top wall. The melting behavior of PGPFX and NGPFX cases are similar to each other when heated from top. For these two cases, the melting front moves further at the side that has lower porosity and higher thermal conductivity.

Figure 3-7 compares liquid fraction for the uniform and all the gradient porosity foam cases heated from different directions with heat source temperature of 340 K. The average PCM liquid fraction for the five porous structures heated from left is plotted in Figure 3-7 (a). It can be seen that among all five cases, PGPFX has the highest liquid fraction at the beginning of phase change process followed by PGPFY and UPF cases. PGPFX has higher thermal conductivity at the heat source which results in a faster heat penetration and more amount of melted PCM at the beginning. However, at the final stages of melting, a turning point is observed and the liquid fraction of PGPFY increases with a higher rate compared to the other cases while the melting rate of PGPFX decreases. Eventually, PGPFY ends up with a lower complete melting time followed by UPF and then PGPFX. As mentioned in the discussion of Figure 3-6 (a), this turning point is attributed to the slower melting rate of PGPFX at the bottom right section of the enclosure due to lower local thermal conductivity at this point, and also higher suppression of liquid circulations which get bigger during the final melting phase. The PGPFY case provides higher thermal conduction at the bottom and lower resistance to convection at the top part of the heat source. Therefore, heat is transferred more

effectively to the right side of the enclosure during final melting phase resulting in a smaller total melting time. The NGPFX structure has the slowest melting in all stages of melting process.

The same turning point behavior can be observed when the heat source is placed at the bottom wall as shown in Figure 3-7 (b). When heated from below, the PGPFY case provides higher thermal conduction at the heat source, and therefore, has higher liquid fraction in the initial melting phase. However, as the PCM melts, the average liquid fraction for PGPFX and NGPFX cases increases with a relatively faster rate, and ultimately the embedded PCM melts faster for these two porous structures. PGPFX and NGPFX have high thermal conductivity at one side and low resistance to convection at the other side of the heat source. The faster melting rate at the final stages can be attributed to the effect of natural convection which is stronger for the PGFPX and NGPFX. Among all cases heated from below, the NGPFY case has the lowest thermal conductivity at the heat source, and hence the slowest melting.

In Figure 3-7 (c) the liquid fraction values are compared for the uniform and gradient porosity cases when heated from top wall. Since in this heating configuration there is no natural convection, no turning point is observed and NGPFY case which has higher thermal conductivity at the heat source, has faster melting rate than the other cases. The PGPFX, NGPFX, and UPF cases have almost the same liquid fraction at all times during phase change process. The PGPFY has slowest melting among all cases.

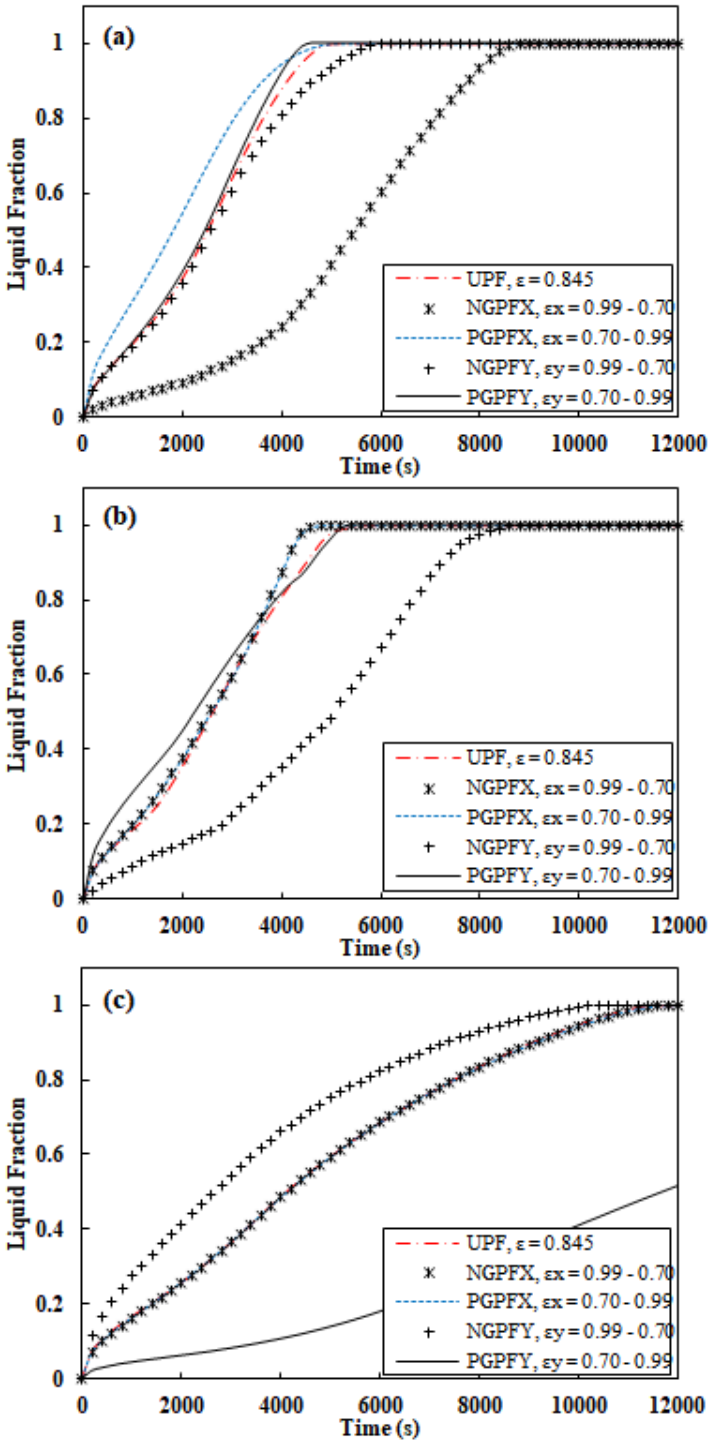

Figure 3-7 Variation of liquid fraction during the phase change process for the uniform and gradient porosity foams heated from (a) left, (b) bottom, and (c) top with heat source temperature of 340 K.

The energy storage density, storage rate, and the complete melting time are compared in Figure 3-8 for all uniform and gradient porosity cases heated from left, bottom, and top walls. As it can be seen, the complete melting time is much higher for the cases heated from top due to absence of natural convection, and therefore, they have lower energy storage rates. The complete melting times are comparable for the cases heated from left and bottom walls. It can be seen that, for the current average porosity, improvement effect of the gradient structures compared to a homogeneous case is slightly more considerable when the heat source is placed at the bottom wall. The PGPFX structure reduces the melting time of the UPF by 15.63% when the heat source is placed at the bottom, while this time reduction for a PGPFY case heated from left wall is about 8.04%. As discussed before, it can be seen in Figure 3-6 that when the heat source is placed at the left wall, a global circulation is formed at the left side of the unit, and despite the differences, this general pattern can be observed for all cases. However, when the enclosure is heated from bottom wall, more distinct melting patterns can be seen when various gradient porous structures are used. It can also be noted that, at an average porosity of 0.845 the homogenous foam structure has a lower melting time when heated from left compared to the case when it is heated from bottom. This can be attributed to the effect of natural convection. For the UPF case heated from left a global circulation is formed from the beginning of phase change process while for the UPF heated from bottom small rolling cells are formed at bottom which are then combined to form bigger ones at later stages. Melting patterns for other average porosities will be discussed later.

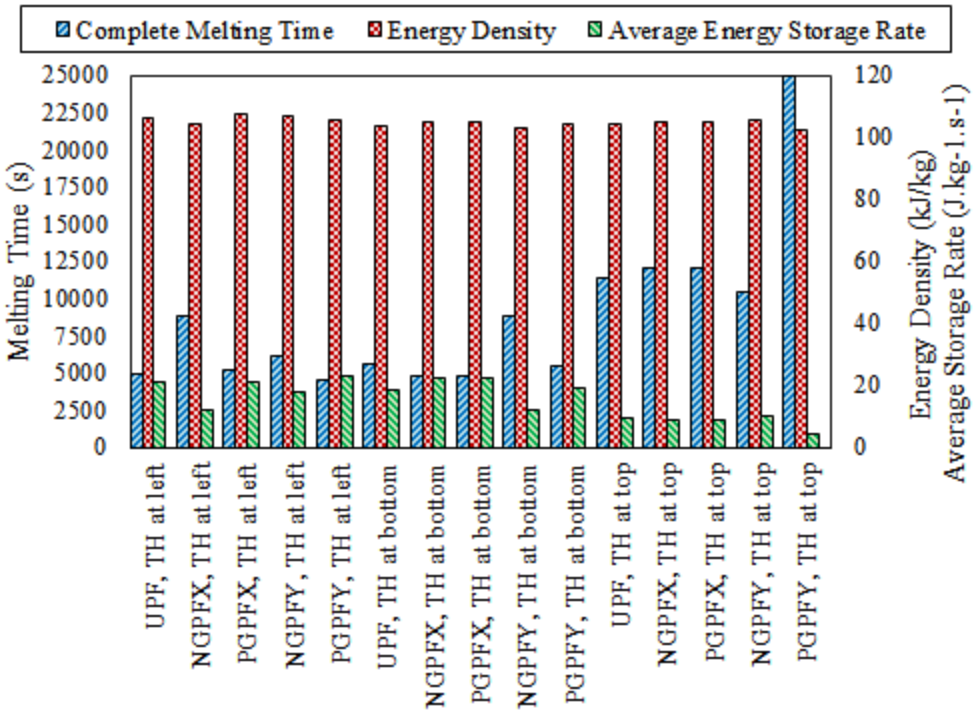

Figure 3-8 Comparison of complete melting time, energy storage density, and energy storage rate for the uniform and gradient porosity foams heated from left, bottom, and top walls with heat source temperature of 340 K.

3.2. Effect of PPI on melting process of graded porous TCEs

In this section, effect of the number of pores per inch (PPI) in the porous metal foam on the performance of the TCEs with graded structures is discussed. To investigate the effect of PPI, first the performance of TCEs with gradient porosity is studied at different PPIs. Then, the porosity is kept constant and the effect of changing PPI in different directions is studied just as like as the cases for gradient porosity.

3.2.1. TCEs with gradient porosity at different PPIs

Figure 3-9 shows liquid fraction variation of uniform and gradient porous metal TCEs heated from left, bottom, and top walls at $PPI = 10$ with a heat source temperature of $T_H = 340$ K. By comparing the results with Figure 3-7 in which the pore density is $PPI = 5$, it can be found

that generally the complete melting times has increased with increasing the PPI. Moreover, the increase in the melting rate is more significant for the cases which are heated from left and bottom. This is due to the fact that by increasing pore density at the same porosity, the pore diameters inside the metal foam will become smaller which will result in decreasing the permeability and hence increasing the resistance to the natural convection. Therefore, in the cases where the natural convection plays an important role in the melting of the PCM—cases heated from left and bottom—increasing PPI has a more significant effect in the melting rate. For the cases heated from left, a comparison of Figure 3-7 (a) with Figure 3-9 (a) shows a similar general trend for both pore densities. Although the natural convection is suppressed at the higher PPI and vortex formations are delayed and slowed, the melting behavior for the cases heated from left follows the same pattern as the lower PPI in which global circulations are formed at the heat source. The PGPFY still has the lowest melting time and NGPFX and NGPFY worsen the melting rate compared to the UPF case. However, compared to $PPI = 5$, the PGPFX case shows improvement respect to the UPF case in $PPI = 10$. The difference between the liquid fraction of PGPFX and other structures is higher at $PPI = 10$ in the beginning and intermediate melting phases. This can be explained by the fact that PGPFX have the highest thermal conductivity at the heat source when the energy storage unit is heated from left. Increasing the pore density will affect the pore and fiber diameter of the metal foam which will change the heat conduction and convection process inside the enclosure. Therefore, at higher pore densities where natural convection effects are more suppressed, thermal conduction plays a more important role in melting of the PCM. As a result, at a higher PPI, the gradient porous cases which have higher conductivity at the heat source show improvement in melting compared to the uniform porosity structure. However, during the final melting phase when most parts of the PCM are melted, the previously discussed deceleration in the melting rate for PGPFX is more severe.

Increasing the PPI for the cases heated from bottom has a more significant effect on the melting behavior of the porous metal foams and unlike the cases heated from left, the melting patterns considerably change at higher PPI. By comparing Figure 3-7 (b) with Figure 3-9 (b), it can be seen that the PGPFX and NGPFX have the smallest melting time at $PPI = 10$ (14% lower than the UPF case). Just as the case discussed above for left-heated PGPFX, the liquid fraction of the bottom-heated PGPFY structure has a bigger difference in the beginning of melting at $PPI = 10$. However, a significant deceleration of the melting rate is observed in the final phase specially between $t = 6000$ s and $t = 8000$ s. This can be attributed to the suppression effect of a higher PPI on the cases heated from bottom which delays the formation, combination, number, and velocity of the roll cells. For PGPFY which already has the highest suppression among the cases heated from bottom, the formation of the vortices is considerably delayed at a higher PPI. The PGPFX and NGPFX cases have a perpendicular gradient porosity direction to the main direction of heat transfer which results in a high conductivity at one side of the heat source while having enough room for natural convection at the other side. Therefore, effects of natural convection are seen at sooner times which facilitates the phase change resulting in a smaller melting time. It should be noted that NGPFY still has the slowest melting time when heated from bottom due to limited thermal conductivity at the heat source. For the cases heated from top, as discussed before, since there is no natural convection, PPI has smaller effect. By comparing Figure 3-7 (c) and Figure 3-9 (c), it can be seen that all five porous structures show the same melting trend with NGPFY having the lowest and PGPFY the highest melting times respectively.

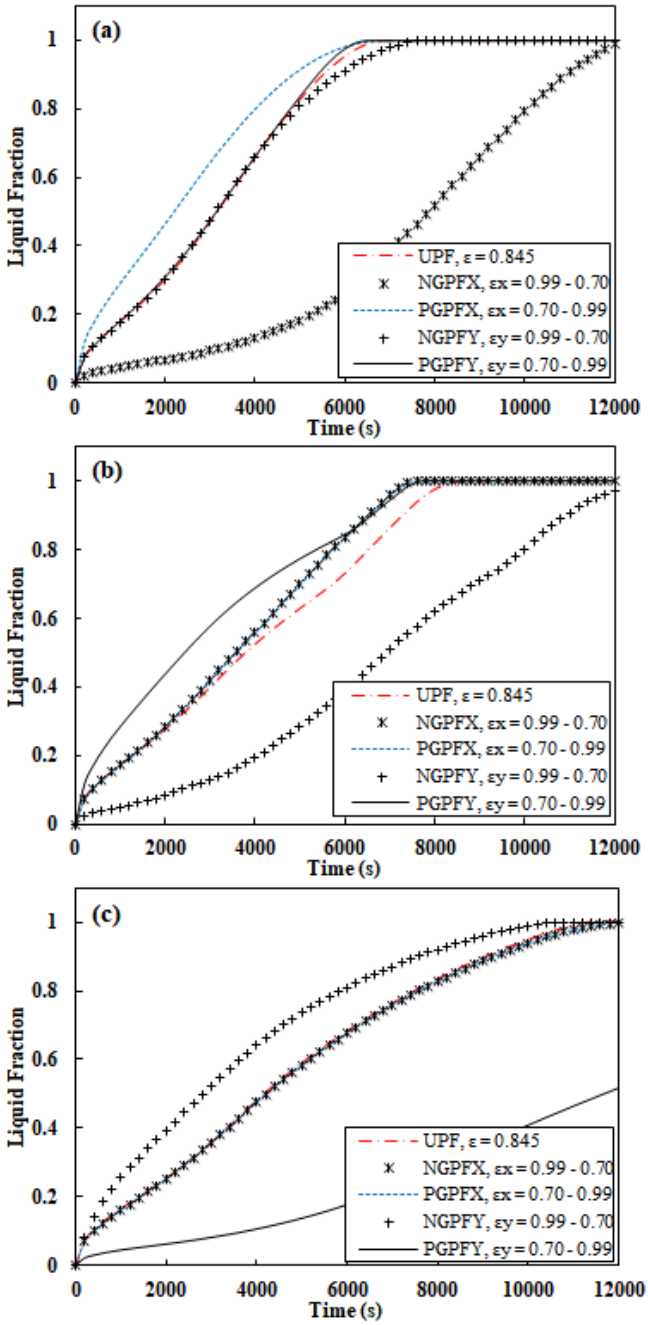

Figure 3-9 Variation of liquid fraction during the phase change process for the uniform and gradient porosity foams heated from (a) left, (b) bottom, and (c) top at PPI = 10.

3.2.1. Foam structures with graded PPI

In this section, the porosity of the metal foam TCEs is kept constant while the pore density is changed in different directions. Figure 3-10 shows the variations of liquid fraction for uniform and gradient PPI metal foams when heated from left, bottom, and top walls with a heat source temperature of $T_H = 340$ K. For all cases an average porosity of $\varepsilon = 0.9$ and average pore density of $PPI = 10$ are considered. The same terminology for the homogeneous and gradient porous structures have been used here. For the gradient PPI cases, the pore density is changed from 5 at one side to 15 at the other side of the enclosure. Since value of the PPI throughout the enclosure has a significant effect of the natural convection, studying of changing PPI will help to better understand the sole role of natural convection on melting the PCM. As can be seen in Figure 3-10 (c), the average liquid fraction curves of all uniform and gradient PPI structures nearly overlap when heated from top wall during the entire period of melting process. This shows that for the metal foam structures with the same average PPI and porosity, when the heat source is placed at the top wall, changing the PPI throughout the enclosure has no considerable effect on the melting process since there are no liquid PCM circulations. However, for the cases where the heat source is placed at the left and bottom walls, and there is a considerable effect of natural convection, changing PPI throughout the enclosure will change the behavior of the melting. As can be seen in Figure 3-10 (a), when the enclosure is heated from left side, the fastest complete melting time is for the PGPFX case in which the pore density is increasing from 5 at the left to 15 at the right side providing the most space among the metal foam TCEs for natural convection. On the other hand, the NGPFX case with pore density changing from 15 at the left to 5 at the right side, has the largest complete melting time due to higher natural convection suppression at the heat source. The melting behavior of the other three cases are very close and fall between the PGPFX and NGPFX cases.

For the cases heated from bottom shown in Figure 3-10 (b), the PGPFY case with lower PPI of 5 at the heat source and higher PPI of 15 at the top side, has the fastest melting until $t = 6000$ s due to more effective natural convection at the heat source. After that, a turning point happens and the PGPFX and NGPFX structures melt faster and eventually have smaller complete melting time. The PCM has difficulty in melting at the top part of the enclosure in the final stages which decelerates the overall melting rate. In the PGPFX and NGPFX one side of the foam structure has more space due to lower PPI, the small roll cells of the molten PCM have more room to combine and form bigger circulations. The NGPFY case has an opposite structure compared to PGPFY case and the slowest melting time among the foam structures heated from bottom.

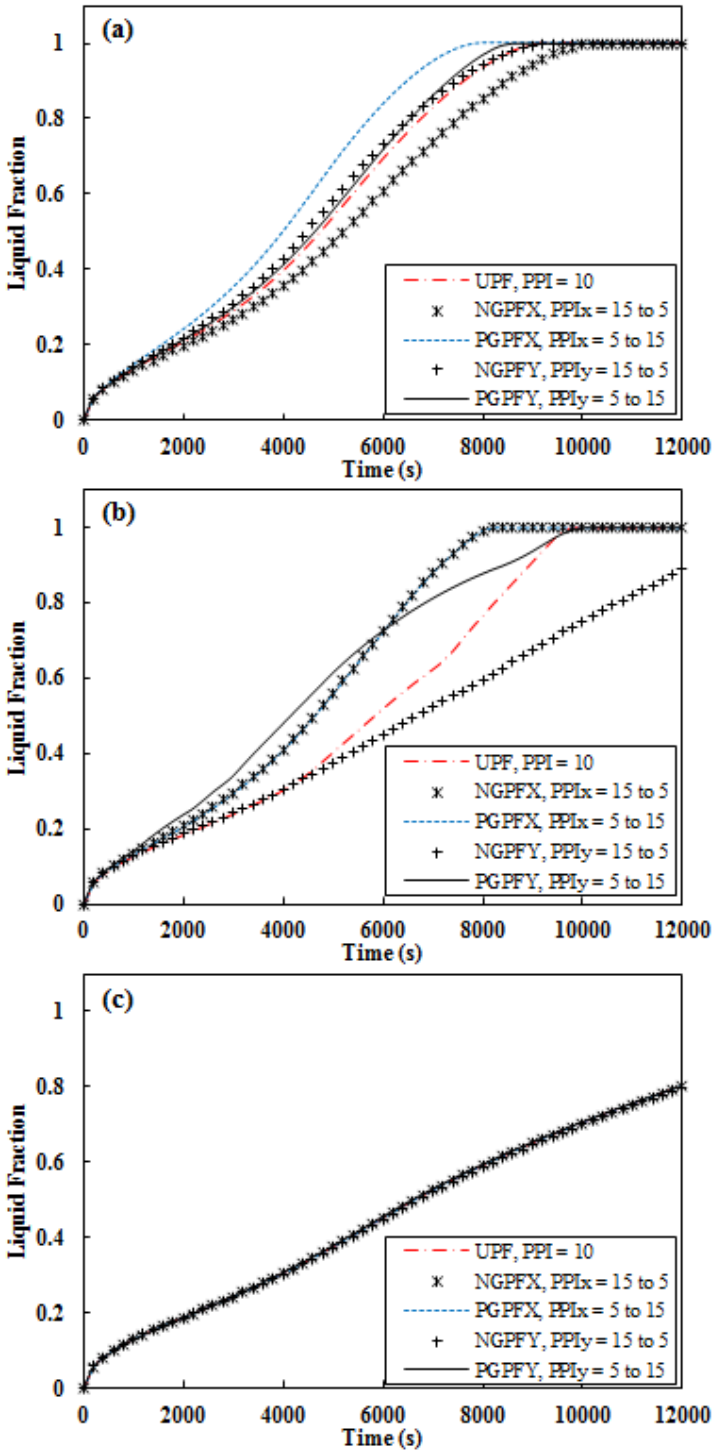

Figure 3-10 Variation of liquid fraction during the phase change process for the uniform and gradient PPI foams heated from (a) left, (b) bottom, and (c) top with heat source temperature of 340 K

3.3. Effect of porosity parameters

In this section, the effects of the gradient porosity parameters on the performance of the PCM-based energy storage systems are investigated. For a gradient porous metal foam TCE, the parameters that determine the porosity distribution are the porosity change rate (m) and the average porosity ($\bar{\varepsilon}$) of the metal foam. Effect of each of these parameters are discussed in this section for six candidate cases which have better melting performance according to the results in the previous sections. Homogeneous and positive gradient porous foams in x and y directions heated from left and bottom walls are chosen. The results for cases heated from top wall are not shown due to absence of natural convection and high melting times. Three porosity change rate of $m = 0.9$, $m = 1.9$, and $m = 2.9$ at constant average porosity of $\bar{\varepsilon} = 0.845$ are considered. For average porosity cases, three average porosities of $\bar{\varepsilon} = 0.92$, $\bar{\varepsilon} = 0.87$, and $\bar{\varepsilon} = 0.82$ with a porosity change rate of $m = 1.4$ are considered. Figure 3-11 shows variation of liquid fraction during the phase change process for the six candidate cases with different porosity change rates and average porosities heated from left and bottom walls. In the cases where porosity change rate is studied, the average porosity is kept constant, and similarly in the cases where average porosity is studied, the porosity change rate is kept constant. Moreover, effect of the porosity change rate (m) and average porosity (ε_{ave}) on the complete melting time, energy density, and energy storage rate for the selected cases is shown in Figure 3-12 (a) and (b) respectively.

Melting curves for UPF, PGPFX, and PGPFY structures with average porosity of $\varepsilon_{ave} = 0.845$ and porosity change rates of $m = 0.9$, 1.9, and 2.9 heated from left wall are shown in Figure 3-11 (a). As can be seen, for all porosity change rates (m) of 0.9, 1.9, and 2.9, the previously discussed turning point behavior is observed in which the PGPFX cases have higher molten PCM in the beginning but fall behind the PGPFY cases in the final stages of the phase change process.

It can also be seen in Figure 3-12 (a) that when heated from left, PGPFY cases have smaller complete melting times compared to UPF and PGFPX structures. Among the PGPFY cases heated from left, the complete melting time reduces by increasing the porosity change rate (m) in y direction from 0.9 to 2.9. The liquid fraction for these cases is very close in the beginning, but as the PCM melts, the case with higher m of 2.9 ($\varepsilon_y = 0.7$ to 0.99) melts faster due to better thermal conduction at the bottom, and natural convection at the top part of the enclosure. A similar behavior is also shown in [46] for porous metal foams with linear changing porosity. The PGFPY foam structures with m of 2.9, 1.9, and 0.9 reduce the complete melting time of a uniform case by 8.04%, 6.03%, and 3.52%. Therefore, the reduction rate in the melting time is bigger at smaller values of m and decreases at bigger values.

Observed melting characteristics for the PGPFX cases with different porosity change rates (m) when heated from left can be found in Figure 3-11 (a) and Figure 3-12 (a). When heated from left, by increasing m in the x direction for PGPFX cases, the complete melting time first decreases (when m changes from 0 to 0.9) but then starts to increase (when m changes from 0.9 to 2.9). Compared to the UPF case, the PGPFX with m of 0.9 ($\varepsilon_x = 0.8$ to 0.89) has a lower melting time while the case with m of 2.9 ($\varepsilon_x = 0.7$ to 0.99) has a higher one. The cases with higher m have higher liquid fraction at the beginning due to higher thermal conductivity at the heat source. But at the final melting phase a turning point occurs and the cases with lower m end up melting faster.

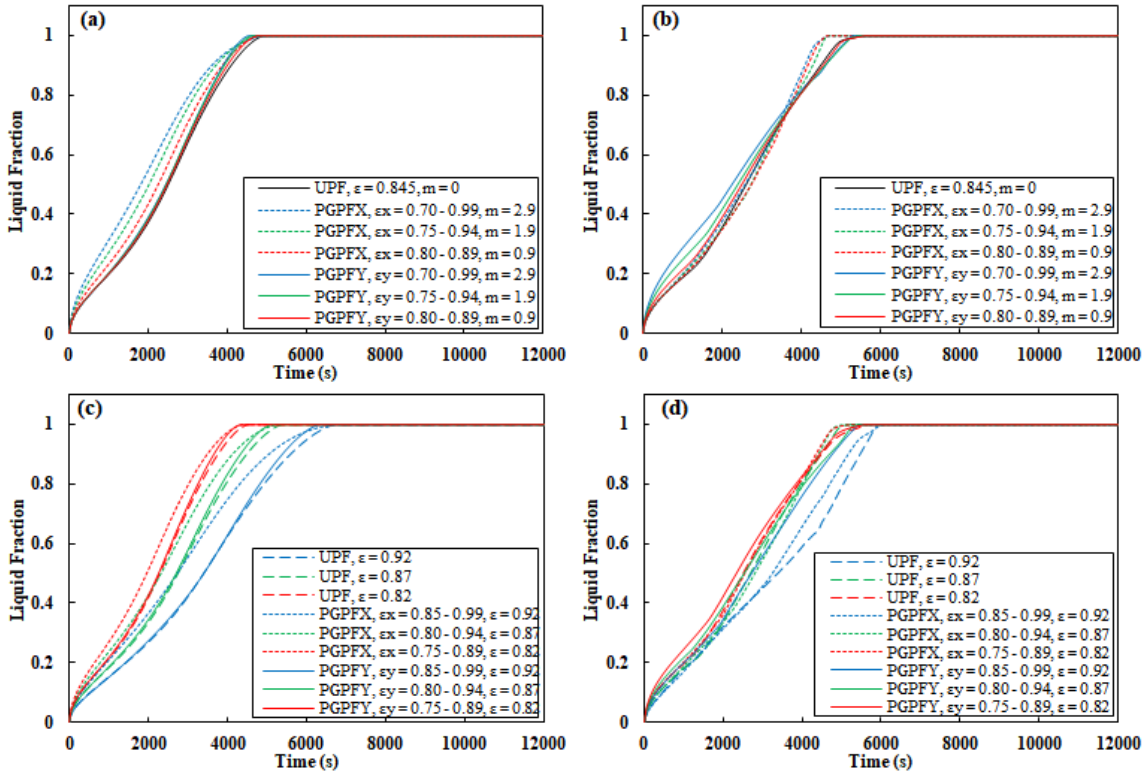

Figure 3-11 Variation of liquid fraction during the phase change process for (a) cases heated from left with average porosity of $\varepsilon_{ave} = 0.845$ and different m; (b) cases heated from bottom with average porosity of $\varepsilon_{ave} = 0.845$ and different m; (c) cases heated from left with porosity change rate of $m = 1.4$ and different ε_{ave}; (d) cases heated from bottom with porosity change rate of $m = 1.4$ and different ε_{ave}.

Liquid fraction variations of UPF, PGPFX and PGPFY cases with average porosity of $\varepsilon_{ave} = 0.845$ and different porosity change rates of $m = 0.9$, 1.9, and 2.9 heated from below is shown in Figure 3-11 (b). As can be seen, for all considered values of m, the turning point behavior is found in the melting curves where the PGFPY cases with higher conductivity at the heat source have higher liquid fraction value in the beginning of the phase change process, but in the final stages, PGPFX cases have higher melting rate. Therefore, it can be seen that the complete melting time for the PGPFX foams is smaller than the PGPFY cases when heater from bottom. As can be found in Figure 3-11 (b) and Figure 3-12 (a), the melting time for PGPFX structures is lower than the UPF at all studied porosity change rates. Complete melting time increases by increasing the m

from 0.9 to 2.9 for bottom heated PGPFX foams. Although the bottom-heated PGPFX with $m = 2.9$ have a higher porosity at one side of the enclosure providing more room for natural convection, it also has a lower local conductivity compared to the cases with $m = 0.9$. This implies that better natural convection at high porosity zone ($\varepsilon = 0.99$) has not compensated for the lower thermal conductivity at this point which eventually leads to a lower melting rate. However, the differences between the complete melting times of PGPFX foams at different values of m are rather small. For the bottom heated PGPFY foams it can be seen from Figure 3-11 (b) and Figure 3-12 (a) that the complete melting times at different m are closer to the UPF case compared to PGPFX foams. The melting time is biggest for bottom heated PGPFY with $m = 0.9$ and then decreases by increasing m. Suppression of natural convection at the heat source shows its effect at $m = 0.9$ but by further increasing the m, higher thermal conductivity overcomes this suppression. It should be noted that as mentioned for PGPFX cases, the differences are rather small among PGPFY cases as well. It can be pointed out that in general, since improving conductivity in the TCE foams suppresses natural convection, balance between the two heat transfer mechanisms determines melting improvement in a design and effective use of both results in better performance.

Variation of liquid fraction for UPF, PGPFX, and PGPFY cases with average porosities of 0.82, 0.87, and 0.92 and porosity change rate of $m = 1.4$ heated from left are shown in Figure 3-11 (c). Generally, changing the average porosity has more distinct effect on the melting of the PCM inside the enclosure since the amount of the PCM changes by changing ε_{ave}. It can be seen that by increasing the average porosity for the uniform and gradient cases, the time required for melting of the PCM also increases. This effect of the average porosity in melting process of the PCMs is well studied in the literature for uniform porosity cases [30,34, 43,57,60,61]. The melting behavior for the gradient cases is generally similar to the case with average porosity of $\varepsilon\_ave = 0.845$ which has been discussed before. As can be found in Figure 3-11 (c) and Figure 3-12 (b), at all average

porosities of 0.82, 0.87, and 0.92, the liquid fraction for the PGPFX case is higher in the initial phase while in the final phase, it is higher for the PGPFY case. Although the PGPFY case has the lowest melting time at all three values of ε_{ave}, the complete melting time gets closer for the three cases at lower average porosities. Therefore, the performance improvement of the PGPFY in melting, is more prominent at higher porosities. On the other hand, at lower average porosities in which the natural convection effects become weaker, PGPFX shows more improvement in melting compared to the uniform structure.

Melting curves for UPF, PGPFX, and PGPFY cases with average porosities of 0.82, 0.87, and 0.92 and porosity change rate of $m = 1.4$ heated from bottom are shown in Figure 3-11 (d). The complete melting times for these cases are compared in Figure 3-12 (b). As can be seen, the melting behavior for this heating configuration is different from what has been observed for the cases heated from left. The cases heated from bottom generally have faster melting at high porosities compared to the cases heated from left. On the other hand, when the average porosity decreases, the left-heated cases melt faster. This can be seen in Figure 3-12 (b) by comparing the complete melting times for the left and bottom heated cases at high porosity ($\varepsilon = 0.92$, $\varepsilon_x = 0.85 - 0.99$, and $\varepsilon_y = 0.85 - 0.99$) and low porosity ($\varepsilon = 0.82$, $\varepsilon_x = 0.75 - 0.89$, and $\varepsilon_y = 0.75 - 0.89$). This also stands for the pure PCM cases where left-heated enclosure melts about 6.3% slower than the bottom-heated enclosure for the assumed size (data not shown). This indicates that at high porosities where natural convection effects are more dominant, liquid circulations are more effective in melting the PCM when the constant temperature heat source is placed at the bottom compared to the left wall. It should be noted that when the heat source is placed at the left wall, although a bigger liquid circulation is formed, most of the melting occurs at the top side of the enclosure and the bottom right side remains in solid phase for a long time which is a disadvantage for the left-heating configuration. On the other hand, when the heat source is placed

at the bottom, a uniform melting occurs and there is no favored side for liquid circulations. As discussed in previous sections, faster melting depends on an ideal balance between the natural convection and thermal conduction effects. When the heat source is placed at bottom, a uniform case with $\varepsilon_{ave} = 0.92$ improves the melting time by about 64% compared to a pure PCM case. Decreasing the porosity will also decrease the melting time until the case where average porosity is 0.87. However, further decreasing the porosity from 0.87 to 0.82 results in a higher melting time, since natural convection, which is more crucial at the final melting stages, is more suppressed. The same trend is observed for PGPFX as the melting time decreases by decreasing the average porosity until $\varepsilon_{ave} = 0.87$ and then starts to increase by further decreasing ε_{ave}. For the PGPFX with $\varepsilon_x = 0.85 - 0.99$ ($\varepsilon_{ave} = 0.92$) there is more room for natural convection but also lack of thermal conduction at the right side of the enclosure. Therefore, an unbalanced melting is observed which delays the melting at the right side of the enclosure. For the PGPFX with $\varepsilon_x = 0.80 - 0.94$ ($\varepsilon_{ave} = 0.87$) better balance between thermal conduction and natural convection occurs at the right side of the enclosure causing a more uniform melting, and consequently, smaller melting time. Further decreasing the average porosity results in more suppression of the natural convection which changes the balance and increases the melting time. For the PGPFY case, smaller melting time in observed at a higher porosity of $\varepsilon_{ave} = 0.92$ ($\varepsilon_y = 0.85 - 0.99$) and further decreasing the porosity results in larger melting times. Generally, among the bottom heated cases, PFGPX structures have smaller melting times at lower average porosities and PGPFY structures have smaller melting times at higher average porosities. Compared to the bottom heated UPF case, at average porosity of 0.87, PGPFX has 13% lower melting time and at average porosity of 0.92, PGPFY has 8% lower melting time.

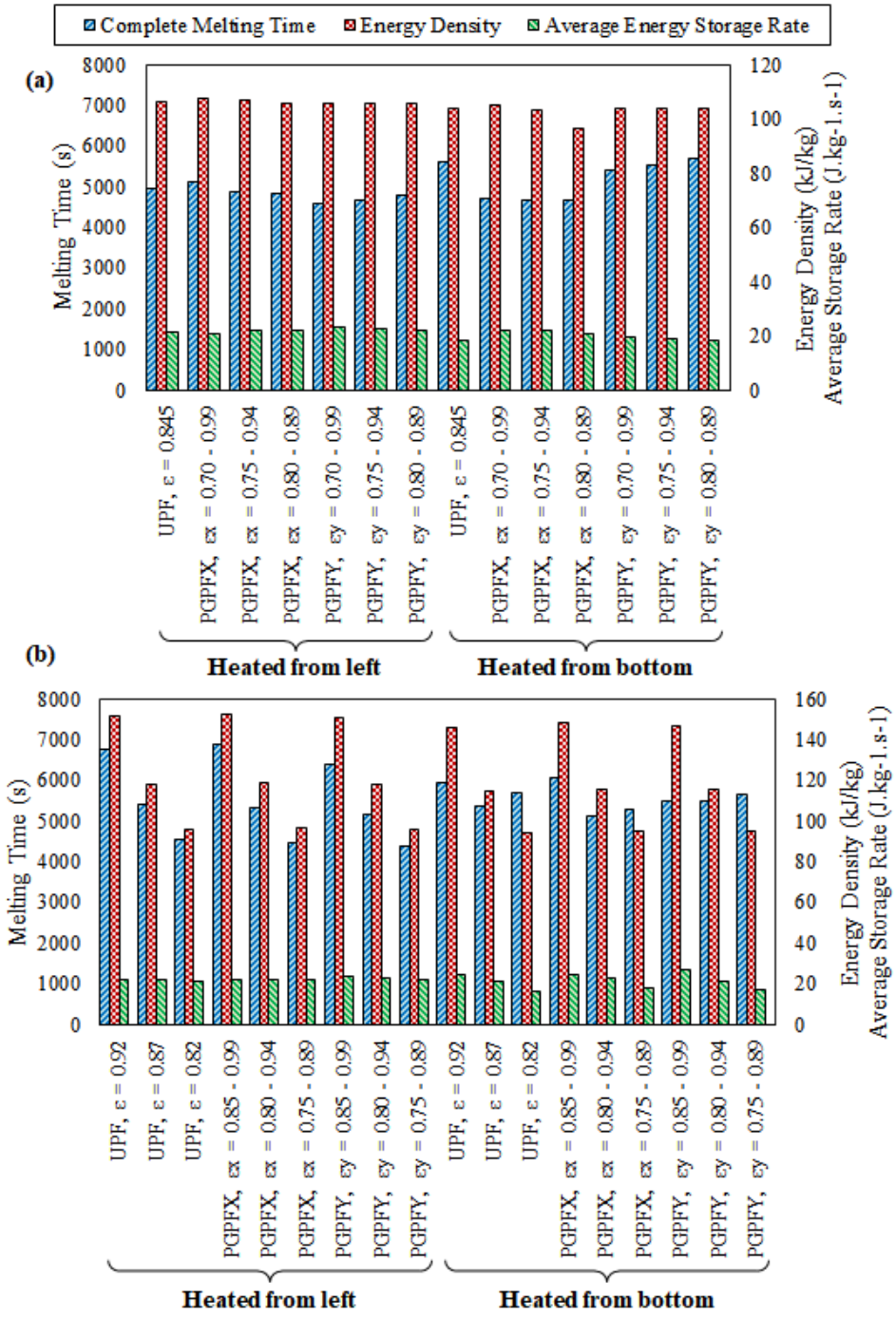

Figure 3-12 (a) Effect of porosity change rate (m) on the complete melting time, energy storage density, and energy storage rate of the UPF, PGPFX, and PGPFY cases with $\varepsilon_{ave} = 0.845$ heated from left and bottom. (b) Effect of average porosity (ε_{ave}) on the complete melting time, energy storage density, and energy storage rate of the UPF, PGPFX, and PGPFY cases with porosity change rate of $m = 1.4$ heated from left and bottom**.**

3.4 Effect of size of the storage system

In this section, the performance of the uniform and the selected gradient porous TCEs is compared and discussed for enclosures of different sizes. First, the effect of width of the enclosure is studied for the UPF, PGPFX, and PGPFY cases heated from left and bottom. Melting of PCM is compared for the enclosures with widths of 100, 150, and 200 mm by keeping the height constant at a value of 100 mm. Then, the effect of height is evaluated for the UPF, PGPFX, and PGPFY cases heated from left and bottom. Similar to the studied cases with various widths, the cases with heights of 100, 150, and 200 mm are investigated by keeping the width at a constant value of 100 mm. The average porosity is kept at a value of $\varepsilon_{ave} = 0.845$ and for the gradient porous cases, the porosity has been changed from 0.70 to 0.99.

Figure 3-13 (a), (b), and (c) show the effect of changing width for the UPF, PGPFX, and PGPFY cases heated from left and bottom at a height of 100 mm. Moreover, Figure 3-14 (a) compares the complete melting time, energy density, and energy storage rate for these cases and their transient melting profile can be found in Figure 3-15. As can be seen, at widths of 150 and 200 mm, the cases heated from bottom melt faster than the cases heated from left due to the bigger heat transfer area and therefore higher input heat. It can be found that, for the cases heated from left, PGPFY melts faster for all widths followed by UPF, and then PGPFX. The melting curves for the left-heated cases show the same trend for all widths with PGPFX having higher melting rate at the beginning but lower at the end. As can be seen in Figure 3-6 (a) and Figure 3-15 (a) and (c) When heated from left, at all widths, the PGPFY case is more effective in melting the bottom right side of the enclosure where is the slowest melting region for left-heated cases. Compared to UPF, using PGPFY is slightly more effective at lower widths as it decreases the complete melting time by about 8.04% at $w = 100$ mm but about 5.67% at $w = 200$ mm. The melting rate for PGPFX gets comparatively worse by increasing the width as the difference can be seen in Figure 3-14 (a)

for $w = 200$ mm. For the cases heated from bottom, the fastest melting at different widths belongs to PGPFY at $w = 200$ mm, to UPF at $w = 150$ mm, and to PGPFX at $w = 100$ mm. Although for the studied cases heated from bottom, PGPFX has smaller melting time at $w = 100$ mm compared to the UPF, it is less effective at higher widths. On the other hand, compared to UPF, the PGPFY structure is found to have bigger melting times at lower widths and smaller one at higher widths. This is due to the fact that the balance of thermal conductivity and natural convection effects changes by increasing the width when heat source is place at the bottom. For PGPFX at $w = 100$ mm, the thermal conductivity and natural convection are balanced at the right side in a way that a uniform melting occurs throughout the enclosure (Figure 3-6 (b)). However, as can be seen in Figure 3-15 (b) and (d), for $w = 150$ and 200 mm, more areas of the right side of the enclosure have high porosity, and lack of thermal conduction leads to a delayed melting at these areas. For PGPFY heated from below, by increasing the width and keeping the height, thermal conduction is increased for a bigger area at the heat source, and the melted PCM reaches the top side of the enclosure before suppression of natural convection takes considerable effect. It should be noted that these results are for the studied cases with $\varepsilon_{ave} = 0.845$ and $m = 2.9$. As discussed in the previous section, a different combination of the porosity parameters can improve or worsen the melting behavior inside the enclosure by changing the balance of the heat transfer mechanisms.

Figure 3-13 (d), (e), and (f) show the effect of changing height for the UPF, PGPFX, and PGPFY cases heated from left and bottom at a width of 100 mm. Furthermore, the complete melting time, energy density, and energy storage for these cases are in Figure 3-14 (b) and their melting profile can be found in Figure 3-16. At heights of 150 and 200 mm, the cases heated from left melt faster than the cases heated from bottom because of larger input heat. As the case where the effect of width was studied, it can be seen that, for the cases heated from left, PGPFY melts faster at all heights. As seen in the melting evolution contours in Figure 3-6 (a) and Figure 3-16 (a) and (c),

this can be attributed to the higher melting rate of the PGPFY at the bottom right section of the enclosure. The improvement in the melting for PGPFY is more at higher heights as there is 7.65% decrease in melting time at $h = 100$ mm but 11% at $h = 200$ mm compared to the UPF. The melting curves show almost the same behavior for the left-heated cases at all heights. The PGPFX melts faster in the beginning but its melting rate slows down during the final phase. For the cases heated from bottom, as indicated in Figure 3-13 (d), (e), (f), and Figure 3-14 (b), PGPFX has the fastest melting at higher heights. The improvement in melting gets more effective at higher heights as there is 15.5% decrease in melting at $h = 100$ mm and 26.4% at $h = 200$ mm compared to the UPF. This can be attributed to the porosity distribution in PGPFX where porosity is changed from left to the right side providing higher thermal conduction at the left and higher natural convection at the right. Moreover, the porosity has changed linearly with a rate (for a width of $w = 100$ mm) that the weight of conduction and natural convection effects are balanced. As shown in Figure 3-16 (b) and (d), this has resulted in a fast uniform melting which transfers the heat from bottom to the top side faster than the UPF and PGPFY cases. For PGPFY cases heated from below, increasing the height has increased the melting rate compared to the UPF case as it has about 15% bigger melting time than UPF at $h = 200$ mm. This is due to the face that by increasing the height, there are larger areas at the top side of the PGPFY where porosity has higher value and therefore thermal conduction is lower. The low thermal conduction in larger areas at the top side has resulted in a slower melting in these regions specially in the final stages. Moreover, natural convection is suppressed in more areas at the bottom part of the enclosure.

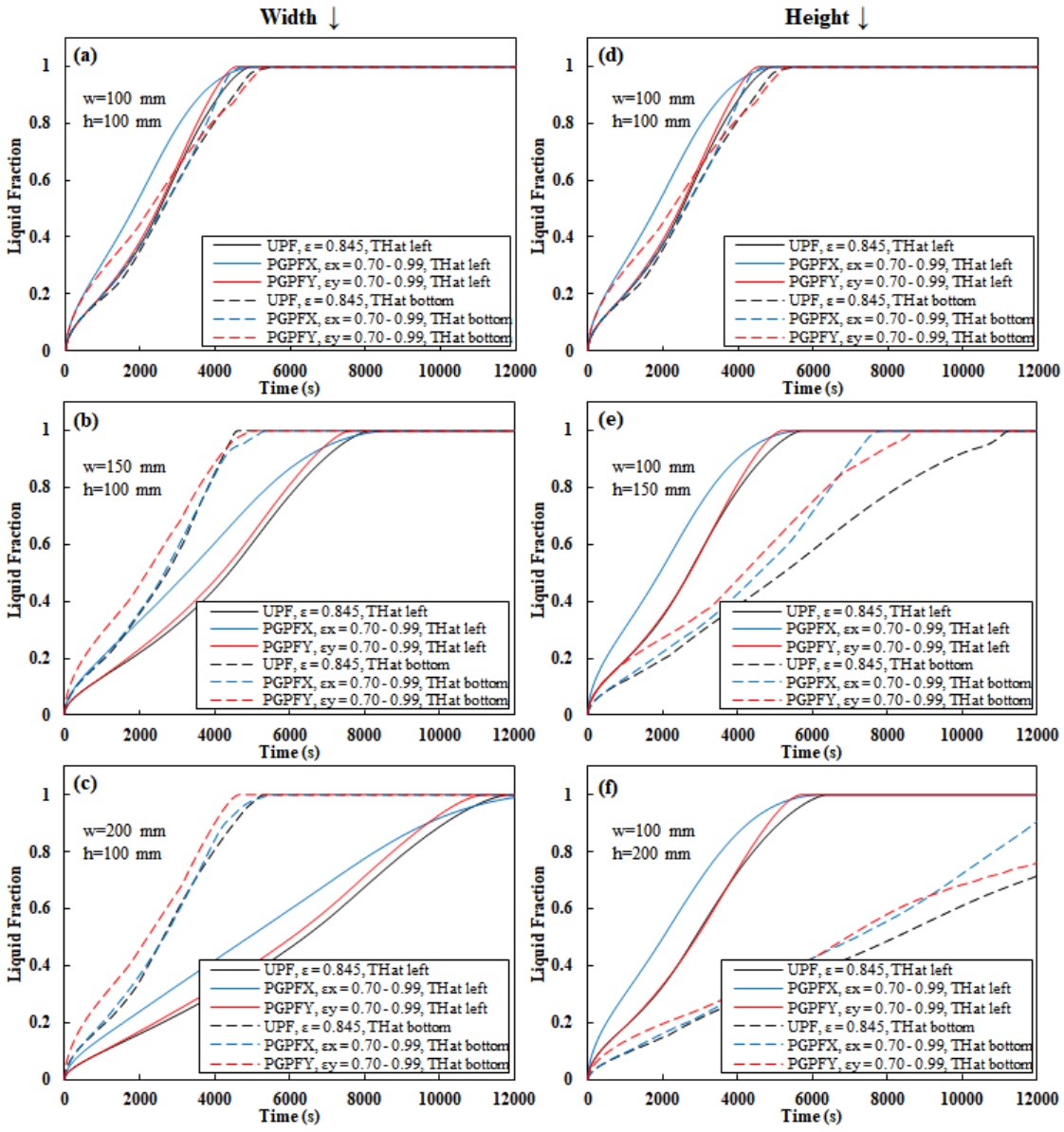

Figure 3-13 Variation of liquid fraction during the phase change process for UPF, PGPFX, and PGPFY metal foams and an enclosure with (a) $w = 100$ mm, and $h = 100$ mm; (b) $w = 150$ mm, and $h = 100$ mm; (c) $w = 200$ mm, and $h = 100$ mm; (d) $w = 100$ mm, and $h = 100$ mm; (e) $w = 100$ mm, and $h = 150$ mm; (f) $w = 100$ mm, and $h = 200$ mm.

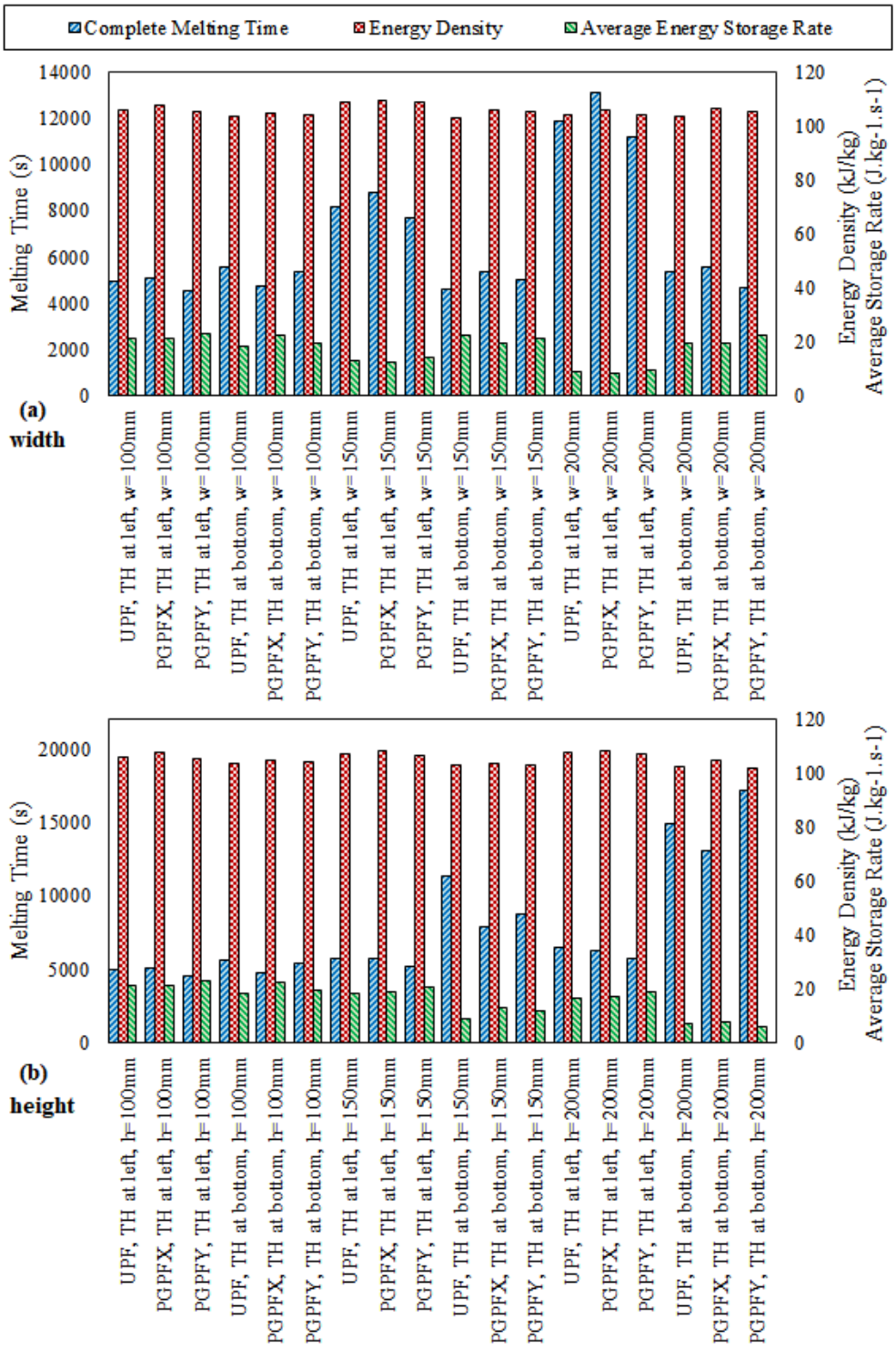

Figure 3-14 Effect of (a) width and (b) height on the complete melting time, energy storage density, and energy storage rate of the UPF, PGPFX, and PGPFY cases heated from left and bottom.

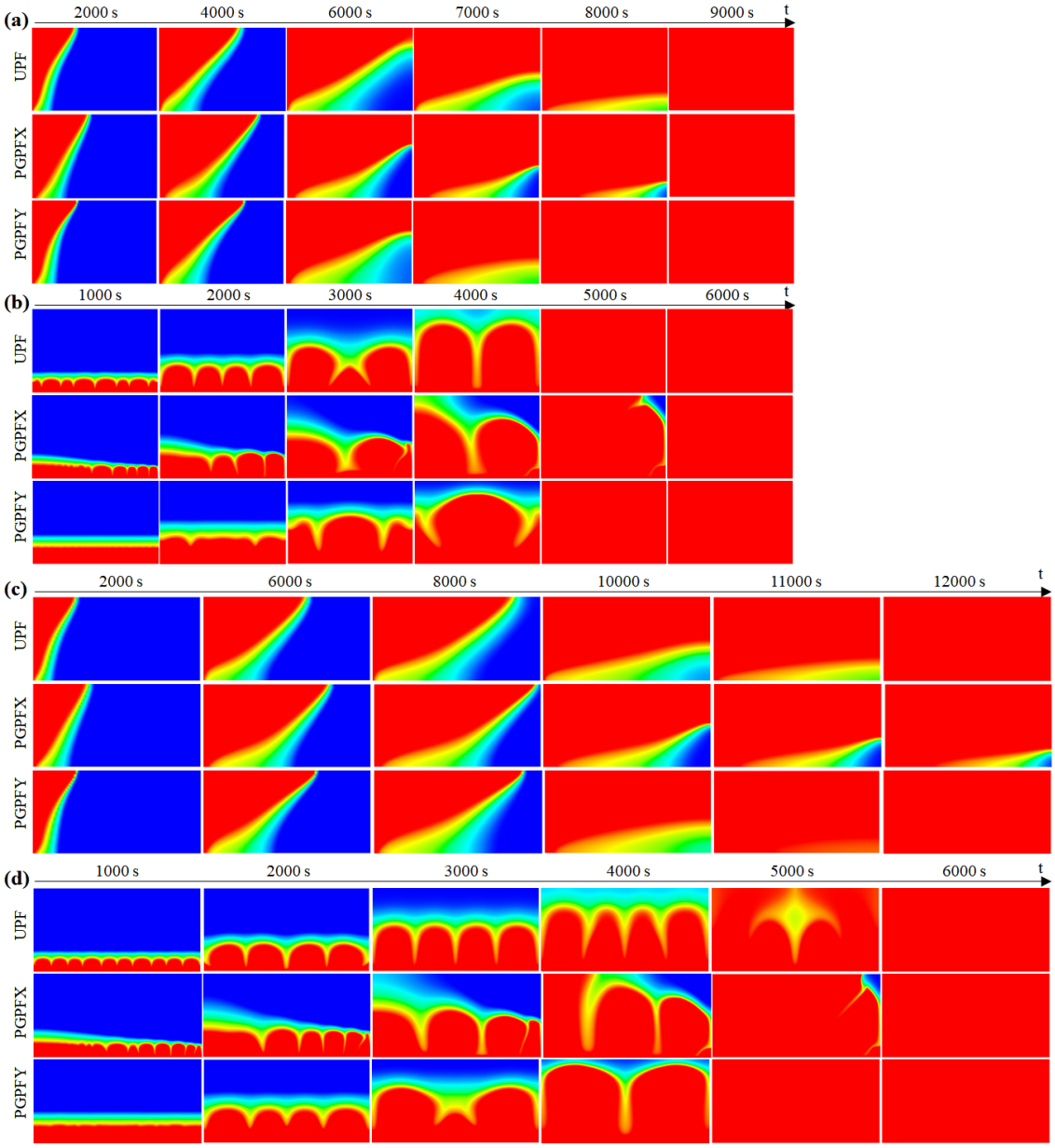

Figure 3-15 Melting evolution for UPF, PGPFX, and PGPFY for (a) $w = 150$ mm and $h = 100$ mm heated from left; (b) $w = 150$ mm and $h = 100$ mm heated from bottom; (c) $w = 200$ mm and $h = 100$ mm heated from left; (d) $w = 200$ mm and $h = 100$ mm heated from bottom.

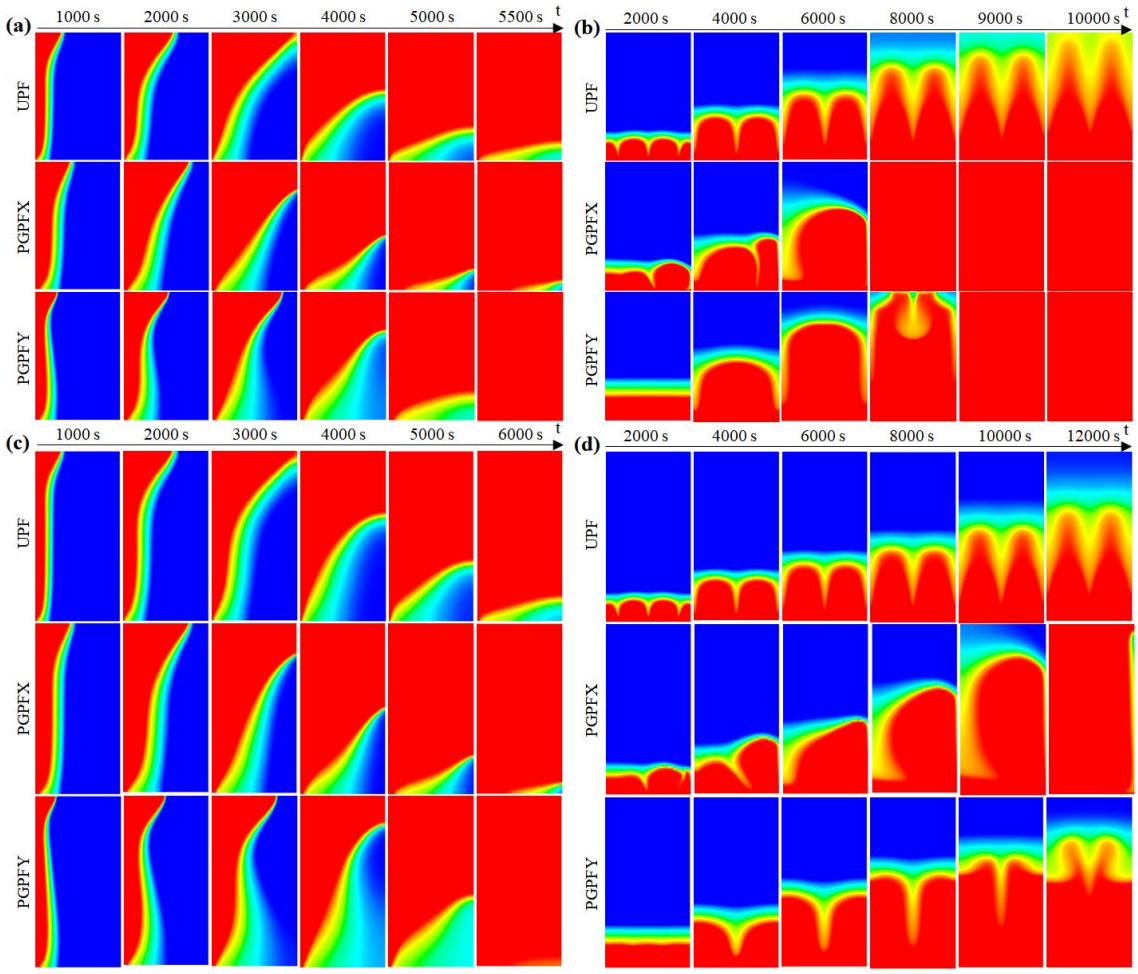

Figure 3-16 Melting evolution for UPF, PGPFX, and PGPFY for (a) $w = 100$ mm and $h = 150$ mm heated from left; (b) $w = 100$ mm and $h = 150$ mm heated from bottom; (c) $w = 100$ mm and $h = 200$ mm heated from left; (d) $w = 100$ mm and $h = 200$ mm heated from bottom.

4. Conclusion

In this chapter, effect of using gradient porous metal foams as thermal conductivity enhancers on melting behavior of phase change materials is investigated. A rectangular enclosure is utilized and a heat source with a constant temperature has been placed at various locations of the enclosure. Five different porous structures, namely, UPF, PGPFX, NGPFX, PGPFY, and NGPFY

are studied for every heating configuration. First, melting patterns and energy storage performance is discussed for the five structures heated from different directions. Then, effects of PPI, porosity parameters, and size of the storage unit has been discussed for the selected designs. The result indicate that the porous characteristics of the metal foam can significantly influence the heat transfer and melting process inside the energy storage unit by affecting the thermal conductivity and natural convection. Faster melting for every set of parameters and heat source locations depends on an ideal balance between the natural convection and thermal conduction effects. When the heat source is placed at the left side, a global circulation is formed at left which grows as the PCM melts. When the heat source is placed at bottom, melting roll cells are formed at the bottom side which may later combine to form bigger circulations. No circulations are formed when the heat source is placed at the top wall. Therefore, melting for the top-heated configurations is significantly slower. It is found that, when the porosity parameters or size of the unit is changed, the melting patterns for the left-heat configurations are generally similar and therefore, their results can be extrapolated. However, the melting behavior of the bottom-heated configurations are significantly affected by changing the settings, and the formation, combination, number, and velocity of the roll cells are varying for different cases. Therefore, more studies are required to obtain the optimized porosity settings for various conditions and sizes of the energy storage unit. For the current considered conditions, the following conclusions are derived based on the observed melting results:

- The cases which have low porosity and hence higher thermal conductivity at the heat source (PGPFX heated from left and PGPFY heated from bottom), have relatively higher rate of melting in the beginning of the phase change process, but then face a turning point and have lower melting rate in the final stages due to higher suppression of natural convection.

- The cases that have highest porosity and hence lowest thermal conductivity at the heat source (NGPFX heated from left, NGPFY heated from bottom, and PGPFY heated from top), have the smallest overall melting time.
- When the heat source is placed at the left wall, PGPFY allows a better natural convection at the top while providing high thermal conductivity at the bottom, and has the fastest melting among the considered structures. Compared to cases heated from left, effect of using gradient structures on the melting profile is generally more considerable when the heat source is placed at the bottom wall. Since the natural convection effects are negligible when the heat source is placed at the top wall, the case that provides the highest thermal conductivity at the heat source (NGPFY here), has the fastest melting.
- The complete melting times has generally increased with increasing the PPI and the change is more significant for the cases which are heated from left and bottom. For bottom-heated configurations the PGPFX structures showed better melting performance at higher pore densities. For the structures with gradient pore density, the cases with increasing PPI from left to right had lower melting times when heated from left and bottom.
- For the studied porosity change rates (m) at a constant average porosity of $\bar{\varepsilon} = 0.845$, the complete melting time is reduced by increasing m for left-heated PGPFY cases. For the left-heated PGPFX, melting time decreases until $m = 0.9$ and then increases.
- Compared to m, changing $\bar{\varepsilon}$ has generally more distinct effect on the melting. Increasing $\bar{\varepsilon}$ resulted in generally bigger melting times for left-heated cases. Also, the performance improvement of the left-heated PGPFY is more prominent at higher average porosities. For bottom-heated UPF and PGPFX, the melting time is reduced until $\bar{\varepsilon} = 0.87$ and then started to rise by further decreasing $\bar{\varepsilon}$. For PGPFY, the melting time is reduced until $\bar{\varepsilon} = 0.92$ and then started to rise by further decreasing $\bar{\varepsilon}$. It is also found that, the left-heated

cases generally melt faster than the bottom-heated ones at lower average porosities while the bottom-heated structures melt faster at higher average porosities.

- In the left-heated conditions, compared to UPF, using PGPFY is slightly more effective at smaller widths and bigger heights. Among the bottom-heated cases, PGPFX showed considerably smaller melting times at higher heights. Increasing the width in bottom-heated PGPFX and increasing height in bottom-heated PGPFY results in bigger melting times.

References

[1] M. Aneke and M. Wang, "Energy storage technologies and real life applications – A state of the art review," Applied Energy, vol. 179, pp. 350-377, 2016.

[2] G. Alva, Y. Lin and G. Fang, "An overview of thermal energy storage systems," Energy, vol. 144, pp. 341-378, 2018.

[3] M. M. Farid, A. M. Khudhair, S. A. K. Razack and S. Al-Hallaj, "A review on phase change energy storage: materials and applications," Energy Conversion and Management, vol. 45, pp. 1597-1615, 2004.

[4] S. Jegadheeswaran and S. D. Pohekar, "Performance enhancement in latent heat thermal storage system: A review," Renewable and Sustainable Energy Reviews, vol. 13, pp. 2225-2244, 2009.

[5] M. Farid, A. Khudhair, S. Razack and S. Al-Hallaj, "A review on phase change energy storage: materials and applications," Energy Conversion and Management, vol. 45, pp. 1597-1615, 2004.

[6] A. Olabi, "Renewable energy and energy storage systems," Energy, vol. 136, pp. 1-6, 2017.

[7] Y. Zhao, C. Zhao, Z. Xu and H. Xu, "Modeling metal foam enhanced phase change heat transfer in thermal energy storage by using phase field method," International Journal of Heat and Mass Transfer, vol. 99, p. 170–181, 2016.

[8] H. Xu and C. Zhao, "Thermal performance of cascaded thermal storage with phase-change materials (PCMs). Part I: steady cases," International Journal of Heat and Mass Transfer, vol. 106, pp. 932-944, 2017.

[9] H. Xu and C. Zhao, "Thermal performance of cascaded thermal storage with phase-change materials (PCMs). Part II: unsteady cases," International Journal of Heat and Mass Transfer, vol. 106, pp. 945-957, 2017.

[10] S. Lohrasbi, M. Sheikholeslami and D. Ganji, "Discharging process expedition of NEPCM in fin-assisted latent heat thermal energy storage system," Journal of Molecular Liquids, vol. 221, pp. 833-841, 2016.

[11] H. Xu and C. Zhao, "Thermal efficiency analysis of the cascaded latent heat/cold storage with multi-stage heat engine model," Renewable energy, vol. 86, pp. 228-237, 2016.

[12] H. Xu and C. Zhao, "Thermodynamic analysis and optimization of cascaded latent heat storage system for energy efficient utilization," Energy, vol. 90, pp. 1662-1673, 2015.

[13] R. Kalbasi and M. R. Salimpour, "Constructal design of horizontal fins to improve the performance of phase change material rectangular enclosures," Applied Thermal Engineering, vol. 91, pp. 234-244, 2015.

[14] R. Kalbasi and M. R. Salimpour, "Constructal design of phase change material enclosures used for cooling electronic devices," Applied Thermal Engineering, vol. 84, pp. 339-349, 2015.

[15] P. Wang, J. Li, L. Zhao, A. Ghahremannezhad and L. Zhou, "Partially shaded heat collector element - A practical approach to performance improvement," Renewable Energy, vol. 133, pp. 1078-1085, 2019.

[16] E. M. Sparrow, S. V. Patankar and S. Ramadhyani, "Analysis of Melting in the Presence of Natural Convection in the Melt Region," ASME Journal of Heat Transfer, vol. 99, pp. 520-526, 1977.

[17] A. D. Brent, V. R. Voller and K. J. Reid, "Enthalpy-Porosity Technique for Modeling Convection-Diffusion Phase Change: Application to the Melting of a Pure Metal," Numerical Heat Transfer, vol. 13, pp. 297-318, 1988.

[18] C. Gau and R. Viskanta, "Melting and Solidification of a Metal System in a Rectangular Cavity," International Journal of Heat and Mass Transfer, vol. 27, pp. 113-123, 1984.

[19] Y.Wang, A.Amiri and K.Vafai, "An experimental investigation of the melting process in a rectangular enclosure," International Journal of Heat and Mass Transfer, vol. 42, pp. 3659-3672, 1999.

[20] C. P. Desai and K. Vafai, "A Unified Examination of the Melting Process Within a Two-Dimensional Rectangular Cavity," ASME Journal of Heat Transfer, vol. 115, pp. 1072-1075, 1993.

[21] V. Voller and C. Prakash, "A fixed grid numerical modelling methodology for convection-diffusion mushy region phase-change problems," Int. J. Heat Mass Transf., vol. 30, p. 1709e1719, 1987.

[22] J. K. L. Fan, "Thermal conductivity enhancement of phase change materials for thermal energy storage: a review," Renew. Sustain. Energy Rev., vol. 14, pp. 24-46, 2011.

[23] M. Liu, W. Saman and F. Bruno, "Review on storage materials and thermal performance enhancement techniques for high temperature phase change thermal storage systems," Renew. Sustain. Energy Rev., vol. 16, pp. 2118-2132, 2012.

[24] C. Zhao, "Review on thermal transport in high porosity cellular metal foams with open cells," Int. J. Heat Mass Transfer, vol. 55 , pp. 3618-3632, 2012.

[25] B. Zalba, J. Marín, L. Cabeza and H. Mehling, "Review on thermal energy storage with phase change: materials, heat transfer analysis and applications," Applied Thermal Engineering , vol. 23, pp. 251-283, 2003.

[26] A. Ghahremannezhad and K. Vafai, "Thermal and hydraulic performance enhancement of microchannel heat sinks utilizing porous substrates," International Journal of Heat and Mass Transfer, vol. 122, pp. 1313-1326, 2018.

[27] A. Ghahremannezhad, H. Xu, M. A. Nazari, M. H. Ahmadi and K. Vafai, "Effect of porous substrates on thermohydraulic performance enhancement of double layer microchannel heat sinks," International Journal of Heat and Mass Transfer, vol. 131, pp. 52-63, 2019.

[28] X. Tong, J. Khan and M. RuhulAmin, "Enhancement of heat transfer by inserting a metal matrix into a phase change material," Numer. Heat Transf. Appl., vol. 30, pp. 125-141, 1996.

[29] X. Py, "Paraffin/porous–graphite-matrix composite as a high and constant power thermal storage material," Int. J. Heat Mass Transfer, vol. 44, pp. 2727-2737, 2001.

[30] K. Lafdi, O. Mesalhy and S. Shaikh, "Experimental study on the influence of foam porosity and pore size on the melting of phase change materials," J. Appl. Phys., vol. 102, 2007.

[31] A. Karaipekli, A. Sari and K. Kaygusuz, "Thermal conductivity improvement of stearic acid using expanded graphite and carbon fiber for energy storage applications," Renew. Energy, vol. 32, pp. 2201-2210, 2007.

[32] C. Jiao, B. Ji and D. Fang, "Preparation and properties of lauric acid–stearic acid/expanded perlite composite as phase change materials for thermal energy storage," Mater. Lett., vol. 67, pp. 352-354, 2012.

[33] C. Zhao, W. Lu and Y. Tian, "Heat transfer enhancement for thermal energy storage using metal foams embedded within phase change materials (PCMs)," Sol. Energy, vol. 84, pp. 1402-1412, 2010.

[34] Y. Tian and C. Zhao, "A numerical investigation of heat transfer in phase change materials (PCMs) embedded in porous metals," Energy, vol. 36, no. 9, pp. 5539-5546, 2011.

[35] T. Oya, T. Nomura, N. Okinaka and T. Akiyama, "Phase change composite based on porous nickel and erythritol," Appl. Therm. Eng., vol. 40, pp. 373-377, 2012.

[36] W. Li, Z. Qu, Y. He and W. Tao, "Experimental and numerical studies on melting phase change heat transfer in open-cell metallic foams filled with paraffin," Applied Thermal Engineering, vol. 37, pp. 1-9, 2012.

[37] Z. Liu, Y. Yao and H. Wu, "Numerical modeling for solid–liquid phase change phenomena in porous media: Shell-and-tube type latent heat thermal energy storage," Applied Energy, vol. 112, pp. 1222-1232, 2013.

[38] X. Xiao, P. Zhang and M. Lib, "Preparation and thermal characterization of paraffin/metal foam composite phase change material," Applied Energy, vol. 112, pp. 1357-1366, 2013.

[39] X. Xiao, P. Zhang and M. Li, "Effective thermal conductivity of open-cell metal foams impregnated with pure paraffin for latent heat storage," Int. J. Therm. Sci., vol. 81, pp. 94-105, 2014.

[40] Y. Xu, Q. Ren, Z.-J. Zheng and Y.-L. He, "Evaluation and optimization of melting performance for a latent heat thermal energy storage unit partially filled with porous media," Applied Energy, vol. 193, pp. 84-65, 2017.

[41] J. M.Mahdi and E. C. Nsofor, "Melting enhancement in triplex-tube latent heat energy storage system using nanoparticles-metal foam combination," Applied Energy, vol. 191, pp. 22-34, 2017.

[42] H. Zheng, C. Wang, Q. Liu, Z. Tian and X. Fan, "Thermal performance of copper foam/paraffin composite phase change material," Energy Conversion and Management, vol. 157, p. 372–381, 2018.

[43] Z. Chen, D. Gao and J. Shia, "Experimental and numerical study on melting of phase change materials in metal foams at pore scale," Int. J. Heat Mass Transf., vol. 72, pp. 646-655, 2014.

[44] S. S. Sundarram and W. Li, "The effect of pore size and porosity on thermal management performance of phase change material infiltrated microcellular metal foams," Applied Thermal Engineering, vol. 64, pp. 147-154, 2014.

[45] S. Feng, M. Shi, Y. Li and T. J. Lu, "Pore-scale and volume-averaged numerical simulations of melting phase change heat transfer in finned metal foam," International Journal of Heat and Mass Transfer, vol. 90, pp. 838-847, 2015.

[46] J. Yang, L. Yang, C. Xu and X. Du, "Numerical analysis on thermal behavior of solid-liquid phase change within copper foam with varying porosity," Int. J. Heat Mass Transf., vol. 84, pp. 1008-1018, 2015.

[47] Y. Tao, Y. You and Y. He, "Lattice Boltzmann simulation on phase change heat transfer in metal foams/paraffin composite phase change material," Appl. Therm. Eng., vol. 93, pp. 476-485, 2016.

[48] X. Yang, W. Wang, C. Yang, L. Jin and T. J. Lu, "Solidification of fluid saturated in open-cell metallic foams with graded morphologies," International Journal of Heat and Mass Transfer, vol. 98, pp. 60-69, 2016.

[49] F. Zhu, C. Zhang and X. Gong, "Numerical analysis on the energy storage efficiency of phase change material embedded in finned metal foam with graded porosity," Appl. Therm. Eng., vol. 123, pp. 256-265, 2017.

[50] Z. Zhang and X. He, "Three-dimensional numerical study on solid-liquid phase change within open-celled aluminum foam with porosity gradient," Applied Thermal Engineering, vol. 113, pp. 298-308, 2017.

[51] A. Kumar and S. K. Saha, "Latent heat thermal storage with variable porosity metal matrix: A numerical study," Renewable Energy, vol. 125, pp. 962-973, 2018.

[52] K. Vafai, "Convective Flow and Heat Transfer in Variable Porosity Media," Journal of Fluid Mechanics, vol. 25, pp. 233-259, 1984.

[53] K. Vafai and R. Thiyagaraja, "Analysis of Flow and Heat Transfer at the Interface Region of a Porous Medium," International Journal of Heat and Mass Transfer, vol. 30, pp. 1391-1405, 1987.

[54] K. Vafai and C. Tien, "Boundary and inertia effects on flow and heat transfer in porous media," Int. J. Heat Mass Transfer, vol. 24, p. 195–203, 1981.

[55] V. Shatikian, G. Ziskind and R. Letan, "Numerical investigation of a PCM-based heat sink with internal fins," Int. J. Heat Mass Transf., vol. 48, pp. 3689-3706, 2005.

[56] V. Calmidi and R. Mahajan, "Forced convection in high porosity metal foams," ASME Journal of Heat Transfer, vol. 122, p. 557–565, 2000.

[57] O. Mesalhy, K. Lafdi, A. Elgafy and K. Bowman, "Numerical study for enhancing the thermal conductivity of phase change material (PCM) storage using high thermal conductivity porous matrix," Energy Conversion and Management, vol. 46, pp. 847-867, 2005.

[58] V. Calmidi, "Transport Phenomena in High Porosity Fibrous Metal Foams," University of Colorado, 1198.

[59] S. Churchill and H. Chu, "Correlating equations for laminar and turbulent free convection from a horizontal cylinder," Int. J. Heat Mass Transfer, vol. 18, pp. 1049-1053, 1975.

[60] R. Baby and C. Balaji, "Experimental investigations on thermal performance enhancement and effect of orientation on porous matrix filled PCM based heat sink," Int. Commun. Heat Mass Transf., vol. 46, pp. 27-30, 2013.

[61] K. Nayak, S. Saha, K. Srinivasan and P. Dutta, "A numerical model for heat sinks with phase change materials and thermal conductivity enhancers," Int. J. Heat Mass Transf., vol. 49, pp. 1833-1844, 2006.